Master's thesis

NTNU
Norwegian University of Science and Technology
Faculty of Natural Sciences
Department of Physics

Ingvild Hansen

Correlated Structural and Optical Characterisation of Individual AlGaN Nanowires on Graphene

Master's thesis in Nanotechnology

June 2019

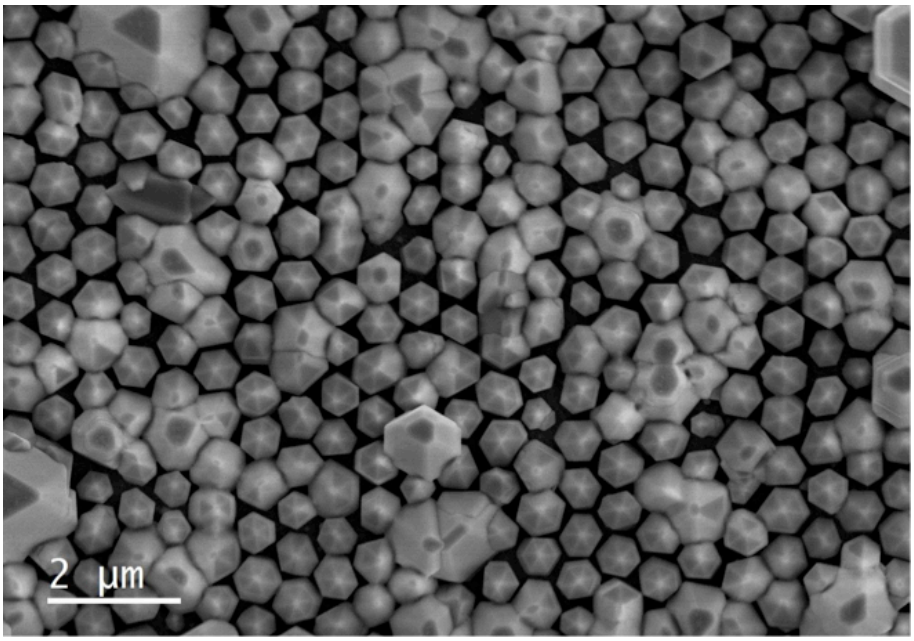

Secondary electron SEM image of position-controlled AlGaN nanowires on graphene.

NTNU
Norwegian University of Science and Technology

CrayoNano

Ingvild Hansen

Correlated Structural and Optical Characterisation of Individual AlGaN Nanowires on Graphene

Master's thesis in Nanotechnology
Supervisor: Antonius T. J. van Helvoort, Ida Marie Høiaas
June 2019

Norwegian University of Science and Technology
Faculty of Natural Sciences
Department of Physics

NTNU
Norwegian University of
Science and Technology

Abstract

III-nitrides exhibit promising properties for application within ultraviolet optoelectronic devices. However, a significant roadblock for future development is the poor wall-plug efficiency for short wavelength devices. With a growing demand for these devices, knowledge concerning the features causing the efficiency droop is sought for. Some of the contributions include lattice mismatch between the substrate and the III-nitride thin film, and absorption in the ultraviolet range by the substrate. A significant enhancement of the crystal quality has been achieved by substituting conventional planar devices with nanowire-based ones. Graphene has proved to exhibit favourable properties as growth substrate and transparent electrode with low absorption in the ultraviolet range. Here, a correlated study comprising scanning electron microscopy, cathodoluminescence and (scanning) transmission electron microscopy, including energy-dispersive X-ray spectroscopy, has been applied to metal-organic chemical vapour deposition grown AlGaN nanowires on graphene. The aim is to link optical properties to structural and compositional properties in order to optimise growth of more efficient AlGaN nanowire-based ultraviolet light-emitting diodes.

Position-controlled nanowire growth on a patterned mask allows for greater uniformity within devices to help fabrication and device performance, however, structural variation still exists. Hence, a correlated study is necessary in order to recognise the factors limiting device efficiency. Six individual and representative nanowires are therefore systematically studied and presented, where the five aforementioned techniques are applied to every nanowire. A cluster consisting of several nanowires attached to the mask is also included in the correlated study.

The AlGaN nanowires mainly grow separately with a diameter and length of 499 ± 113 nm and 574 ± 115 nm, respectively. From transmission electron microscopy inspection the crystal structure is found to be wurtzite with growth direction along the c-axis. The displayed facets are $\{10\bar{1}0\}$, $\{1\bar{1}02\}$ and $\{0001\}$. For the majority of the nanowires peak emission is detected at 361 nm and the emission band is found to exhibit a redshift and a decrease in intensity towards the bottom of the nanowires. Grain boundaries and other irregularities are assumed to be responsible for the latter. The redshift can possibly be explained by Mg acceptor levels from the p-GaN layer which, due to variation in growth rate, is much thicker on the nanowire m-planes. For the optical data, novel processing techniques based on unsupervised machine learning are applied in order to remove noise and redundant data and to detect repeating patterns. Diffusion of charge carriers deteriorates the spatial resolution of the optical data, complicating the process of assigning certain emission patterns to certain regions of the nanowires.

The studied AlGaN nanowires are predominantly grown defect-free. However, stacking faults, facet changes and other irregularities occasionally occur. The distribution of these defects is found to increase in density for the bottom part of the nanowires. Variation in the thickness of the heterostructure layers for different facets also causes undesirable effects. Higher crystal quality and more uniform thickness for the radial growth should therefore be targeted via systematic growth optimisation. For this routine, correlated optical and structural characterisation on the nm-scale, as developed and applied in the present study, will be essential.

Sammendrag

III-nitrider viser lovende egenskaper for bruk innen ultrafiolette optoelektroniske enheter, men en betydelig utfordring for fremtidig utbedring er lav effektivitet for enheter med kort bølgelengde. Med en økende etterspørsel for slike enheter søkes kunnskap om årsakene til den lave effektiviteten. Noen av bidragene inkluderer uoverensstemmelse i gitterkonstant mellom substrat og III-nitrid tynnfilm, og absorpsjon av ultrafiolett stråling i substratet. En betydelig forbedring av krystall-kvaliteten oppnås ved å substituere konvensjonelle planare enheter med enheter basert på nanotråder. Grafén har også vist seg å ha gunstige egenskaper som vekstsubstrat og ikke-absorberende elektrode. I dette arbeidet presenteres en korrelert studie bestående av sveipelektronmikroskopi, katodeluminisens og (sveipe)transmisjonselektronmikroskopi, inkludert energidispersiv spektroskopi, av AlGaN-nanotråder på grafén, grodd med metallorganisk gass-fase-epitaksi. Målet med dette er å etablere en sammenheng mellom strukturelle og optiske egenskaper for å øke effektiviteten til AlGaN nanotråd-baserte ultrafiolett lysemitterende dioder.

Nanotråder grodd med posisjon-kontroll ved hjelp av en mønstret maske tillater mer uniforme nanotråder for enklere fabrikasjon og økt ytelse. Til tross for utnyttelse av denne vekstmetoden eksisterer det fortsatt variasjoner i nanotrådene. På grunn av dette er det nødvendig å utføre en korrelert studie slik at effektivitetsbegrensende faktorer kan identifiseres. Seks individuelle og representative nanotråder er derfor systematisk inspisert og presentert med de fem nevnte teknikkene. En klynge bestående av flere nanotråder festet til den mønstrede masken er også inkludert i den korrelerte studien.

De inspiserte AlGaN-nanotrådene gror hovedsakelig separat med en diameter og lengde på henholdsvis 499 ± 113 nm og 574 ± 115 nm. Inspeksjon med transmisjonselektronmikroskop viser wurtzitt krystallstruktur med vekstretning langs c-aksen. De eksponerte fasettene er $\{10\bar{1}0\}$, $\{1\bar{1}02\}$ og $\{0001\}$. Flertallet av nanotrådene viser emisjon rundt 361 nm og dette emisjonsbåndet har en rødforskyvning og en gradvis avtagende intensitet mot bunnen av nanotrådene. Korngrenser og andre uregelmessigheter er antatt å være ansvarlig for sistnevnte. Rødforskyvningen kan muligens forklares med ytterligere akseptor-energinivåer fra p-GaN laget, som er tykkere på de nedre m-planene som følge av høyere vekstrate. Optisk data er analysert med avanserte prosesseringsteknikker basert på ikke-veiledet maskinlæring. Hensikten er å fjerne overflødig data og støy og å gjenkjenne repeterende mønster i dataen. Diffusjon degraderer den romlige oppløsningen i den optiske dataen, noe som kompliserer mønstergjenkjenning og lokalisering av mønster på nanotrådene.

AlGaN nanotrådene er grodd tilnærmet uten defekter, men noen stablefeil, fasettendringer og andre uregelmessigheter foreligger sporadisk. Fordelingen av disse øker i tetthet for den nedre delen av nanotrådene. Variasjon i tykkelse for forskjellige lag forårsaker også uønskede effekter. Målrettet vekst med høyere krystallkvalitet og mer uniform tykkelse for den radielle veksten bør derfor implementeres for optimalisering av enhetene. Til dette formålet vil korrelert optisk og strukturell karakterisering på nm-skala, som utviklet og utført i denne studien, være viktig.

Preface and acknowledgements

This thesis is the final work of my master's degree in the Master of Science program in Nanotechnology, with specialisation in Nanoelectronics. The work is a continuation of the authors project work carried out autumn 2018 at the Department of Physics, Norwegian University of Science and Technology (NTNU). The experimental work is done at the TEM Gemini Centre and at CrayoNano's facilities at Sluppen, Trondheim. All data recorded in this report is acquired by me, unless otherwise stated explicitly.

First of all I would like to thank my supervisor Antonius T. J. van Helvoort for excellent guidance and invaluable feedback on my work, during the course of this year. I would also like to thank Ida Marie Høiaas for valuable assistance and fruitful discussions. It has been highly educational and inspiring to work with you.

The nanowires studied in this work were grown by Mazid Munshi, Dheeraj Dasa and Julie Hessevik from CrayoNano. Thank you so much for the help with CL acquisition and interpretation. I would also like to thank the entire CrayoNano team and the TEM group at NTNU for constructive feedback and for the opportunity to write this master's thesis.

Last but not least, I want to thank my family and friends for the love and support during the last five years here in Trondheim.

Ingvild Hansen
Trondheim, June 2019

List of abbreviations

ADF	Annular dark-field
AEM	Analytical electron microscopy
BF	Bright-field
BSE	Back-scattered electron
BSF	Basal-plane stacking fault
CBED	Convergent-beam electron diffraction
CL	Cathodoluminescence
DF	Dark-field
DP	Diffraction pattern
EBIC	Electron beam-induced current
EBL	Electron-beam lithography
EDS	Energy-dispersive X-ray spectroscopy
EL	Electroluminescence
EELS	Electron energy loss spectroscopy
FCC	Face-centred cubic
FFT	Fast Fourier transform
FWHM	Full width at half maximum
HCP	Hexagonal close-packed
HRTEM	High-resolution transmission electron microscopy
LED	Light-emitting diode
MBE	Molecular beam epitaxy
MOCVD	Metal-organic chemical vapour deposition
NMF	Non-negative matrix factorisation
NW	Nanowire
PCA	Principal component analysis
PL	Photoluminescence
QCSE	Quantum-confined Stark effect
SAED	Selected-area electron diffraction
SAG	Selected-area growth
SE	Secondary electron
SEM	Scanning electron microscopy
SLG	Single-layer graphene
S/N	Signal-to-noise ratio
STEM	Scanning transmission electron microscopy
TEM	Transmission electron microscopy
UV	Ultraviolet
VDWE	Van der Waals epitaxy
WZ	Wurtzite
XRD	X-ray diffraction
YL	Yellow luminescence
ZB	Zinc blende

Contents

1 Introduction

Since the 19th century lightning devices have made a transition from the first incandescent light bulb to the efficient and more complex semiconductor-based light-emitting diode (LED) [1]. However, in the deep-ultraviolet (DUV) range of the electromagnetic spectrum a satisfactory efficiency has not yet been achieved for LEDs. Semiconductor light sources transmitting in the DUV range have become an important field of research in the recent years, as they are essential in a wide range of application areas. The current market consists of applications within disinfection, air- and water purification, environmental monitoring, food processing, photochemical reactions, counterfeit detection and forensics, to mention a few [2].

In the past decade the III-nitride material system has been extensively studied within the field of optoelectronic devices, much due to the wide direct bandgap and the ability to tune the bandgap energy. This resulted in the invention of efficient blue LEDs, for which the inventors were awarded the Nobel Prize in Physics in 2014 [3]. However, misfit-induced dislocations in III-nitride thin films caused by lattice mismatch to the substrate constitute a bottleneck for the efficiency, with a wall plug efficiency of less than 5% for today's UV LEDs. Hence, a great potential for improving performance exists. Another factor limiting the device efficiency is light absorption in the UV range by the substrate. AlN with high crystal quality is often used but comprises significant additional costs [2, 4].

By growing III-nitrides in the shape of one-dimensional nanowires (NWs), which structure has proved to greatly improve the III-nitride crystal quality (i.e. provide low defect density), the efficiency bottleneck of III-nitride LEDs can be surpassed. Due to their small diameter NWs are able to relax strain in the lateral direction and hence avoid introduction of threading dislocations [5]. In the search for a UV transparent substrate a two-dimensional semimetal named graphene, extracted from graphite by A. Geim and K. Novoselov in 2004, has proved to be an attractive alternative. The extraction of stable graphene was awarded the Nobel Prize in Physics 2010 [6]. This sparked off enormous research and development activities, for example, the EU Flagship Graphene [7] and graphene-related activities at large enterprises like Samsung and IBM [8]. Growth of III-V NWs on graphene has been demonstrated and has attracted a lot of attention [9]. For the purpose of a UV LED, graphene can function as both the growth substrate and one of the LED electrodes, due to its broad functionality.

CrayoNano is a start-up company developing disruptive technology to the UV LED market with the goal of providing more efficient and durable, low cost UV LEDs. Realisation of such devices would end the era of hazardous traditional

mercury UV lamps. CrayoNano sprung out of the Norwegian University of Science and Technology and was established in 2012 [10]. The company has seen a continuous growth since then and recently installed their own production line for UV LED devices. Their devices are based on metal-organic chemical vapour deposition (MOCVD) grown AlGaN NWs on inexpensive sapphire substrates covered with single layer graphene (SLG). In order to achieve more uniform devices, position-controlled NW growth on graphene with an electron beam lithography (EBL) patterned mask is being developed. The company is aiming for commercialisation of their technology within 2023 [11].

The goal of the study presented in this thesis is the following:

(1) Correlate the optical properties to the structure and composition of position-controlled AlGaN NWs developed by CrayoNano.

(2) Analyse defects and variations in the growth of radial heterostructures at nm-scale to better understand and possibly improve the growth process.

A correlated study is necessary to determine which structural features are responsible for the different optical characteristics, and to detect NW-to-NW variation. A schematic of the targeted structure of a single NW and several NWs implemented as part of a device is shown in Figure 1.1 (a) and (b), respectively. The methods applied in this correlated study include conventional transmission electron microscopy (TEM), scanning electron microscopy (SEM), high-angle annular dark-field scanning transmission electron microscopy (HAADF STEM), energy-dispersive X-ray spectroscopy (EDS) and cathodoluminescence (CL).

This thesis is structured in the following way. First theory on NW-based optoelectronic devices, crystallography, diffraction and the applied techniques are given in chapter 2. Following is the experimental details and the results in chapter 3 and 4. Finally, the results are discussed in chapter 5 before a conclusion and suggestions for future work are presented in chapter 6 and 7.

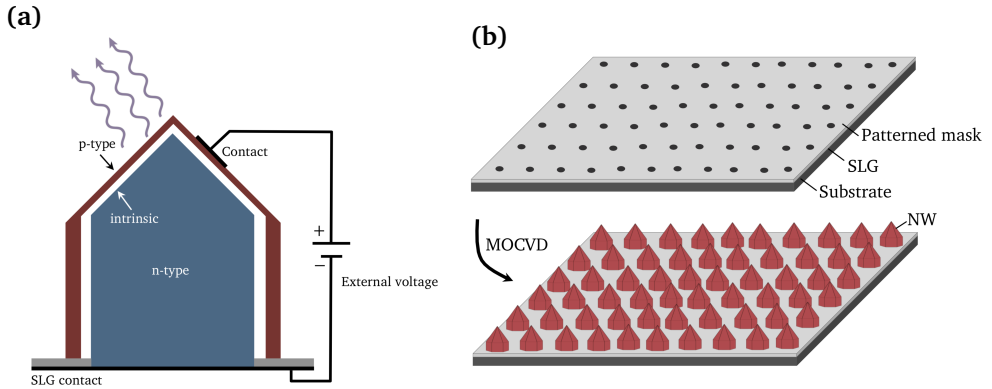

Figure 1.1: (a) Simplified schematic showing the structure of a single NW in a NW-based pin LED device. In this work the device is made from different alloys of $Al_xGa_{1-x}N$. (b) NW growth with position control where a patterned mask is exploited resulting in uniform and separated NWs. MOCVD is the growth method and EBL is applied to pattern the mask.

2 Theory

This chapter provides the theory required to interpret experimental methods and results presented in chapter 3 and 4. Firstly, NW-based optoelectronic devices, relevant materials and growth methods are described. Then necessary theory on crystallography is presented before finally, the applied microscopy techniques in this work are introduced[1].

2.1 NW-based optoelectronic devices

NWs exhibit desirable properties due to their one-dimensional structure which are especially sought for in novel optoelectronic devices today. These properties include high crystal quality and appealing optical and electronic behaviour [13]. It is therefore believed that the performance of many optoelectronic devices can be enhanced by substituting conventional two-dimensional and bulk materials with NW-based ones. There is for example a big demand for increasing the quantum efficiency of certain LEDs and a device architecture based on NWs is promising [13]. Today, proof-of-concept devices based on NWs have been demonstrated for solar cells, detectors, LEDs and lasers to mention a few [14].

Both radial and axial growth of NW heterostructures can be realised, depending on the growth parameters, for a variety of material systems. This is illustrated in Figure 2.1. Because of the small diameter of NWs they are able to relax strain radially. By doing so NWs avoid threading dislocations along the growth direction and they become well suited for heterostructural growth. Threading dislocations constitute a critical issue for planar devices, as illustrated in Figure 2.2 [15]. This is because in a LED, for example, these defects can contribute to non-radiative recombination and carrier trap sites, which is undesirable. At atomically sharp interfaces, for example, in multiple quantum wells (MQWs) or between the substrate and the device, strain introduction is caused by lattice-mismatch in two-dimensional and bulk structures. This is a less strict condition for NWs, as the contact area and also the volume is less. For two-dimensional and bulk structures, threading dislocations can severely hamper the device performance [16, 13]. In order to reduce lattice-mismatch at the substrate-device interface, growth by van der Waals epitaxy (VDWE) can be performed. The latter will be discussed in detail in section 2.1.2 [16].

[1] The theory section is to a large extent based on a previous thesis written by the author [12].

Figure 2.1: Illustration of hexagonal NW with (a) an axial heterostructure, where different layers are grown in the c-direction and (b) a radial heterostructure, where layers are grown perpendicular to the c-axis. It is also possible to grow structures composed of a mixture of the two.

Another property of NWs is their large surface-to-volume ratio, due to size effects. This is preferable for light extraction or light trapping in devices. By applying one-dimensional NWs in optoelectronics devices the light-extraction efficiency in a LED or the light-trapping efficiency in a detector can be enhanced, as the effective area emitting or detecting light is made larger. However, with a large surface-to-volume ratio NWs are also more disposed to surface defect states, which might affect the optoelectronic properties in an undesirable manner [15]. This is because the electronic structure of a surface deviates from the bulk. Due to the abrupt transition from material to vacuum at the surface, the electronic band structure is altered and surface-bound states with energies within the forbidden gap can be found [17].

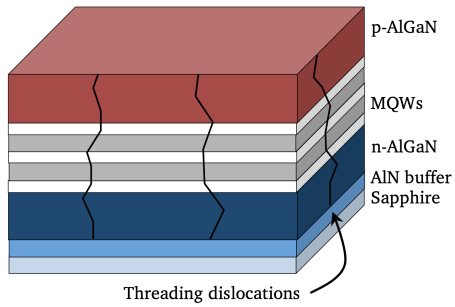

Figure 2.2: Illustration of threading dislocations in a planar LED. Threading dislocation and similar irregularities can, for example, act as carrier trap sites or cause non-radiative recombination [16].

As a consequence of the one-dimensional structure of NWs, charge carriers are confined in two directions and free to move in one. Hence, the charge carriers

have one degree of freedom and can be approximated by the Schrödinger equation in one dimension, discussed in section 2.1.5 [18]. Quantum confinement effects occur when the size of an object is comparable to the wavelength of the electrons inside, as the electrons no longer can behave as free particles. This alters the optical and electronic properties of the object, as the possible energies the object can take get discretised and hence make the bandgap dependent on the size [19]. Therefore, the bandgap can be controlled by altering the object size at nm-scale.

In this work, a III-nitride NW-based UV LED device is studied and a simplified schematic was illustrated in Figure 1.1. The NWs have a radial heterostructure including a pin-junction and are grown with position control on a patterned SiO_2 mask. In the finalised device, each of the doped regions of the NWs are connected to two separate contacts. These are connected with an external voltage supply which, when turned on, put the pin-junction in forward bias. Depending on the material composition of the pin-junction, electromagnetic radiation of a certain wavelength results. A more detailed description of the NWs and device design will be given in the experimental section.

2.1.1 III-nitrides

The III-nitride material system, including AlN, GaN, InN and their ternary and quaternary compounds, is widely used for UV LED applications. The system exhibits a wide bandgap, which is required for UV radiation, and it can withstand high operating temperatures. For the $Al_xGa_{1-x}N$ system relevant for this work the bandgap is also direct, which is important for recombination efficiency. $Al_xGa_{1-x}N$ exhibits hexagonal crystal structure, more specifically the Wurtzite (WZ) crystal structure, which will be discussed in detail in section 2.2.2 [20].

By altering the ratio between the different III-components in ternary III-nitrides, the bandgap can be tuned. $Al_xGa_{1-x}N$ can be tuned from 3.4 eV (GaN, $x = 0$) to 6.2 eV (AlN, $x = 1$), as seen in Figure 2.3 [21]. For $Al_xGa_{1-x}N$ the lattice constant changes with the III-element composition, however, only slightly. Hence, minimal defects are introduced by AlN/GaN heterojunctions.

The bandgap for $Al_xGa_{1-x}N$ is predicted to follow the succeeding relation [21]

$$E_g^{Al_xGa_{1-x}N}(x) = E_g^{AlN}x + E_g^{GaN}(1-x) - bx(1-x), \tag{2.1}$$

where the bandgap bowing parameter is given by b. This parameter describes the deviation from the linear approximation between AlN and GaN in Figure 2.3. Hence, by controlling the composition a specific range in the electromagnetic spectrum can be obtained.

2.1.2 Graphene

Graphene is a two-dimensional membrane comprised of carbon atoms arranged in a close-packed hexagonal pattern, as shown in Figure 2.4(a). This carbon allotrope has a thickness of a single atom with an interatomic spacing of 1.42 Å [22], as illustrated in Figure 2.4(b). Graphene is categorised as a semi-metal, hence

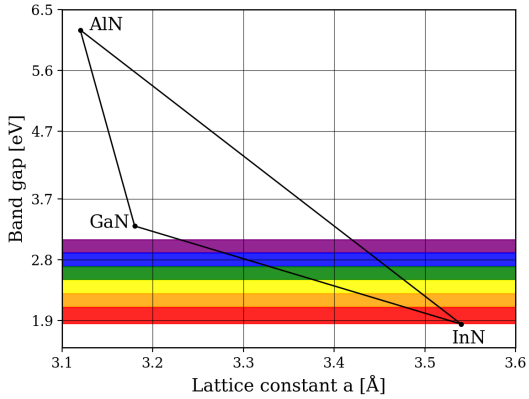

Figure 2.3: Bandgap and lattice constant for III-nitrides of varying composition. For $Al_xGa_{1-x}N$, the bandgap increases with Al/Ga ratio, while the lattice constant decreases slightly. Adapted from [4, 20].

a slight overlap between the conduction band and the valence band is present, making it an excellent conductor of electricity. Graphene conducts heat well, it shows exceptional mechanical properties and it is close to transparent, also in the UV-range [23]. These properties make graphene a good option for electrode material in LEDs. A difficulty regarding the atomic structure of graphene is the sp^2 hybridised bonding and the absence of dangling bonds [9, 24], making it hard to induce crystal growth on its surface by epitaxy. Hence, in order to grow a crystal structure on graphene a nucleation layer, also called a buffer, is often required [22]. By applying VDWE it is possible to minimise strain induced due to lattice-mismatch between the substrate and the NW, which is discussed in more detail under.

Graphene can be fabricated from many different processes, like mechanical cleavage, epitaxial growth, chemical vapour deposition (CVD), total organic synthesis and chemical methods [25]. CVD is a frequently used, cost-effective method producing high-quality films with high throughput that can be transferred to the desired substrate [26]. Graphene can, for example, be grown on Cu-foil and transferred to sapphire by etching the Cu away. Sapphire provides a low-cost and UV transparent option suitable for UV LEDs. A common irregularity induced in graphene during growth and substrate transfer is wrinkles, as a result of interaction between the substrate and graphene [27]. In addition to the graphene structure discussed above it is also possible to grow two or more layers of graphene on top of each other, resulting in bilayer and multilayer graphene [23].

Van der Waals epitaxy

VDWE occurs when the substrate that is attempted growth upon has no dangling bonds. An example of this is graphene, which has naturally occurring surface-

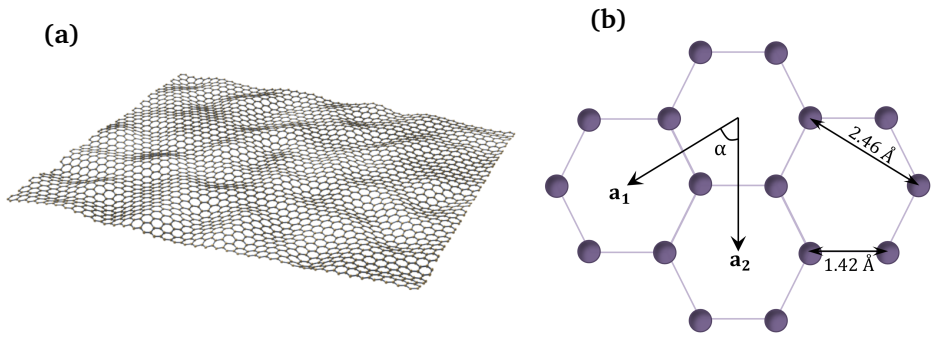

Figure 2.4: (a) A single layer of graphene [28] and (b) the corresponding unit cell with primitive lattice vectors $\boldsymbol{a_1}$ and $\boldsymbol{a_2}$ related by $\alpha = 60°$ and given lattice constants. Adapted from [24, 22].

terminated bonds, or bulk material with a passivated surface. During growth no covalent bonds occur between the substrate and the epitaxial layer. Only van der Waals interaction arises, which is a weaker interaction. Therefore, even though lattice-mismatch is present between the substrate and the epitaxial growth, the epitaxial layer grows without strain. VDWE can be performed in, for example, a MOCVD growth system [16].

2.1.3 Position-controlled growth

In order to obtain reproductive growth and avoid coalescence for device fabrication and performance, the position of every single NW can be controlled. One method to do this is by applying a mask to the substrate before growing the NWs. The mask is patterned with holes of desired diameter and spacing, such that NW growth is restricted to the holes only. Separate NWs grown from separate holes create arrays of NWs with more uniform properties compared to NW grown without position control. In order to obtain sub-micron sized holes in the mask, electron-beam lithography (EBL) can be applied.

EBL systems are based on the SEM and use the same principles as conventional photolithography. Conventional photolithography can not be applied for sub-micron precision due to the Rayleigh criterion, which limits the resolving ability of an image-forming device to approximately half the wavelength of the applied light (see Equation 2.54). In an EBL system the light source is replaced by an electron beam, which is scanned over an electron-sensitive film (referred to as resist) covering the substrate to be patterned. Exposure to the electron beam alters the solubility of the resist, such that selective removal results in a solid pattern left on the substrate with a resolution of about 5 nm limited by the resist. Compared with conventional photolithography EBL provides superior resolution for pattern features, due to the use of electrons instead of electromagnetic radiation and the maskless writing method. On the other hand, EBL writing and processing is a slow and high-cost production method unable to pattern larger areas with high

efficiency. Hence, it is not suitable for large-scale wafer production [29, 30]. A schematic of the EBL patterning process of resist on a substrate is illustrated in Figure 2.5.

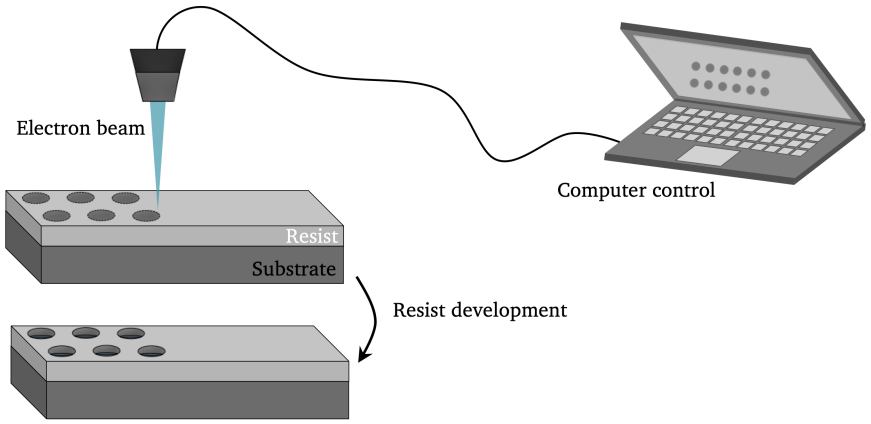

Figure 2.5: Simplified illustration of EBL where the vacuum column, lenses etc. have been omitted. A substrate covered with a resist is exposed to an electron beam that is scanned according to a pattern. Selective removal of the resist occurs during resist development as the electron beam alters the solubility of the exposed areas.

2.1.4 III-nitride growth by MOCVD

Due to precise control of growth parameters, resulting in good uniformity in rate of growth, MOCVD growth systems are today considered state-of-the-art in line with molecular beam epitaxy (MBE) [31]. These properties allow for sharp interfaces in single crystal heterostructure growth. Growth by MOCVD is especially popular for III-V semiconductor optoelectronic devices, due to lower production price, good process repeatability for mass production and faster growth compared to MBE [31].

The MOCVD system is made up of a gas blending system, a reactor and a gas exhaust system, illustrated in Figure 2.6. The blending system controls and combines the carrier gas, the III precursor and the V reactant. During MOCVD processing the growth substrate is heated to the process temperature and rotated for uniform deposition [32]. The reactants are evaporated prior to being transported into the reactor with the aid of carrier gases and subsequently decompose and react onto the substrate. Decomposed III and V reactants eventually reach the surface and diffuse laterally until they find an appropriate crystal site and settle. Depending on pressure, temperature and gas flows, layered structures of varying composition can be processed in the shape of thin films or more complex geometries, like NWs [33]. NWs can be grown with catalyst seeds, for example Au, or catalyst-free, which is the case for the growth mechanism studied in this work [4].

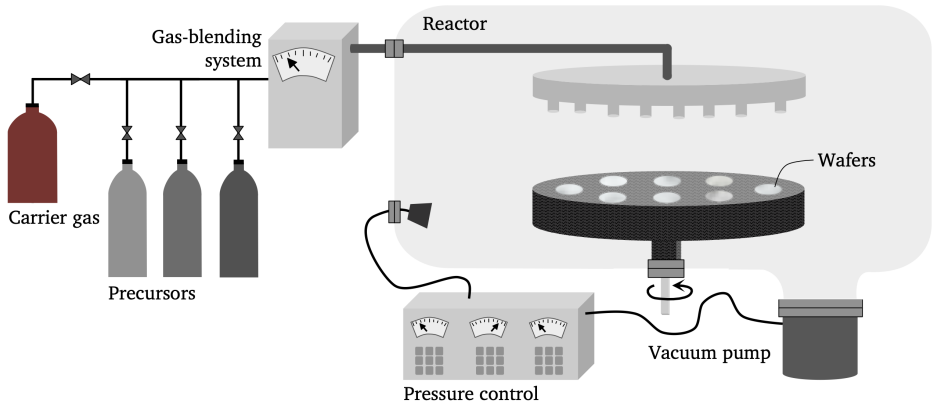

Figure 2.6: Simplified schematic of a MOCVD growth system. Chemical reaction of the gas precursors takes place on the substrate surface at moderate pressure. The substrate is placed on a susceptor with the temperature controlled based on the chemical reaction taking place at the wafer surface. Adapted from [33].

For the NW structure in this work an intermediate layer between the NWs and the SLG layer is required in order to wet the graphene surface. For GaN growth on graphene AlN is the preferred buffer [34]. This method of position-controlled growth on graphene with a SiO_2 mask is not as well-developed as the conventional Si/SiO_2 interface. Hence, systematic growth optimisation is necessary in order to achieve targeted properties. The thickness and the crystallographic orientation of this AlN layer, in addition to the morphology of its surface, is known to affect the NW growth [35]. During the initial growth process small nucleation islands are randomly distributed over the graphene-covered sapphire substrate through the holes in the mask. Some islands are distributed on top of the mask as well. These nucleation islands comprise low energy nucleation sites for the following NW growth [31] and increase in size until they reach a critical radius. Eventually the nucleation islands start growing vertically along the c-axis, due to the fact that incorporation of adatoms on the c-plane is preferred over incorporation of adatoms on the m-plane [36, 37]. By introducing the different gas phase reactants into the chamber with varying concentration ratio and processing conditions, a heterostructure of $Al_xGa_{1-x}N$ with $0 \leq x \leq 1$ and possibly doping is grown from the nucleation islands.

The sticking coefficient in surface physics is a measure of the adsorption of an element to a surface, taking a value between 0 and 1 [38]. For Al the sticking coefficient is larger than for Ga, which makes the surface mobility of Ga larger than for Al [39]. One explanation for this is that the Al-N bond is stronger than the Ga-N bond. The difference in surface mobility can possibly affect crystal quality, surface morphology and also the growth rate [39].

2.1.5 Principles of the LED

The light-emitting diode is an optoelectronic device turning electrical power into light by electron-hole recombination [40]. The simplest design of a LED consists

of a single diode; a two-terminal component conducting current primarily in one direction. More complex LED configurations are, for example, pin-diodes and diodes with quantum wells [41]. A simple diode is made up of a semiconductor with two adjacent regions of different doping (p- and n-doping) called a pn-junction, illustrated in Figure 2.7(a). Similarly, a pin diode is made up of a semiconductor with three adjacent regions where i represents $intrinsic$.

Doping is the act of adding small amounts of electrically active impurities to alter the mobile charge carrier densities and hence the conductivity of the semiconductor. The energy of the highest occupied electron states is called the Fermi energy. n-doping causes an increase in negative charge carrier concentration and in the Fermi energy, while p-doping causes an increase in positive charge carrier concentration and a decrease in the Fermi energy. The doping concentration in a n-type semiconductor is denoted N_{D} (electron donor) and N_{A} (electron acceptor) in a p-type semiconductor, representing the concentration of excess electrons and holes, respectively. For conventional IV semiconductors, like Si and Ge, impurity atoms from group III or V, contributing with an extra hole or an extra electron, are simply added. Doping is more complicated for compound semiconductors like AlGaN where, for example, Mg from group II and Si from group IV can be used [4].

When the two regions are brought together, majority carriers from each region diffuse into the other region due to the excess charge carrier concentration of opposite sign. This results in a depletion region, as all free carriers recombine with donors and acceptors in this region and hence become bound. This causes an electric field from the n-type region to the p-type region, keeping more carriers from migrating to the opposite side of the junction [40, 17, 42]. In Figure 2.7(b) the band diagram for a simple diode is given and the quasi-Fermi levels are illustrated. During forward bias charge carriers are injected. That is, a current flows through the pn-junction, as illustrated in Figure 2.7(a), making the distribution of electrons and holes overlap. Recombination occurs as a spontaneous and statistical process resulting in emission.

The current-voltage characteristics of an ideal diode is given by the Shockley diode equation [41]

$$I = I_s\left(\exp\left(\frac{eV}{nk_BT}\right) - 1\right), \tag{2.2}$$

where e is the elemental charge unit, V is the voltage across the diode, k_B is the Boltzmann constant, T is the temperature and n is the quality factor, typically varying from 1 to 2. The characteristics for LEDs of different elemental composition and hence bandgap are illustrated in Figure 2.8. I_s is the reverse bias saturation current given by [4]

$$I_s = eA\left(\frac{D_n n_i^2}{L_n N_A} + \frac{D_p n_i^2}{L_p N_D}\right), \tag{2.3}$$

where A is the area of the diode, D_n and D_p are the diffusion coefficients of electrons and holes, n_i is the intrinsic carrier concentration of the semiconductor, L_n and L_p are the diffusion lengths and N_D and N_A are the donor and acceptor concentrations in the n-doped and p-doped region. Under equilibrium conditions

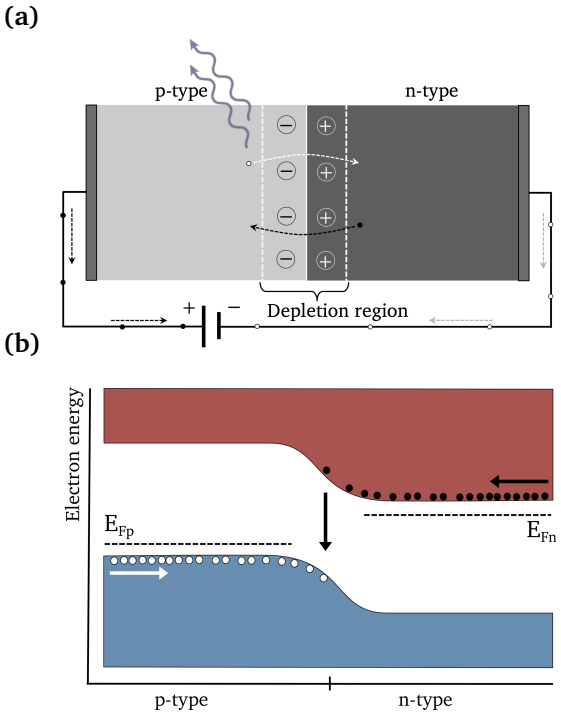

Figure 2.7: (a) Schematic of a simple pn-junction where the direction of the different charge carriers under forward bias has been given and (b) the corresponding band diagram where the quasi-Fermi levels are included. Black spheres represent electrons and white spheres holes. Adapted from [41, 42].

(no applied voltage) the product of the carrier concentrations in any semiconductor is constant, given by the law of mass action [41]. The fraction given by

$$n_{p0} \approx \frac{n_i^2}{N_A} \tag{2.4}$$

is hence an approximation of the electron concentration in the p-region during equilibrium. A similar expression exists for n-type semiconductors. By applying a voltage over the pn-junction the minority carrier concentration increases, as illustrated in Figure 2.9, and a new expression is given by [42]

$$n_{pV} \approx \frac{n_i^2}{N_A} e^{\frac{eV_D}{k_B T}}. \tag{2.5}$$

This makes the probability for radiative recombination (also called spontaneous emission) larger, which can be seen from the following equation, as it is proportional to the product np. The rate of spontaneous emission under the low

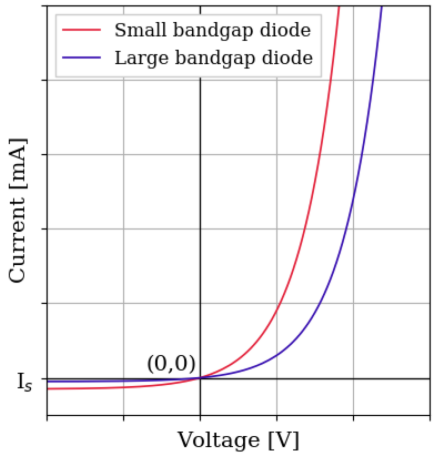

Figure 2.8: Simplified IV-characteristic according to Equation 2.2 for a small bandgap semiconductor and a semiconductor with larger bandgap. A larger bandgap requires higher voltage across the device to turn it on.

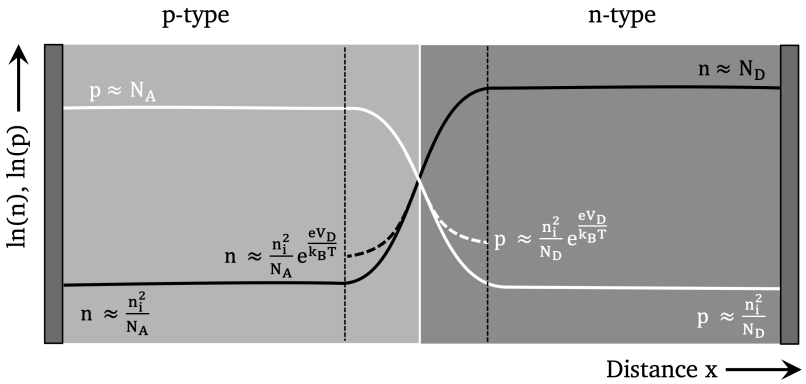

Figure 2.9: Concentration profiles across a pn-junction showing the approximate minority and majority carrier concentrations with (white) and without (black) applied voltage across the junction. Adapted from [24].

injection regime is given by [43]

$$R_s = \frac{1}{2\tau_0}\left(\frac{2\pi\hbar^2 m_r^*}{k_B T m_e^* m_h^*}\right)^{\frac{3}{2}} np, \tag{2.6}$$

where τ_0 is the recombination time, m_r^* is the reduced mass of the electron and hole mass system (m_e^*, m_h^*) and n and p is the concentration of available electrons and holes in the recombination area. Hence, in order to have significant emission rate in a LED both available electrons and holes must be present and these numbers can be increased by doping. Under carrier injection it is common practice to apply

quasi-Fermi levels in order to describe the occupation probability and hence the density of carriers, as the pn-junction no longer is in equilibrium [43]. For electrons and holes the density of carriers during non-equilibrium conditions is given by

$$n = N_{\mathrm{C}} \exp\left[\frac{E_{\mathrm{Fn}} - E_{\mathrm{C}}}{k_{\mathrm{B}}T}\right] \qquad p = N_{\mathrm{V}} \exp\left[\frac{E_{\mathrm{V}} - E_{\mathrm{Fp}}}{k_{\mathrm{B}}T}\right]. \tag{2.7}$$

The occupation probability is dependent on the carrier concentration in the conduction and valence band, N_{C} and N_{V}, the quasi-Fermi level of electrons and holes, E_{Fn} and E_{Fp} and the energy of the conduction and valence band, E_{C} and E_{V}. The quasi-Fermi levels for a pn-junction was illustrated in Figure 2.7(a). The probability for a charge carrier to occupy a state with energy E at temperature T is given by the Fermi-Dirac distribution [43]

$$f(E,T) = \left(\frac{1}{e^{\frac{E-E_{\mathrm{Fi}}}{k_{\mathrm{B}}T}} + 1}\right), \tag{2.8}$$

where E_{Fi} represents the quasi-Fermi level of the electron (E_{Fn}) or the hole (F_{Fp}). Hence, increased doping results in quasi-Fermi levels closer to the band edges and therefore larger probability of, for example, electrons occupying the conduction band.

The spectral characteristics of a LED are given by the emission wavelength, the spectral width and the spectral shape. The wavelength is determined by the bandgap of the semiconductor, related by [41]

$$E_g = \frac{hc}{\lambda}, \tag{2.9}$$

where h is Planck's constant, c the speed of light in vacuum and λ the wavelength of the emitted light. Light emitted by a LED is incoherent, that is, the relative phase of the different waves is random. The spectral width of a LED during electroluminescence can be approximated by [41]

$$\frac{hc}{\Delta\lambda} \approx n k_{\mathrm{B}} T, \tag{2.10}$$

where n is in the interval $\{2, 4\}$. This corresponds to a spectral width in units of nm of approximately 20 - 100 nm. The shape and the width of the emitted spectrum is dependent on many factors, like doping level, injection current, temperature, impurities, etc.

Electrons and holes can recombine either non-radiatively or radiatively. The latter is preferred in LEDs and should be maximised. Band-to-band recombination and Shockley-Read-Hall recombination, also known as trap-assisted recombination, both contribute to radiative recombination. Auger recombination, on the other hand, transfers the energy from the recombination to another electron or hole instead of creating a photon [41]. The different recombination mechanisms are illustrated in Figure 2.10.

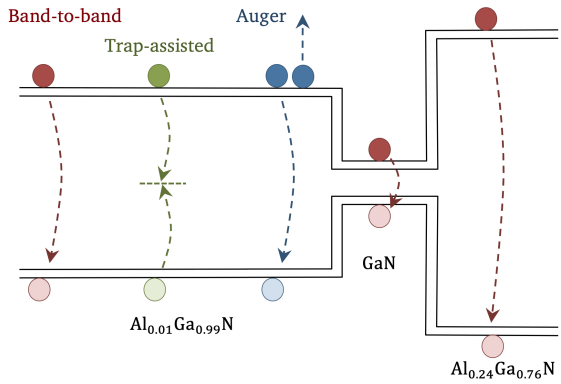

Figure 2.10: Different types of recombination mechanisms across the bandgap. Band-to-band and trap-assisted recombination results in electromagnetic radiation with wavelength according to the bandgap where the recombination occurs. This can be detected by cathodoluminescence (CL). Auger recombination is a non-radiative recombination mechanism. Adapted from [41].

The spontaneous carrier recombination lifetime, which is the time an excess electron-hole pair exists before recombining occurs, is given by

$$\frac{1}{\tau} = \frac{1}{\tau_{\mathrm{R}}} + \frac{1}{\tau_{\mathrm{NR}}}, \tag{2.11}$$

where τ_{R} and τ_{NR} represents radiative and non-radiative recombination lifetimes, respectively. Based on this, efficiency can be approximated according to the ratio τ/τ_R, which is large for high efficiency. Another important efficiency measure is the injection efficiency given by [43]

$$\gamma_{\mathrm{inj}} = \left(\frac{J_n}{J_n + J_p + J_{\mathrm{GR}}} \right). \tag{2.12}$$

This is the ratio between the electron current density (J_n) and the total LED current density made up from the electron and hole current densities (J_n and J_p) and the current density from trap-assisted recombination (J_{GR}).

Some of the more complex LED configurations make use of quantum confinement. This is a means of bandgap tuning through implementation of, for example, quantum wells, as the electronic states are altered relative to the bulk situation [44]. Quantum confinement works by restricting the movement of charge carriers approximately to the de Broglie wavelength of the carriers in one or several dimensions. The effect of this is shifting and discretisation of the energy levels, illustrated in Figure 2.11. The quantum-confined area has a smaller bandgap than the surrounding barrier material, as the purpose is to trap charge carriers to increase radiative emission efficiency [46]. By increasing the density of carriers, the radiative recombination lifetime (τ_R in Equation 2.11) decreases an by altering the size of the confined dimension it is possible to tune the bandgap. This

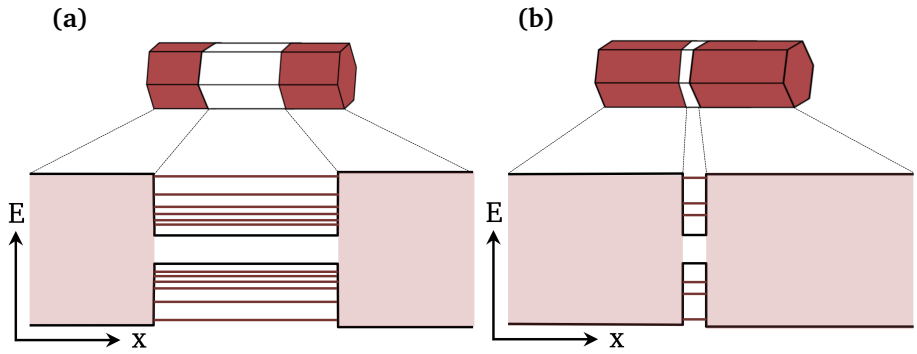

Figure 2.11: Illustration showing how the size of the confinement area alters the energy states for (a) a large confinement area, where the energy of the states are close to continuous and (b) a smaller confinement area or a quantum well, where three discrete states can be seen. The red material has larger bandgap than the white material, such that carriers are confined to the smaller bandgap area. Adapted from [45].

can be understood from the particle in a box approach, which describes electrons by the Schrödinger equation. For confinement to one dimension the Schrödinger equation is given by [47]

$$-\frac{\hbar^2}{2m}\frac{\partial^2\Psi(x,t)}{\partial x^2}+V(x)\Psi(x)=i\hbar\frac{\partial\Psi(x,t)}{\partial t}. \tag{2.13}$$

Here, $\Psi(x)$ is the electron wavefunction and $V(x)$ is the potential the electron is subject to at position x. The general solution of Equation 2.13 for infinite potential outside the box is

$$\Psi(x)=Ae^{-i(\omega t+kx)}, \tag{2.14}$$

where A is a normalisation constant, ω is the angular frequency and k is the wavenumber. The eigenstate energies of Equation 2.13 with the solution given in Equation 2.14 is

$$E_n=\frac{\pi^2\hbar^2n^2}{2m^*w^2}, \tag{2.15}$$

where m^* is the effective mass of the electron and w is the width of the confinement area. Hence, if the size of the confinement area changes, the energy of the states will also change, as can be seen in Figure 2.11. For a finite potential outside the box the solution wavefunction will be extended outside the box, decaying exponentially. This results in smaller eigenstate energies [47].

AlGaN LEDs

III-nitrides were discussed in section 2.1.1 and one of the greatest merits of this material system is the ability to alter the bandgap energy by adjusting the

III-component ratio. An approximation of the bandgap energy of $Al_xGa_{1-x}N$ was given in Equation 2.1 and illustrated in Figure 2.3. For structures like heterojunctions and MQWs in $Al_xGa_{1-x}N$, layers with alternating values of x are simply engineered in a heterostructure with thickness controlled at the nm-scale. In doing so, charge carriers can be localised in the structure. That is, the optical properties of III-nitride LEDs can be tuned by altering the composition and by scaling the size at the nm-scale. Defect related luminescence in GaN is often referred to as yellow luminescence (YL), as the energy transitions correspond to approximately 2.23 eV (~ 540 nm).

For implementation in LEDs, $Al_xGa_{1-x}N$ is commonly doped with Mg for p-doping and Si for n-doping to achieve a pn-junction [4]. These elements are found in the periodic table in group II and IV, respectively. p-doping of GaN has for a long time been problematic and still is. The reason for this is the high activation energy associated with introduction of Mg in GaN. Moreover, this activation energy increases with Al content, which makes it hard to achieve high hole concentration in p-AlGaN with high Al content (see Figure 2.3). This also poses problems when it comes to establishing ohmic contacts [48]. With p-doping the Fermi energy decreases and the formation energy for shallow acceptors also decreases. The Mg_{Ga} acceptor takes a Ga site when introduced in GaN. These states have low ionisation energies (~ 200 meV) and can cause a redshift in the emitted wavelength [2].

The Quantum-confined Stark effect (QCSE) is the effect of an electric field on a quantum-confined state [49]. This phenomenon can cause a decrease in the efficiency of, for example, quantum wells. Due to the polarity of the $Al_xGa_{1-x}N$ compound, a polarisation-induced electric field along the c-axis emerges and causes a redshift in the emitted spectrum. That is, the bandgap is effectively reduced and the spatial electron-hole overlap becomes smaller, hampering the efficiency [48, 49]. The QCSE is illustrated in Figure 2.12.

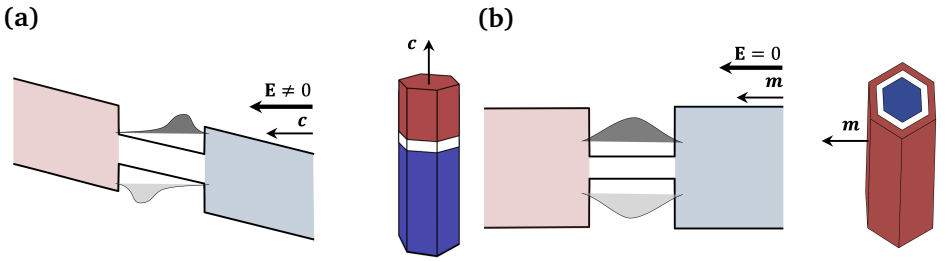

Figure 2.12: (a) Illustration of QCSE along the c-axis of AlGaN. Because $[0001]$ is a polar vector QCSE reduces the wavefunction overlap between electrons and holes. QCSE also effectively reduces the bandgap. (b) For the m-vector perpendicular to the c-vector no such effect should be present as the m-planes are non-polar. Adapted from [49, 48].

In general, when the bandgap energy of a semiconductor making up the LED device increases, the external quantum efficiency (EQE) decreases. This is the case when the mole fraction of Al (x) increases in $Al_xGa_{1-x}N$. Carrier-

transport properties get more asymmetric with increasing bandgap and the hole injection efficiency gets weaker. Ionisation energy and effective mass increases with bandgap. These are some of the problems regarding the efficiency $Al_xGa_{1-x}N$ UV LEDs with high Al content. All these effects cause what has been named an efficiency droop, a significant roadblock in the search for more efficient UV LEDs [50].

2.2 Crystallography

2.2.1 General crystallography

Ideal crystals are made up of infinite repetitions of organised atomic groups. In order to describe specific crystals in real space, lattices are exploited. A lattice is a mathematical concept describing the distribution of points in three-dimensional space using three translation vectors. In a primitive lattice all points are equivalent, such that any vector combination translates into an identical position. Such a lattice is called a Bravais lattice and any point is given by [17]

$$\boldsymbol{R} = m\boldsymbol{a_1} + n\boldsymbol{a_2} + o\boldsymbol{a_3}. \tag{2.16}$$

Here, m, n and o represent arbitrary integers, $\boldsymbol{R}$ is any point in the Bravais lattice and $\boldsymbol{a_1}, \boldsymbol{a_2}$ and $\boldsymbol{a_3}$ represent the primitive translation vectors. The latter span out a parallelepiped shown in Figure 2.13(a), which constitutes the unit cell [40]. The

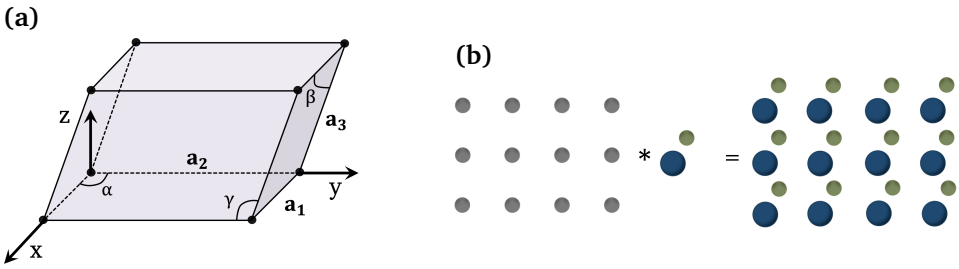

Figure 2.13: (a) Parallelepiped unit cell made from the translation vectors $\boldsymbol{a_1}$, $\boldsymbol{a_2}$ and $\boldsymbol{a_3}$ with angle relations α, β and γ. (b) Illustration of a basis on a finite lattice giving a crystal, where $*$ is a convolution in real space, which corresponds to a multiplication in reciprocal space. Adapted from [17, 40].

smallest repetitive unit is called the basis of the lattice and may consist of more than one element, in which case the position of atom j relative to its lattice point is given by

$$\boldsymbol{r_j} = x_j\boldsymbol{a_1} + y_j\boldsymbol{a_2} + z_j\boldsymbol{a_3}. \tag{2.17}$$

Here, $0 \leq x_j, y_j, z_j \leq 1$ [17]. In order to construct the complete crystal, the basis is repeated at each lattice point, as illustrated in Figure 2.13(b).

In three-dimensional space there are 14 different types of Bravais lattices with characteristic symmetries. They are characterised by the length of the translation vectors ($|\mathbf{a_1}|, |\mathbf{a_2}|, |\mathbf{a_3}|$) and their angle relations (α, β, γ). These 14 Bravais lattices are categorised in seven different systems; triclinic, monoclinic, orthorhombic, tetragonal, cubic, trigonal and hexagonal [17]. The latter will be discussed in more detail in section 2.2.2.

When studying periodic structures it is common to perform a Fourier analysis. Fourier transforms are mathematical operations that represent periodic structures in reciprocal lattices with the general form for the function $f(x)$ given by [51]

$$\hat{f}(\epsilon) = \int_{-\infty}^{\infty} f(x) e^{-2\pi i x \epsilon} dx. \tag{2.18}$$

The function to be transformed is multiplied by a complex exponential and integrated over all space. This representation is related to the periodic structure like frequency is related to time. The Fourier transform decomposes the real space lattice into its different spatial frequency components and is closely related to diffraction, discussed in section 2.3.

The unit for length in reciprocal space is the inverse of real space, and the reciprocal lattice is defined by the primitive vectors [17]

$$\boldsymbol{b_1} = 2\pi \frac{\boldsymbol{a_2} \times \boldsymbol{a_3}}{\boldsymbol{a_1} \cdot \boldsymbol{a_2} \times \boldsymbol{a_3}} \ , \ \boldsymbol{b_2} = 2\pi \frac{\boldsymbol{a_3} \times \boldsymbol{a_1}}{\boldsymbol{a_1} \cdot \boldsymbol{a_2} \times \boldsymbol{a_3}} \ , \ \boldsymbol{b_3} = 2\pi \frac{\boldsymbol{a_1} \times \boldsymbol{a_2}}{\boldsymbol{a_1} \cdot \boldsymbol{a_2} \times \boldsymbol{a_3}}. \tag{2.19}$$

As for the real space lattice, any point in reciprocal space can be translated into by

$$\boldsymbol{G} = h\boldsymbol{b_1} + k\boldsymbol{b_2} + l\boldsymbol{b_3}, \tag{2.20}$$

where $\boldsymbol{G}$ is the reciprocal lattice vector and (hkl) is the Miller indices [17]. By the Miller notation a plane given by (hkl) in real space intersects $\boldsymbol{a_1}, \boldsymbol{a_2}$, and $\boldsymbol{a_3}$ at 1/h, 1/k and 1/l, respectively [40]. In general, the distance between two parallel planes given by (hkl) is

$$d_{\text{hkl}} = \frac{2\pi}{|\boldsymbol{G}_{\text{hkl}}|}, \tag{2.21}$$

where $\boldsymbol{G}$ is the reciprocal vector [52]. A useful relation for diffraction theory is [17]

$$\boldsymbol{b_i} \cdot \boldsymbol{a_j} = 2\pi\delta_{ij}, \tag{2.22}$$

where δ_{ij} is the Kronecker delta. This equation is used for calculation of the selection rules discussed in section 2.3.1.

2.2.2 The hexagonal crystal system

The relevant crystal system for this work is the hexagonal one, which is recognised by $|a_1|=|a_2|\neq|a_3|$ and $\gamma=120°$, illustrated in Figure 2.14(a). Hexagonal close-packed (HCP) structures consist of identical spheres packed with maximum density [17]. WZ is the name adapted for binary hexagonal crystal structures where two

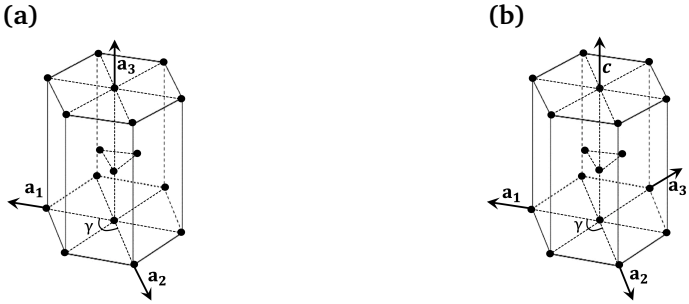

Figure 2.14: (a) Conventional hexagonal crystal indices (hkl) and (b) Miller-Bravais hexagonal crystal indices (hkil). Adapted from [53].

hexagonal structures shifted by $(0\ 0\ \frac{3}{8})$ make up the system [43]. Additionally, it is possible to alloy WZ crystal systems with a third element. For GaN this is done by replacing some of the atoms of the III-element (Ga) with another element in group III, such as Al, to form $\mathrm{Al}_x\mathrm{Ga}_{1-x}\mathrm{N}$ [4]. The resulting change in bandgap is described by Equation 2.1 and depicted in Figure 2.3.

It is common to introduce the Miller-Bravais notation for hexagonal crystal systems by adding a fourth, seemingly redundant, axis (hkil). This is shown in Figure 2.14(b), where the new translation vectors are named $\boldsymbol{a_1}, \boldsymbol{a_2}, \boldsymbol{a_3}$ and $\boldsymbol{c}$. The purpose of this is to more easily recognise symmetry equivalent directions, illustrated in Figure 2.15. Miller-Bravais indices are related by [53]

$$h + k + i = 0 \Rightarrow i = -(h + k). \tag{2.23}$$

The most important compound semiconductors, such as GaN, ZnO and GaAs, adapt either WZ or Zinc blende (ZB) crystal structure, where the latter is the cubic equivalent of WZ [41]. ZB has a face-centred cubic (FCC) crystal structure with a basis consisting of two atoms displaced by $(\frac{1}{4}\frac{1}{4}\frac{1}{4})$. For identical atoms the diamond structure results, exhibited by Si and Ge. The close-packed direction for ZB is $[111]$. WZ and ZB are distinguished by the packing order, which for WZ is ABAB in $[0001]$ and ABCABC in $[111]$ for ZB [17]. The packing sequences are illustrated in Figure 2.16.

For the hexagonal case the distance between parallel planes is found from [52]

$$d_{\mathrm{hkl}} = \left[\frac{4}{3}\left(\frac{h^2 + hk + k^2}{a_1^2}\right) + \frac{l^2}{a_3^2}\right]^{-1/2}, \tag{2.24}$$

where (hkl) are the conventional hexagonal indices. The lattice constants for pure GaN and AlN are listed in Table 2.1 [4] and the positions of the basis atoms (defined in Equation 2.17) are for a III-V semiconductor given in hexagonal indices (hkl) as [54]

$$\boldsymbol{r}_{\mathrm{III}} = \left\{(0,0,0), \left(\frac{2}{3}, \frac{1}{3}, \frac{1}{2}\right)\right\} \qquad \boldsymbol{r}_{\mathrm{V}} = \left\{\left(0,0,\frac{3}{8}\right), \left(\frac{2}{3}, \frac{1}{3}, \frac{7}{8}\right)\right\}. \tag{2.25}$$

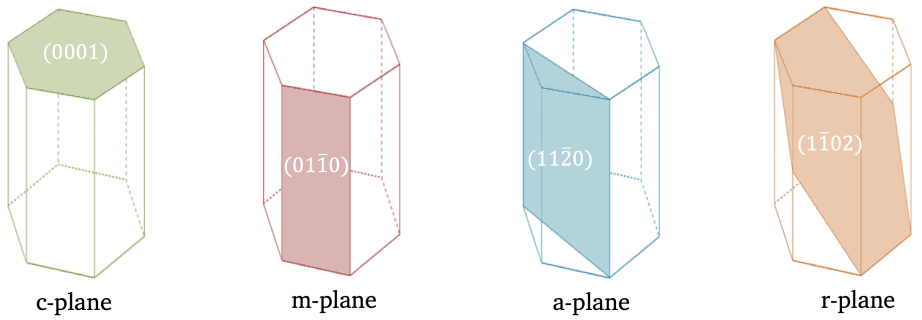

Figure 2.15: Different planes in the hexagonal crystal system with indicated Miller-Bravais notation. The c-planes are polar, the m- and a-planes are non-polar and the r-planes are semi-polar. Adapted from [48, 16].

The angle between the c-plane and the r-plane, given by α in Figure 2.17(a), is

$$\alpha = \arctan\left(\frac{2c}{\sqrt{3}a}\right), \tag{2.26}$$

which is approximately 62° for both AlN and GaN. The r-planes sometimes make up the top facets of structures like NWs, resulting in an angle of 152° with the m-planes, represented by γ in Figure 2.17(b).

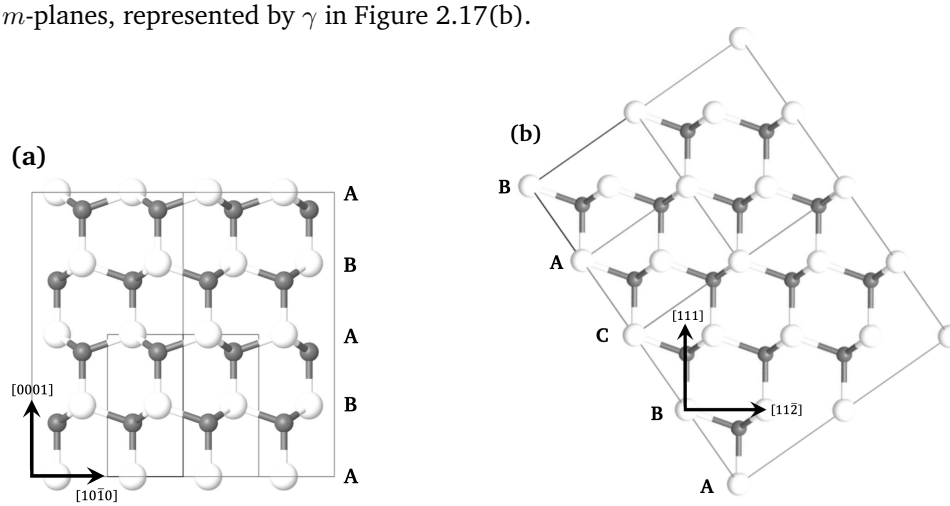

Figure 2.16: Stacking sequence of Ga (white) and N (grey) for (a) WZ and (b) ZB along [0001] and [111], respectively. The lattice is simulated in JEMS with basis position parameters as given above.

WZ is a noncentrosymmetric crystal structure with one polar axis along [0001], illustrated in Figure 2.15 [31]. This means that the distribution of charge

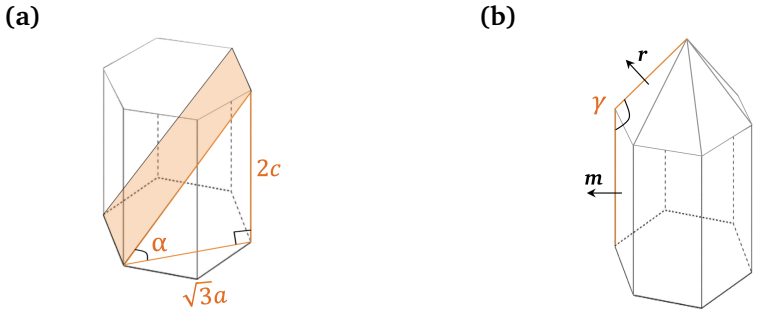

Figure 2.17: (a) Hexagonal structure where the orange plane represents the r-plane. The angle between the c-plane and the r-plane (α) is shown. For WZ crystal structures r-planes and the m-planes are often displayed, as illustrated in (b). The angle between the two planes (γ) depends on the lattice constants a and c.

Table 2.1: Lattice constants for AlN and GaN [55, 4]. From Figure 2.3 it is found that for an AlGaN alloy a decreases and bandgap energy increases with Al content.

Lattice parameter	AlN [Å]	GaN [Å]	Deviation[1] [%]
a	3.111	3.189	2.51
c	4.978	5.185	4.16

[1] $\left(\frac{a_{GaN}-a_{AlN}}{a_{AlN}}\right) \times 100\%$.

contributes to a polarisation pointing along the c-axis. The m- and a-planes are non-polar and the r-planes are semi-polar. Polar c-planes of Ga (0001) and non-polar a-planes $(10\bar{1}0)$ can be seen in Figure 2.16(a). Due to the noncentrosymmetry of the WZ crystal structure it also exhibits piezoelectric polarisation [31]. That is, the polarisation changes due to strain present in the structure, or the other way around. Nitrides show especially strong spontaneous polarisation due to the polarity of the III-V bond, which might have an impact on the strain and the free carrier distribution in the material. Asymmetric excitation probability has been observed with convergent-beam electron diffraction (CBED) by L. H. G. Tizei et al. in GaN/AlN heterostructures [56].

2.3 Diffraction

2.3.1 General diffraction

When a travelling wave hits an obstacle or an opening, it is scattered in space according to Huygens principle [52]. The points along the wavefront constitute point sources of new waves, which subsequently interfere and eventually result in a pattern due to constructive interference at certain locations. Constructive interference happens where the wave crests of both sources coincide. If the

obstacle is periodically structured, the resulting interference pattern will show periodical effects. This phenomenon is called diffraction and applies to any obstacle or opening hit by a wave of appropriate wavelength. Bragg's law of diffraction is based on specular reflection of waves from adjacent planes of spacing d. In order for plane waves incident at angle θ reflecting off of succeeding parallel planes to be in phase and thereby constructively interfere, the path difference $AB + BC$ in Figure 2.18 must be some integer times the wavelength [57]

$$2d \sin \theta_{\mathrm{B}} = n\lambda. \tag{2.27}$$

Here n is an integer, λ is the wavelength, d is the interplanar spacing and θ_B is the diffraction angle. Therefore, given that the applied wavelength is known, the spacing in a crystal can be calculated by measuring θ_B. The latter can be found from the recorded diffraction pattern and the geometry of the set-up. Bragg's law is based on kinematical diffraction theory, hence multiple and inelastic scattering is neglected. The theory builds on single coherent scattering and is used in order to explain the intensity and the location of spots in a diffraction pattern [58]. The scattering intensity depends on the type and distribution of atoms in the basis, that is, the spatial distribution of electrons in the sample. As the electron

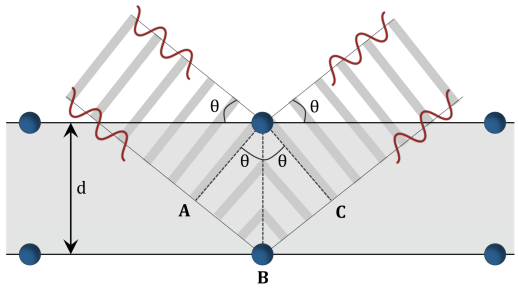

Figure 2.18: Bragg reflection illustrated for parallel planes of spacing d for incident plane waves at an angle θ. When $AB + BC$ equals an integer times the wavelength, constructive interference occurs as the reflected waves are in phase. Adapted from [58, 57].

number density ($n(\boldsymbol{r})$) varies for different atoms, an atomic form factor (f_j) is used to account for the difference in scattering amplitude[2]. Higher atomic number indicates higher electron number density. For atom j the atomic scattering factor is defined as [17]

$$f_j = \int n_j(\boldsymbol{\rho}) e^{(-i\boldsymbol{G}\cdot\boldsymbol{\rho})} dV, \tag{2.28}$$

with $\boldsymbol{\rho}$ representing the vector between the lattice point and atom j ($\boldsymbol{\rho} = \boldsymbol{r} - \boldsymbol{r_j}$, from Equation 2.17) and $\boldsymbol{G}$ is defined in Equation 2.20. Atomic scattering factor is often conveniently expressed as a function of scattering angle ($f(\theta)$)

[2]The description for X-ray scattering is used here, as it is the most instructive. X-rays scatter on electron clouds, whereas electrons scatter on the nucleus, which is screened by the electron cloud. The same description is used, but instead of n($\boldsymbol{r}$) it is the inner potential the electron detects. Electron specific deviations are addressed in section 2.3.2.

for the purpose of diffraction pattern interpretation. The magnitude decreases with scattering angle and wavelength of the incident beam. The total scattering amplitude (F_G) is given by the product of the combined scattering factor for all atoms in the crystal (the structure factor, S_G) and the number of unit cells (N) [17]

$$F_{\mathrm{G}} = NS_{\mathrm{G}} = N\sum_j f_j e^{(-i\boldsymbol{G}\cdot\boldsymbol{r_j})}, \tag{2.29}$$

where $\boldsymbol{r_j}$ is defined in Equation 2.17. The observed intensity of a diffraction pattern is proportional to the squared magnitude of the scattering amplitude ($I \propto |F_{\mathrm{G}}|^2$) [17]. From the relation given in Equation 2.22 we find that the sum in Equation 2.29 can be written as

$$F_{\mathrm{G}} = N\Big(f_j e^{-2\pi i(x_j h + y_j k + z_j l)} + f_{(j+1)} e^{-2\pi i(x_{(j+1)} h + y_{(j+1)} k + z_{(j+1)} l)} + ...\Big), \tag{2.30}$$

where (hkl) are the Miller indices of the diffracting plane. There is a possibility of having $F_{\mathrm{G}} = 0$, in which case the specific reflection is said to be kinematically forbidden and no diffraction intensity is produced. When $F_{\mathrm{G}} \neq 0$ the reflection is said to be kinematically allowed and a diffraction spot can appear [58]. By accounting for all possible combination of h, k and l the diffraction conditions can be found.

The scattering intensity for GaN, using the atomic positions found in section 2.2.2, is found to be

$$\begin{aligned} f_{\mathrm{hkl}} &= f_{Ga}\Big(1 + e^{-2\pi i(\frac{2}{3}h + \frac{1}{3}k + \frac{1}{2}l)}\Big) + f_N\Big(e^{-2\pi i(\frac{3}{8}l)} + e^{-2\pi i(\frac{2}{3}h + \frac{1}{3}k + \frac{7}{8}l)}\Big) \\ &= \Big(1 + e^{-2\pi i(\frac{2}{3}h + \frac{1}{3}k + \frac{1}{2}l)}\Big)\Big(f_{Ga} + f_N e^{-i\pi\frac{3}{4}l}\Big) = S_{\mathrm{HCP}}\Big(f_{Ga} + f_N e^{-i\pi\frac{3}{4}l}\Big). \end{aligned}$$

From this expression it can be seen that WZ has the same selection rules as HCP, as the final parenthesis never equals zero. This is because $f_{Ga} > f_N$ and $-1 \leq e^{-i\pi\frac{3}{4}l} \leq 1$, hence the final parenthesis will only have an effect on the intensity. Taking advantage of the selection rules for the ideal HCP structure [58] and defining the atomic scattering factor for the III components in AlGaN as

$$f_{\mathrm{III}} = (1-x)f_{Ga} + xf_{Al},$$

we get the following kinematically forbidden and allowed reflections for $\mathrm{Al}_x\mathrm{Ga}_{1-x}\mathrm{N}$ [59]:

$$|f_{\text{hkl}}|^2 = \begin{cases} 0 & l \text{ odd}, h-k=3n \\ 3\Big(\big((1-x)f_{Ga}+xf_{Al}\big)^2 \pm & \\ \quad \sqrt{2}\big((1-x)f_{Ga}+xf_{Al}\big)f_N + f_N^2\Big) & l \text{ odd}, h-k\neq 3n \\ 4\Big(\big((1-x)f_{Ga}+xf_{Al}\big)^2 + f_N^2\Big) & l=4m+2, h-k=3n \\ \big((1-x)f_{Ga}+xf_{Al}\big)^2 + f_N^2 & l=4m+2, h-k\neq 3n \\ 4\Big(\big((1-x)f_{Ga}+xf_{Al}\big)^2 \pm f_N^2\Big) & l=4m, h-k=3n \\ \big((1-x)f_{Ga}+xf_{Al}\big)^2 \pm f_N^2 & l=4m, h-k\neq 3n \end{cases}$$

2.3.2 Electron diffraction

Due to the discovery of their wave nature by de Broglie [60], electrons can be exploited in diffraction in line with photons for X-ray diffraction (XRD). The motivation behind the transition from photons to electrons is the enhanced resolution provided due to the short wavelength of accelerated electrons. Electron diffraction can be performed in a TEM, but unlike XRD, where the photons are reflected off planes in a specular manner, the accelerated electrons in the TEM beam are transmitted through the sample. Because electrons interact more strongly with matter compared to photons, multiple and inelastic scattering events are likely to occur. Therefore, the kinematic theory as described above might not be sufficient to describe diffraction by electrons, but can be a useful first approximation [58].

The conditions for electron diffraction in TEM is often given by the Laue equations and is related to the reciprocal space, introduced in section 2.2.1. When an incident wave $\boldsymbol{k_I}$ is scattered, the following diffracted wave results [17]

$$\boldsymbol{k_D} = \boldsymbol{k_I} + \boldsymbol{\Delta k}. \tag{2.31}$$

Here, $\boldsymbol{\Delta k}$ is the scattering vector. The conditions for diffraction can be illustrated with an Ewald sphere shown in Figure 2.19. The Laue equations tell us that if the scattering vector equals any vector combination in reciprocal space, diffraction occurs [17]

$$\Delta \boldsymbol{k} = \boldsymbol{G}. \tag{2.32}$$

Equation 2.32 can equivalently be expressed in three separate equations

$$\boldsymbol{a} \cdot \Delta \boldsymbol{k} = 2\pi h, \tag{2.33}$$

$$\boldsymbol{b} \cdot \Delta \boldsymbol{k} = 2\pi k, \tag{2.34}$$

$$\boldsymbol{c} \cdot \Delta \boldsymbol{k} = 2\pi l. \tag{2.35}$$

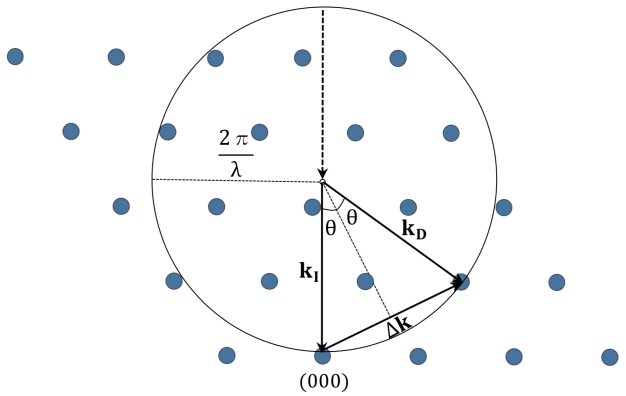

Figure 2.19: Ewald sphere illustrating the Laue condition for diffraction. The beam or the specimen can be tilted in order to change the diffraction conditions. Adapted from [17, 58].

Because the scattering is assumed elastic we have that

$$|\boldsymbol{k_I}| = |\boldsymbol{k_D}| = \frac{2\pi}{\lambda}. \tag{2.36}$$

Bragg diffraction is just a special case of Laue diffraction, where the three conditions are reduced to one in Bragg's law due to specular geometry [40]. This can be seen from

$$|\boldsymbol{k_D} - \boldsymbol{k_I}| = \frac{2}{\lambda} \sin\theta_B. \tag{2.37}$$

Until now we have assumed kinematical diffraction and a perfect infinite crystal structure. However, due to strong coulombic interaction with matter, dynamical effects occur for diffracting electrons, as scattering is strong and likely to happen multiple times unless the sample is extremely thin. This makes it harder to interpret the resulting image. Double diffraction in dynamical diffraction theory can, for example, contribute to diffraction intensity at kinematically forbidden reflections. That is, reflections can occur from hkl-planes where the scattering amplitude should be zero according to the selection rules. This happens when the double-diffracted beam is not characteristic for the relevant reciprocal lattices. Double diffraction is illustrated for WZ in Figure 2.20(a) [58].

A TEM sample typically has a thickness of approximately < 100 nm, resulting in diffraction spots that are spread in accordance with the relationship between distances in real space and reciprocal space. This results in rod-shaped spots in the diffraction pattern, known as reciprocal lattice rods (relrods), illustrated in Figure 2.21. This dynamical scattering effect makes the conditions for diffraction less strict. It is common to introduce a deviation parameter called the excitation error ($\boldsymbol{s}$), related to the scattering vector by [58]

$$\Delta\boldsymbol{k} = \boldsymbol{G} + \boldsymbol{s}. \tag{2.38}$$

The excitation error represents the deviation from Bragg's diffraction condition. It is defined as positive when $\mathbf{G}$ is inside the Ewald sphere and negative when $\mathbf{G}$ is

outside the Ewald sphere. This is relevant for the contrast observed in conventional TEM (see section 2.4.3).

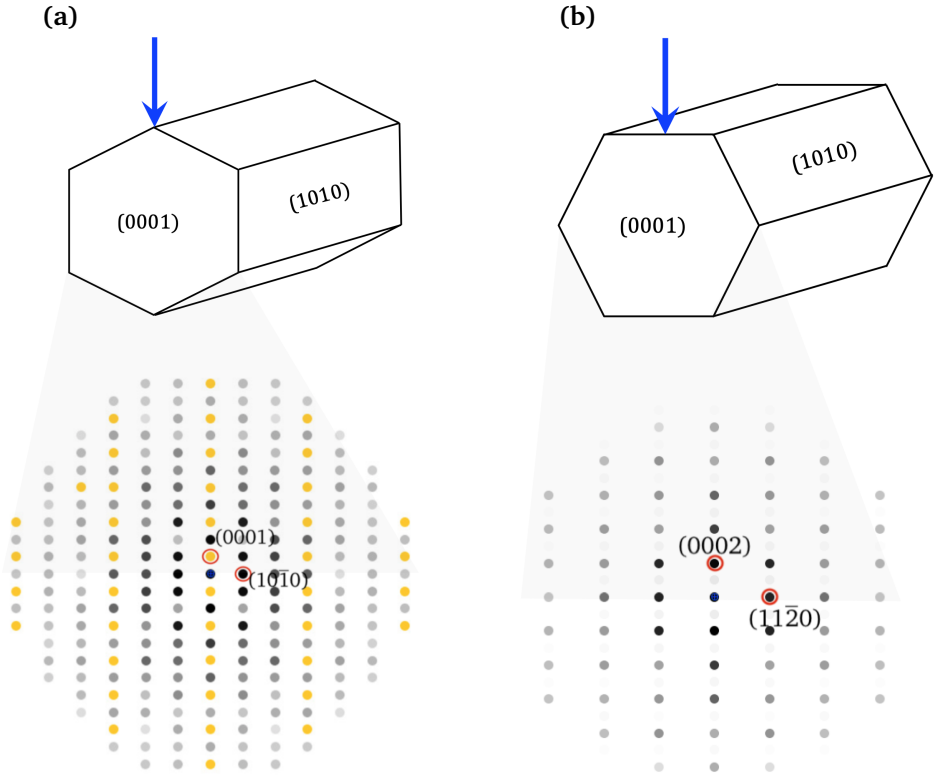

Figure 2.20: Different diffraction features for the WZ crystal structure. (a) Diffraction pattern from zone axis $[11\bar{2}0]$ showing kinematically forbidden reflections indicated with yellow spots and schematic indicating the orientation of the NW. (b) Diffraction pattern from zone axis $[01\bar{1}0]$ and the corresponding NW orientation [3].

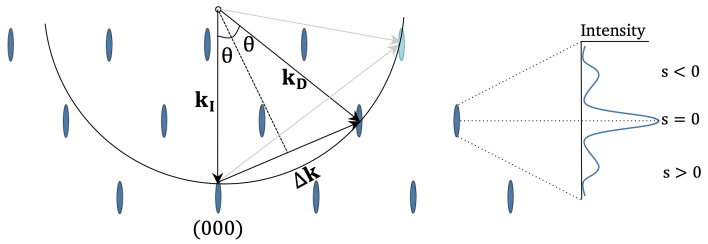

Figure 2.21: Deviation from Bragg's diffraction condition illustrated with excitation error. The grey arrows indicate an additional diffraction condition caused by the relrod-shaped diffraction spots. The intensity profile of a relrod is proportional to the sinc-function squared, as illustrated. Adapted from [58].

[3] For WZ GaAs NWs facets are rotated 30 degrees [61, 62].

2.4 Transmission electron microscopy

The TEM is a powerful characterisation tool able to extract information down to the atomic level. This can provide knowledge about single atoms and how they are arranged in a specimen. In using electrons, instead of photons like visible light microscopes (VLM), higher resolution is achieved because accelerated electrons demonstrate shorter wavelengths, as they are not limited by the Rayleigh criterion. The direct interpretable resolution of TEM is, however, limited to approximately 0.5 Å (for state-of-the-art machines with correction) by instability and aberrations from the lenses. Machines with no correction for spherical aberrations can reach a resolution of about 2 nm [58].

The TEM has two different modes of operation, depending on what part of the beam along the optical axis is projected onto the viewing screen. Imaging mode projects a magnified image of the specimen onto the viewing screen and recording medium, whereas diffraction mode projects the back focal plane onto the viewing screen revealing the diffraction pattern. TEM is based on similar principles as the traditional VLM, but various signal mechanisms are exploited and care must be taken when interpreting the resulting images. They are in fact two-dimensional images of three-dimensional specimens as a result of image formation through transmission. The result is for the same reason affected by a range of different features across the thickness of the specimen [58], which optimally should be less than approximately 100 nm to have a decent elastic transmitted signal. Restricted sampling is another limitation, making it a quantitative method only for a limited volume, and additionally, the high energetic beam of electrons alters the studied specimen to some degree. The theory in this section is mainly based on Williams & Carter, Transmission Electron Microscopy [58].

2.4.1 The instrument

A TEM consists of an electron gun to generate electrons, a range of lenses to focus or project the beam, apertures that restrict what part of the beam is used, stigmators compensating for astigmatism, deflectors that shift and tilt the beam, a specimen holder and detectors, depicted in Figure 2.22. The electron gun produces high-energy electrons by either thermal emission or field emission, and these electrons are commonly accelerated corresponding to 100-300 kV. Further down the TEM column condenser lenses follow. The condenser lenses control the convergence of the electron beam, that is, they condense the beam diameter and limit the beam current. These lenses can be operated by a parallel beam or a convergent beam. Parallel beam mode is used for TEM imaging and selected-area electron diffraction (SAED). A convergent beam is exploited in scanning TEM (STEM) and CBED. Together, the gun and the condenser lenses make up the illumination system. Next follows the specimen stage and the objective lens. The latter is responsible for selecting electrons contributing to contrast formation (by selecting a beam with an aperture) and is considered the most essential lens in the TEM. Finally, the intermediate and diffraction lenses magnify the image and the projector lens eventually projects the result onto the viewing screen, in

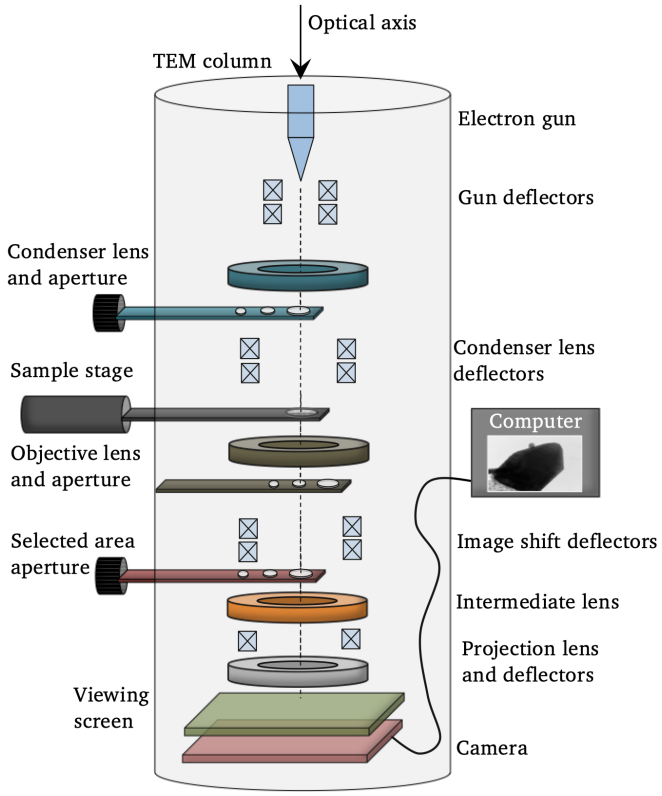

Figure 2.22: Schematic of a TEM showing the main constituents. The different pumps responsible for vacuum conditions are not included. Adapted from [58, 63].

what is called the imaging system of the TEM. Additionally, stigmators are present for the condenser and objective lenses to compensate for astigmatism caused by deformation of the beam by the lenses. The most advanced TEMs also have complex aberration-correction systems inserted in the column. These systems counter balance spherical aberrations that limit the spatial resolution in the TEM, or the smallest probe size in convergent beam mode.

2.4.2 Electron-matter interaction

In electron microscopy, understanding the interactions between electrons and matter is vital in order to extract valid information from the data. Figure 2.23 illustrates a range of possible outcomes when an incident electron interacts with a thin specimen. This section will focus on electron interaction in TEM. However, many aspects are relevant for SEM, STEM and CL as well, discussed in section 2.5, 2.6 and 2.7, respectively.

Electron interaction signals are divided into two categories, depending on

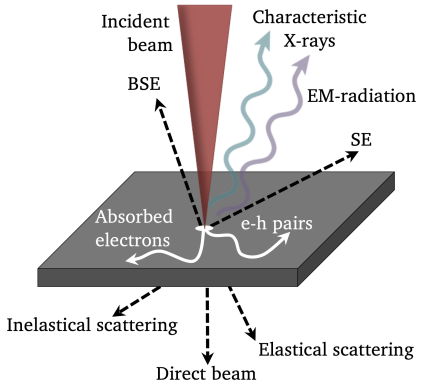

Figure 2.23: Signals emerging from a thin sample when an electron beam is incident on its surface. These include secondary and backscattered electrons (SEs and BSEs), electromagnetic radiation and elastically or inelastically transmitted electrons. Electrons can also get absorbed in the sample. Adapted from [58].

whether or not the electron loses energy upon impact, that is, if the collision is inelastic or elastic. Elastically scattered electrons are often coherent while inelastically scattered electrons are incoherent. The incident beam can, for example, be transmitted directly through a specimen more or less without losing energy, or on the contrary, be completely backscattered. Accelerated electrons constitute a type of ionising radiation known to interact strongly with matter. Hence, it is possible for the incident electron to generate secondary signals, like characteristic X-rays, electromagnetic radiation or secondary electrons (SEs). Most of the secondary signals are utilised in analytical electron microscopy (AEM). The main signal mechanism exploited in TEM stems from transmitted electrons, either forming the direct beam or scattering elastically or inelastically away from the direct beam.

The concept of an interaction cross section (σ) is used in order to describe the probability for an electron-atom interaction. The interaction cross section for a specific atom depends on the energy of the incident electron beam, the atomic number and the thickness and orientation of the atom. The unit for interaction cross section is barn, that is $(10^{-5}\text{nm})^2$, and the interaction probability is found by dividing by the area of the atom. Hence, the larger cross section the greater the probability of interaction. In TEM we are interested in how the interaction cross section changes with the scattering angle (θ), or equivalently solid angle (Ω). This quantity, called differential cross section, describes the angular distribution of the scattered electrons and is related to the atomic scattering factor discussed in section 2.4.1 by [58]

$$|f(\theta)|^2 \propto \left(\frac{d\sigma(\theta)}{d\Omega}\right). \tag{2.39}$$

When a beam of electrons is incident on a crystalline surface, electron channelling has a certain interaction cross section depending on the orientation of the

crystalline specimen and the settings on the microscope. If the crystalline specimen is close to a suitable zone axis the electrons will have a larger interaction cross section for the event of channelling through the entire specimen. This dictates interaction depth and hence contrast in the resulting image.

The main signals that will be exploited in this work are forward scattered elastic electrons, incoherent quasi-elastically scattered electrons, quasi-elastically backscattered electrons (BSE), SEs, X-rays from core-excitations and visible light caused by radiative electron-hole recombination.

2.4.3 Imaging modes and contrast mechanism

Bright-field imaging
Bright-field (BF) imaging is performed by using the objective aperture to select the unscattered electrons for contrast formation. That is, electrons scattered over a certain angle after transmission are subsequently excluded from the beam. The resulting image appears dark where electrons are scattered or absorbed by the aperture and bright anywhere the direct beam is transmitted. This is illustrated in Figure 2.24 (a) and an example of a BF TEM image is given in Figure 2.25(a).

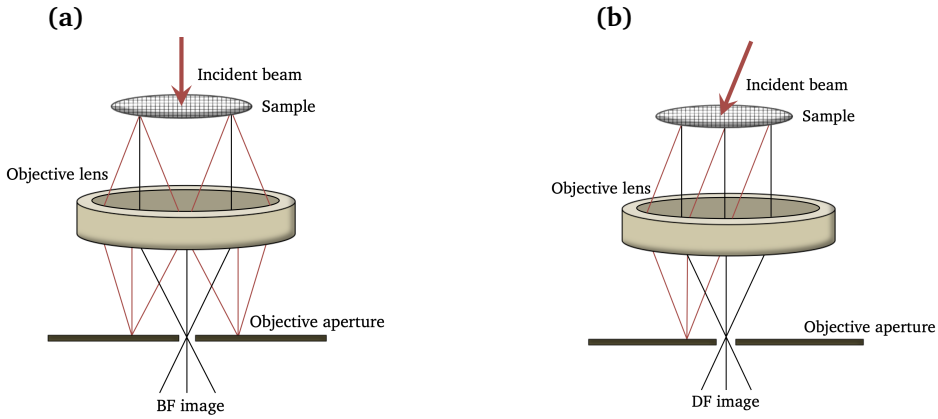

Figure 2.24: (a) Illustration of BF imaging where the electrons transmitted through the sample with no scattering angle make up the final image. (b) Illustration of DF imaging where the electrons transmitted with a certain scattering angle from the sample make up the final image. Adapted from [58].

Dark-field imaging
Images formed by dark-field (DF) TEM utilise the scattered electrons for contrast formation. This is done by selecting a scattered beam with the objective aperture, thereby excluding the direct beam. The resulting image appears dark where the direct beam or other reflections are transmitted, for example in vacuum, and bright where the scattered beam selected with the objective aperture is transmitted. The image holds thereby direct orientation information and can confirm, for example,

difference in orientation between two adjacent grains. DF imaging is illustrated in Figure 2.24 (b) and an example of a DF TEM image is given in Figure 2.25(b).

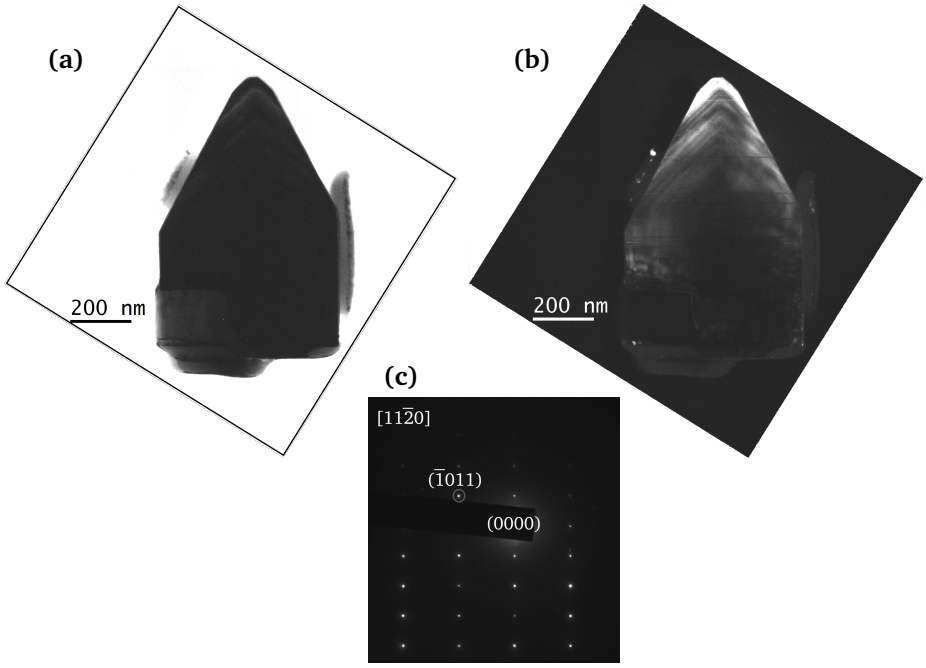

Figure 2.25: (a) BF TEM image from the (0000) reflection and (b) DF TEM image from the ($\bar{1}011$) reflection of the same NW. Basal-plane stacking faults (BSFs) can be seen in (b). In (c) the corresponding diffraction pattern can be seen were ($\bar{1}011$) (DF) is shown and (0000) (BF) is covered by the beam block.

Mass-thickness contrast

Mass-thickness contrast results from incoherent elastic scattering of electrons. The cross section is given by

$$\sigma_R(\theta) = \frac{Z^2 e^4 d\omega}{16(4\pi\epsilon_0 E_0)^2 \sin^4(\theta/2)}, \tag{2.40}$$

where σ_R is the differential cross section at scattering angle θ, Z is the atomic number, e is the elemental charge, ϵ_0 is the vacuum permittivity, E_0 is the energy of the incident electron in keV and $d\omega$ represents the solid angle. Additionally, it is known that the derivative of σ_R with respect to ω is proportional to the intensity. At low angles this contrast mechanism competes with Bragg-diffraction, however, for amorphous parts only mass-thickness contrast is seen. Thicker areas or areas of higher atomic number scatter more and hence appear darker in BF TEM. For

higher angles, mass-thickness contrast dominates, which is exploited in HAADF STEM (discussed in section 2.6.2.)

Thickness fringes

TEM samples can have a non-uniform thickness across their area and, since TEM imaging is based on averaging data collected across the thickness of a sample, effects of this non-uniformity can be seen in TEM images. Thickness fringes are a result of complementary oscillations in the intensity of the direct and diffracted beam, illustrated in Figure 2.26. They are interpreted similarly to a contour map, where joint points represent equal elevation or thickness. This is a phase effect with periodically occurring constructive and destructive interference. The amplitude of a diffracted beam is given by

$$\phi_{\boldsymbol{g}} = \frac{\pi z i}{\xi_{\boldsymbol{g}}} \sum_n e^{-2\pi i \boldsymbol{\Delta k} \cdot \boldsymbol{r_N}} e^{-2\pi i \boldsymbol{k_D} \cdot \boldsymbol{r}}, \tag{2.41}$$

where z is the thickness of the specimen, N is the number of unit cells and $\xi_{\boldsymbol{g}}$ is a characteristic extinction length, expressed by

$$\xi_{\boldsymbol{g}} = \frac{\pi V_c \cos\theta_B}{\lambda F_{\boldsymbol{g}}}. \tag{2.42}$$

This parameter represents the beating length of the direct and the scattered beam and depends on the volume of the unit cell (V_c), the diffraction angle (θ_B), the wavelength of the incident electron beam (λ) and the total scattering amplitude ($F_{\boldsymbol{g}}$) from Equation 2.29. The total wave function transmitted through the specimen can be written as a sum using the principle of superposition

$$\Psi = \phi_{\mathbf{0}} e^{2\pi i \chi_{\mathbf{0}} \cdot \boldsymbol{r}} + \phi_{\boldsymbol{g_1}} e^{2\pi i \chi_{\boldsymbol{g_1}} \cdot \boldsymbol{r}}, \tag{2.43}$$

where all diffracted beams except for one, denoted $\boldsymbol{g_1}$, are omitted, using a two-beam approximation. $\phi_{\mathbf{0}}$ represents the direct beam. In Equation 2.43 the wave vectors are expressed as $\chi_{\mathbf{0}}$ and $\chi_{\boldsymbol{g_1}}$ as the wave function is considered in vacuum and not inside the crystal. From Equation 2.41 we can see that the amplitude of the diffracted beams is proportional to the thickness (z) of the specimen. The change in amplitude ($d\phi_i$) in relation to a change in thickness (dz) can hence be expressed for the two beams as

$$d\phi_{\boldsymbol{g_1}} = \left\{ \frac{\pi i}{\xi_{\boldsymbol{g_1}}} \phi_{\mathbf{0}} e^{2\pi i (\boldsymbol{\chi_0} - \boldsymbol{\chi_D}) \cdot \boldsymbol{r}} + \frac{\pi i}{\xi_{\mathbf{0}}} \phi_{\boldsymbol{g_1}} \right\} dz, \tag{2.44}$$

$$d\phi_{\mathbf{0}} = \left\{ \frac{\pi i}{\xi_{\mathbf{0}}} \phi_{\mathbf{0}} + \frac{\pi i}{\xi_{\boldsymbol{g_1}}} \phi_{\boldsymbol{g_1}} e^{2\pi i (\boldsymbol{\chi_D} - \boldsymbol{\chi_0}) \cdot \boldsymbol{r}} \right\} dz. \tag{2.45}$$

Realising the following chain of equality relations

$$(\boldsymbol{\chi_0} - \boldsymbol{\chi_D}) = (\boldsymbol{k_0} - \boldsymbol{k_D}) = \boldsymbol{g} + \boldsymbol{s}, \tag{2.46}$$

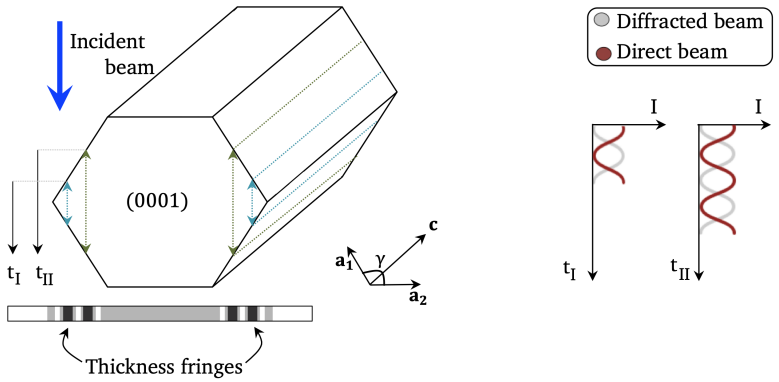

Figure 2.26: Illustration of the origin of thickness fringes for a NW on zone axis $[01\bar{1}0]$ in BF TEM. The intensity (I) of the diffracted and direct beam is plotted along the thickness at two positions where the beams are 180 degrees out of phase (t_I and t_{II}). The symmetric variation in thickness across the basal plane results in a symmetric fringe pattern. Adapted from [58].

and assuming that both the excitation error from section 2.3.2 ($\boldsymbol{s}$) and $\boldsymbol{r}$ are parallel to the electron beam, we end up with a pair of coupled differential equations, called the Howie-Whelan equations, after rearrangement. When solved, the intensity of the diffracted beam, $\phi_{\boldsymbol{g_1}}$, can be expressed as

$$I_{\boldsymbol{g_1}} = |\phi_{\boldsymbol{g_1}}|^2 = \left(\frac{\pi t}{\xi_{\boldsymbol{g_1}}}\right)^2 \frac{\sin^2(\pi t s_{\text{eff}})}{(\pi t s_{\text{eff}})^2} = 1 - I_0, \tag{2.47}$$

where t is now the thickness and s_{eff} is the effective excitation error given by

$$s_{\text{eff}} = \sqrt{s^2 + \frac{1}{\xi_{\boldsymbol{g_1}}^2}}. \tag{2.48}$$

Equation 2.48 is part of the dynamical description for diffraction. In the kinematic case s is used. Bending contrast occurs when the orientation of diffracting planes change such that the Bragg condition is fulfilled only at certain positions. This can be seen from Equation 2.47 when t is constant and s_{eff} varies. Thickness fringes appear when s_{eff} is constant and t varies, as illustrated in Figure 2.26 [58].

When a WZ NW is oriented on the $[1\bar{2}10]$ zone axis, thickness fringes are not detected. However, when the NW is rotated 30 degrees about the c-axis onto the $[01\bar{1}0]$ zone sinusoidal variations are seen. A schematic of the two different orientations can be seen in Figure 2.27 and TEM, STEM and diffraction patterns from the two orientations are presented in Figure 2.28. The BF TEM intensity profile across the semi-polar plane and the HAADF STEM intensity perpendicular to the c-axis is given in Figure 2.29.

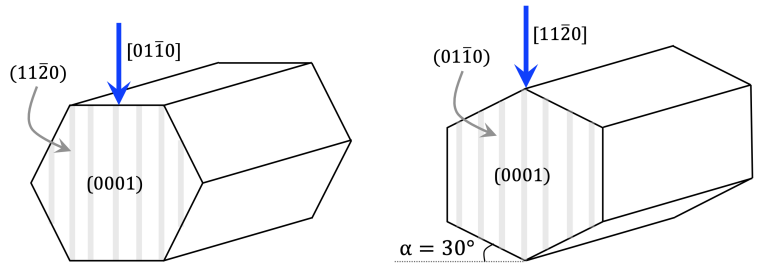

Figure 2.27: Two different orientations of a WZ NW. For inspection with TEM the [01$\bar{1}$0]-orientation results in thickness fringes because the thickness gradually increases from zero to maximum thickness. For the [11$\bar{2}$0]-orientation there is an abrupt increase from zero to a certain thickness before it increases towards maximum thickness. Adapted from [61].

(a)

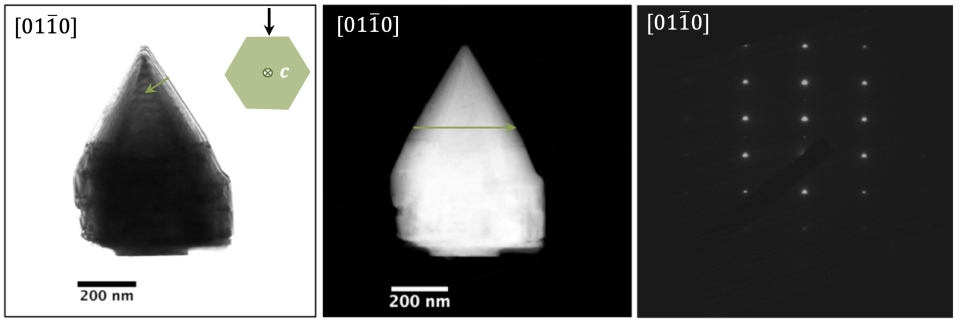

(b)

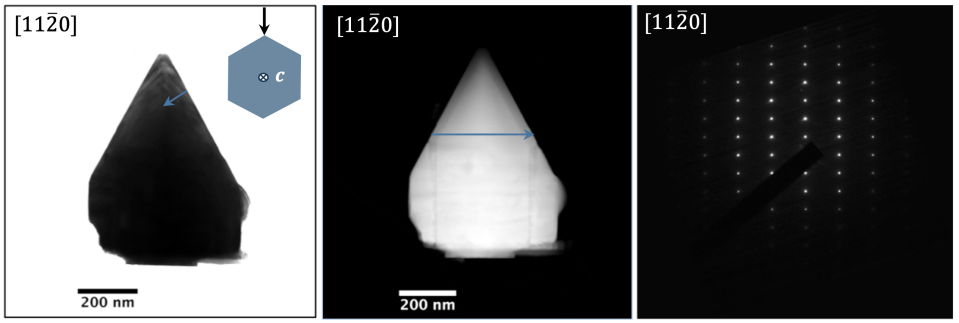

Figure 2.28: BF TEM, HAADF STEM and diffraction pattern from (a) zone [01$\bar{1}$0] and (b) zone [11$\bar{2}$0] of the same NW. The intensity profiles from the indicated arrows are given in Figure 2.29.

Phase contrast

Phase contrast imaging is exploited in order to record high-resolution TEM (HRTEM) images and takes advantage of the phase difference between different electron waves. This is the technique within conventional TEM with highest resolution. Whenever there is more than one beam contributing to an image, phase

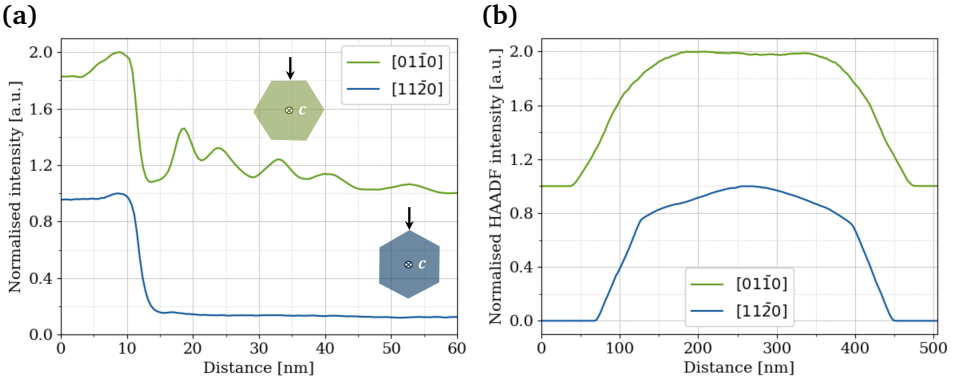

Figure 2.29: (a) TEM intensity profiles across the semi-polar planes and (b) HAADF STEM intensity profiles across the c-axis, indicated in Figure 2.28 for $[01\bar{1}0]$ and $[11\bar{2}0]$. For $[01\bar{1}0]$ thickness fringes are seen. The profiles across the c-axis show the gradual and abrupt change in thickness for $[01\bar{1}0]$ and $[11\bar{2}0]$, respectively. Diffraction contrast dominates for $[01\bar{1}0]$, while mass-thickness contrast dominates in $[11\bar{2}0]$.

contrast is present and in general the more beams collected the higher resolution. This is opposite to BF and DF TEM, where one or a small number of beams are collected to form diffraction contrast. Therefore, a larger objective aperture is used for phase contrast. Phase contrast is, for example, seen in thickness fringes, which is a result of interference between the direct beam and diffracted beams. In general, this contrast mechanism is recognised by fringes. Atomic resolution is possible because this contrast mechanism is extremely sensitive to thickness, orientation, scattering factor and focus and astigmatism of the instrument. An example of HRTEM from AlGaN NWs is given in Figure 2.30. Because there are so many factors affecting phase contrast formation, direct interpretation of atomic planes should be carried out carefully.

Another type of phase contrast occurs when two sets of repeating patterns overlap and the difference in periodicity is small. This results in a so-called Moiré pattern and the interference causing the pattern can be either translational, rotational or a combination of both. An example of Moiré fringes as a result of overlapping grains of different orientation is given in Figure 2.31. By taking advantage of such patterns, information about the crystal structure can be extracted, despite not having the resolution to resolve the individual lattices. This is done by inspecting the deviation in diffraction vectors

$$\Delta \boldsymbol{g_{tm}} = \boldsymbol{g_2} - \boldsymbol{g_1} \qquad \Delta \boldsymbol{g_{rm}} = 2\boldsymbol{g_1} \sin\left(\frac{\beta}{2}\right), \tag{2.49}$$

given for translational and rotational Moiré, respectively. Here, $\boldsymbol{g_i}$ represents the vector from the 000 reflection to the diffraction spot from lattice i and β is the angle of rotation. The magnitude of these vectors is found using Equation 2.21. Edge dislocations , for example, can be manifested by discontinuities in Moiré fringes.

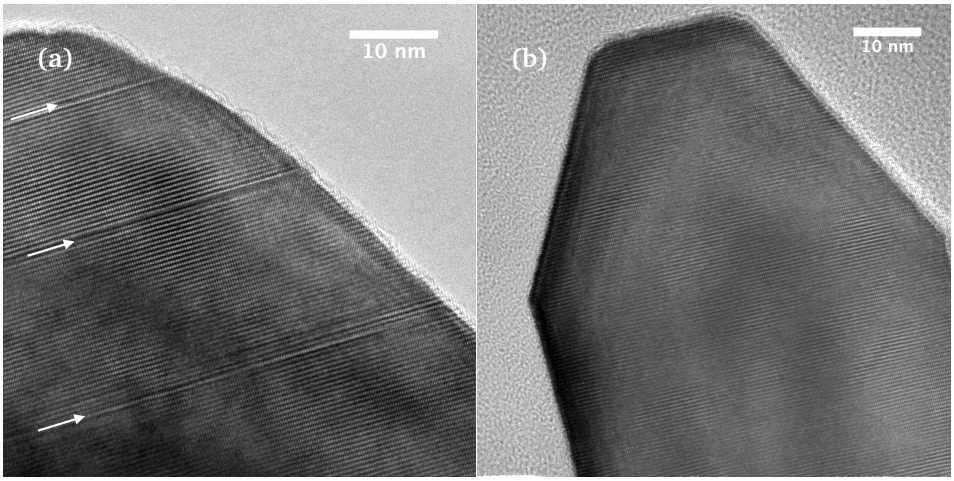

Figure 2.30: HRTEM images from AlGaN NWs with WZ crystal structure on zone [11$\bar{2}$0]. (a) Some NWs develop basal plane stacking faults (BSFs) at the tip of the NW. The NW in (b), on the other hand, exhibits higher crystal quality.

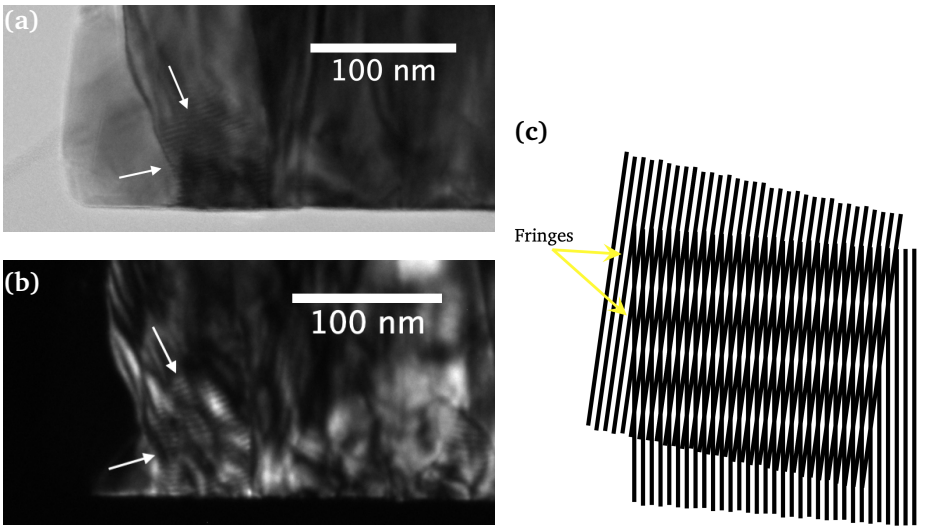

Figure 2.31: Moiré fringes from TEM inspection using (a) BF mode and (b) DF mode from the bottom of a NW. (c) The interference pattern is a result of the difference in orientation between two or more grains.

Kikuchi lines

Kikuchi lines are results of inelastic interactions followed by coherent elastic scattering events and can be seen in diffraction mode. Hence, the electrons contributing to this pattern have been transmitted through the specimen with multiple scattering events. These incoherent electrons can be exploited in order

to orient a crystalline specimen onto a desired zone axis, as the Kikuchi lines are fixed to the crystal. Kikuchi lines can also be used to determine the excitation error (s). A kikuchi pattern from zone axis $[01\bar{1}0]$ in GaN is simulated in Figure

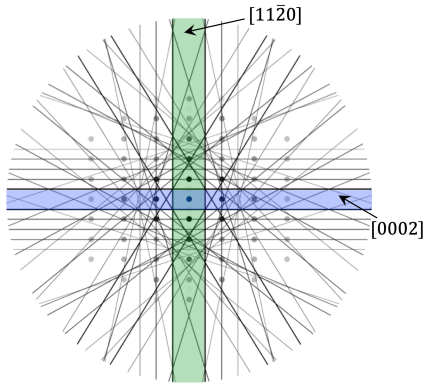

Figure 2.32: Kikuchi pattern from zone axis $[01\bar{1}0]$ in GaN simulated with JEMS. The corresponding diffraction spots can be seen in the background. Each symmetric pair of lines represents the span of the corresponding Kikuchi band, as illustrated in Figure 2.33. The [0002]-band and the [11$\bar{2}$0]-band are indicated.

2.32. Each zone is marked as a defined intersection between different bands and the bands from $[11\bar{2}0]$ and $[0002]$ have been indicated. Formation of Kikuchi bands through diffuse scattering for two different orientations of a crystal is illustrated in Figure 2.33. The edges on either side of one Kikuchi band represent lines from $\pm\boldsymbol{g_i}((hkl)$ and $(\bar{h}\bar{k}\bar{l}))$ and the projection of the diffracting plane can be found in between these two lines, separated according to Bragg's law.

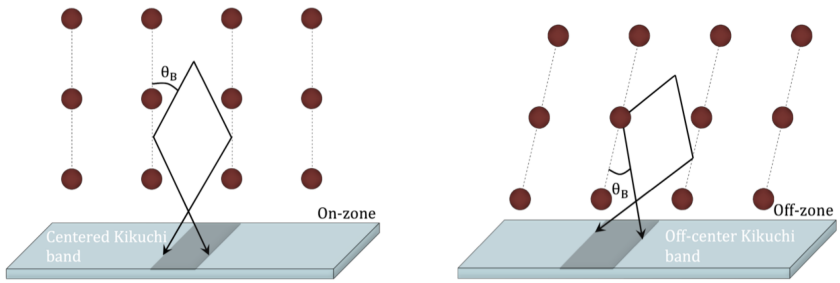

Figure 2.33: Illustration of the origin of Kikuchi lines. If the Kikuchi map is known it is possible to orient the crystal onto specific zone axes, as the Kikuchi lines are fixed to the crystal. Adapted from [58, 64].

2.4.4 Energy-dispersive X-ray spectroscopy

EDS is common supplementary equipment for electron microscopes. From Figure 2.23 it can be seen that characteristic X-rays are emitted from the TEM specimen when radiated by an electron beam. The origin of the X-rays can be explained by transitions between the electronic levels of the specimen material, as illustrated in Figure 2.34(a). Because the electrons in an atom have sharply defined energy levels depending on the element, different elements can be recognised based on characteristic transitions between these energy levels. The radiation process is described in three steps; ionisation, relaxation and finally, emission. When the electron beam hits the specimen, electrons are excited into higher states (ionisation). After a while the empty states are filled up by electrons from higher states (relaxation). By de-exciting to a lower state they emit characteristic radiation with wavelength corresponding to the specific energy transition (emission) [65, 58].

Moseley's law describes how the frequency of X-rays are related to the atomic number [66, 58]

$$\sqrt{\nu} = k_1(Z - k_2), \tag{2.50}$$

where k_1 and k_2 depend on the specific transition. Energy is proportional to ν and hence increases with Z. By exploiting X-rays in TEM the microscope can also perform analytical measurements.

After being excited by the electron beam, a fraction of the travelling X-rays gets absorbed inside the material. Hence, the detectable signal is hampered and this effect depends on the energy of the X-ray and the surrounding material. The final signal intensity arriving at the detector can be estimated by [65]

$$I = I_0 e^{-\mu l}, \tag{2.51}$$

where I_0 is the initial intensity, μ is the absorption coefficient of the absorbing material and l is the length travelled by the X-ray inside the absorbing material. μ is found to increase for lower energy X-rays from, for example, light materials like nitrogen [65]. This effect is illustrated in Figure 2.34(b).

EDS data can be quantified by the Cliff-Lorimer method, which is valid for sufficiently thin samples [58]. The continuous background emission shown in Figure 2.34(b) is removed before quantifying the signal. The method uses the following equation for a binary material

$$\frac{C_\mathrm{A}}{C_\mathrm{B}} = k_\mathrm{AB}\frac{I_\mathrm{A}}{I_\mathrm{B}}, \tag{2.52}$$

where the ratio of the concentration of two elements are proportional to the ratio of the intensities of the peaks in the EDS spectrum. The proportionality factor (k_AB) is determined from, amongst other, ionisation cross sections and fluorescent yields and vary for different microscopes and settings.

The EDS system consists of an X-ray detector, processing electronics and software. The detector generates voltage pulses proportional to the X-ray energy,

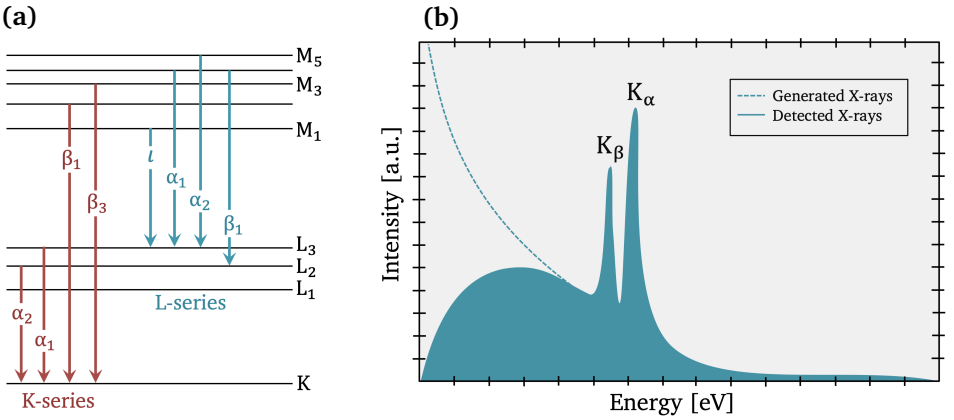

Figure 2.34: (a) Electronic transitions in an atom with the Siegbahn notation. (b) X-ray radiation with characteristic peaks superimposed on the continuous background emission (Bremsstrahlung). Not all of the generated radiation is picked up in the resulting spectrum because the lowest energy radiation is either absorbed by the sample or in the detector. Adapted from [65, 61].

which is processed into a spectrum with counts versus energy in one dimension. Because of the geometry of the set-up, the sample has to be tilted towards the detector to increase the signal yield [58]. This is illustrated in Figure 2.35. When

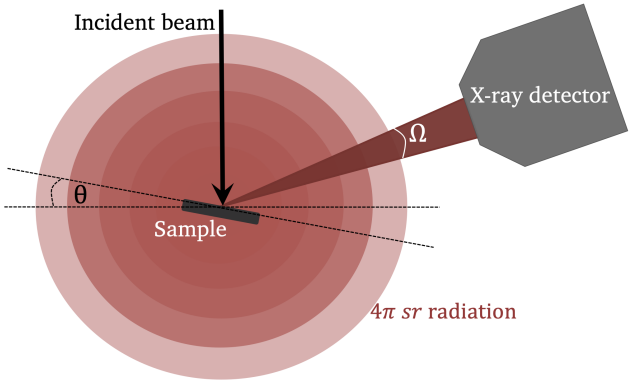

Figure 2.35: Illustration of X-ray detection inside a TEM where the sample emits radiation at a solid angle of 4π sr. The sample has been tilted θ degrees towards the detector in order to increase the signal yield within the collection angle (Ω) of the detector. Adapted from [58, 65, 61].

the sample is struck by the electron beam it emits radiation at a solid angle of 4π sr [65]. However, some of this radiation is absorbed in the specimen and only a fraction ends up within the collection angle (Ω) of the X-ray detector [58]. The efficiency of EDS is therefore poor, resulting in relatively low signal-to-

noise ratio (S/N). Counting statistics often limits quantification and extending the counting duration only reduces the spatial resolution due to drift, beam damage, contamination, etc. The same problems are encountered for other electron spectroscopy techniques like CL, discussed in section 2.7. EDS data is hyperspectral and different data processing routines are discussed in section 2.8.

2.5 Scanning electron microscopy

The principles of the SEM are in many aspects comparable to the TEM, the main differences being what type of electron signal is detected (discussed in section 2.4.2), the acceleration voltage of the electron beam and how sampling is performed. A TEM predominantly exploits the transmitted electrons while a SEM, on the contrary, makes use of the BSEs and SEs. This requires the accelerating voltage in TEM to be of greater magnitude (100-300 kV compared to 1-30 kV for SEM). On this account, the SEM provides to a larger extent information about the sample surface and composition. The sampling in SEM is conducted by coils scanning the beam over the sample in a raster-scan manner. Pixel-by-pixel data acquisition followed by reconstruction results in the final image. TEM, on the other hand, uses a static beam [65, 58]. Combined, the differences between SEM and TEM make up a factor of about 10 in resolution in favour of TEM [67]. The benefits of SEM are larger size of inspected area and fewer restrictions on sample preparation. In conclusion, SEM and TEM provide slightly different information about a sample and should be used complementary to each other.

2.5.1 Principles of the SEM

A SEM column is depicted in Figure 2.36 where the various components exploited for image formation is illustrated. Like in a TEM, an electron gun forms the initial beam that is subsequently extracted towards the following lenses with the help of an anode. TEM differs from SEM as scanning coils are inserted for the latter, directing the beam away from the optical axis before hitting the sample. A donut-shaped BSE detector is commonly placed symmetric above the sample, while the SE detector is biased to one side of the column. The coils raster scan the sample and a map consisting of the intensity at each (x,y) location is put together on the viewing screen [65, 67].

In this work a SEM equipped with a SE detector is exploited. SEs have lower energy than BSEs (see Figure 2.37(b)) and can therefore only escape from the volume closest to the specimen surface [65]. The interaction volume for different signals in the SEM is illustrated in Figure 2.37(a). Contrast formed by SEs is characterised by shadowing due to the spatial bias from the SE detector. This was illustrated in Figure 2.36. From this contrast mechanism it is, for example, possible to extract specimen topography, which makes the orientation of the specimen during acquisition important. Another type of contrast mechanism is related to the atomic number and the work function[3] of the material, as elements with high

[3]The work function of a material is the difference in potential energy for an electron between the

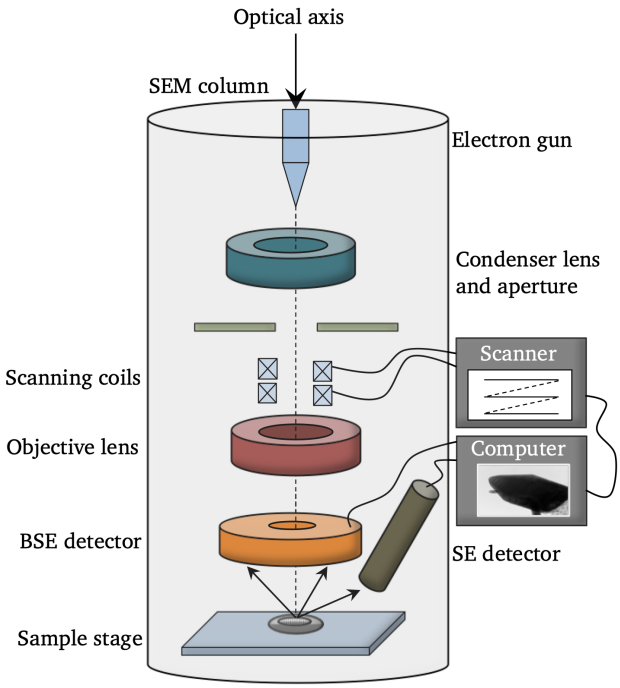

Figure 2.36: Schematic of a SEM showing the main constituents along the electron column. The coils raster scan the sample and save the detected signal from each position in a (x,y)-map on the computer. Adapted from [63, 65].

atomic number have higher SE yield on a flat sample [65]. Therefore, Ga appears brighter than Al, for example, in a SE SEM image. SE yield also depends on specimen tilt, that is, the incident angle of the electron beam, and accelerating voltage. The SE yield is found to increase with increasing tilt and decreasing acceleration voltage [65].

2.6 Scanning transmission electron microscopy

The STEM combines different features from the two earlier discussed and today well-established microscopy techniques, SEM and TEM. Like in TEM electrons are transmitted through an electron transparent specimen. However, in a STEM the beam is initially formed into a small probe (convergent beam) with a radius in Angstrom range. As opposed to the static parallel beam used for conventional TEM this convergent STEM beam is raster-scanned across the specimen with a double deflection system, like in a SEM [69].

BF STEM has similar contrast as BF TEM, but due to the added scan noise in STEM it provides no advantages. High-angle annular dark-field (HAADF) STEM,

Fermi level and the vacuum level [17]. This is the energy it takes to remove the electron from the core.

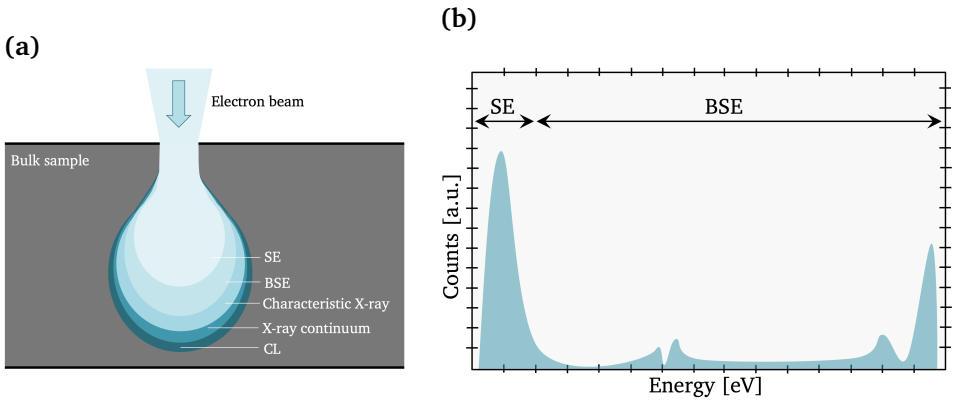

Figure 2.37: (a) Interaction volume for a SEM sample during inspection. The volume is dependent on accelerating voltage, average atomic number and incident angle of the electron beam. (b) Graph showing the approximate energy distribution of SEs and BSEs. Adapted from [68].

on the other hand, can give complementary information by exploiting electrons that have undergone interaction, like diffraction and Rutherford scattering, in image formation [70]. By taking advantage of electrons scattered above a certain angle with a HAADF detector it is possible to achieve sensitive Z-contrast imaging, one of the big merits of the STEM. The scanning feature also makes STEM suitable for spectroscopic mapping, like EDS-mapping.

A crucial aspect when it comes to resolution in STEM is the size of the probe. This size is determined by the lenses and is therefore limited by aberrations ($\sim$2 nm for uncorrected microscopes). Presently there exist both dedicated STEMs in addition to TEMs with available STEM operation [69, 62]. The latter will be used in this work and a schematic of the principles of STEM operation is given in Figure 2.38.

2.6.1 Principles of the STEM

Inside the vacuum column in a conventional TEM, scan coils, particular detectors and necessary circuitry are connected to provide STEM operation [69]. The main objective of the initial condenser lenses during STEM operation is to form the electron beam into a small probe, which is critical for the resolving ability of the microscope. This probe is raster-scanned across the region of interest on the specimen surface and the detected signal is combined with the probe position to produce an image. If spectroscopic acquisition is performed in STEM mode, this is detected simultaneously. This is illustrated in Figure 2.38. The magnification of the resulting image is determined by the size of the scanned area [62]. Given a fixed detector size, the scattering angle determining the STEM mode is controlled

by the camera length, that is, the intermediate lenses.

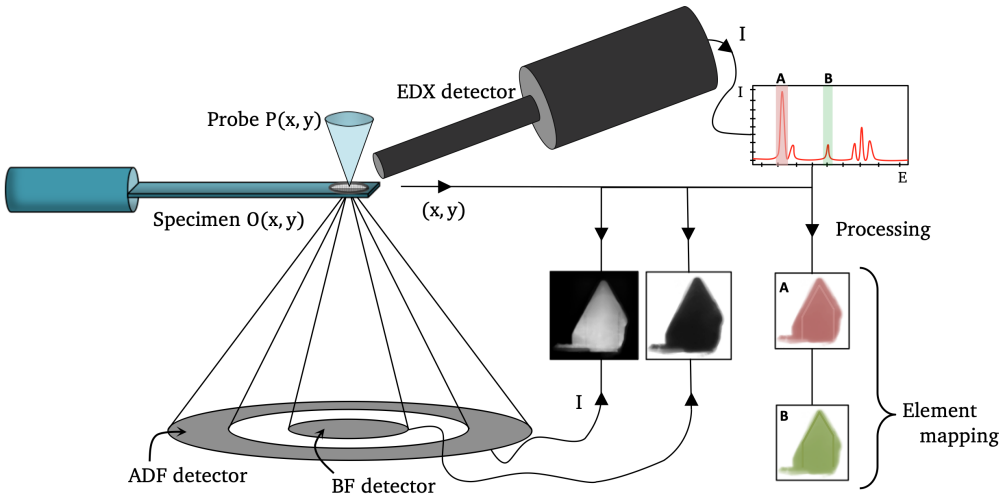

Figure 2.38: Hyperspectral image formation in STEM mode where the intensity detected for both electrons (BF STEM and HAADF STEM) and X-rays (EDS) are coupled to the probe location on the sample. By integrating the X-ray energy over a certain range, element mapping can be performed, illustrated for element **A** and **B**. Adapted from [62].

The signals that can be exploited in STEM are transmitted electrons scattered at a relative low angle (BF mode), transmitted electrons scattered at a relative high angle (ADF mode), transmitted electrons loosing significant amounts of energy (electron energy loss spectroscopy (EELS)) and X-rays generated in the specimen (EDS) per probe position (x,y) [69].

2.6.2 HAADF STEM

HAADF STEM is the name of the STEM mode taking advantage of incoherent quasi-elastically scattered electrons [70] with relative high scattering angles. Compared to coherent diffraction and phase contrast, Z-contrast from HAADF STEM images is easier to interpret. The electron scattering is approximated in analogy with Rutherford scattering from an unscreened nucleus [71], which was described in Equation 2.40. For HAADF STEM the intensity is integrated over the ADF detector and this value is approximately related to the atomic number Z by [72]

$$I \propto Z^{1.7}. \tag{2.53}$$

This equation stems from the Rutherford formula in Equation 2.40, where the exponent is lowered due to screening of the Coulomb potential and complex channelling effects [70]. Hence, elements with higher atomic number normally result in more intensity and appear brighter in the HAADF STEM image. One of the

merits of HAADF STEM is high chemical sensitivity providing Z-contrast imaging for materials with small alterations in elemental composition.

2.7 Cathodoluminescence

Recently the interest in and value of CL has risen within the semiconductor industry, partly due to the current exploration of III-nitride NWs for optoelectronic devices. CL occurs when electrons are accelerated onto a material, resulting in emission of low energy photons (1 eV to 5 eV [65]). This spectroscopy technique is made use of for inspection of optoelectronic properties of semiconductors, like bandgap energy, as the electronic transitions can be measured. Features like lattice vacancies and other defects can also provide energy transitions responsible for radiative recombination and hence be inspected. Other application areas include detection of local efficiencies in optoelectronic devices or determination of doping levels [65, 73]. Similar to EDS, discussed in section 2.4.4, CL is a hyperspectral imaging technique when used in scanning mode. It is therefore possible to construct two-dimensional images based on the wavelength of the emitted electromagnetic radiation. The perk of using accelerated electrons as excitation source in CL, compared to a photon beam in photoluminescence (PL) or current in electroluminescence (EL), is that the probe diameter can be made sufficiently small in order to spatially resolve small features in the NWs. PL is limited by the Rayleigh criteria, discussed for electron microscopy in section 2.4, given by [58]

$$x = 0.61\frac{\lambda}{\mathrm{NA}}. \tag{2.54}$$

Here, λ is the wavelength of the photon beam and NA is the numerical aperture. EL is a macroscopic technique also limited according to the Rayleigh criteria, with the ability to resolve features in the μm-range depending on the detection system [74, 75]. CL exhibits a spatial resolution down to approximately 10 nm and a spectral resolution of $<$1 nm [76]. One of the reasons for the inferior resolving ability compared to SEM is that electron-hole pairs not necessarily recombine at the same location as where they are generated. This is due to the fact that charge carriers are mobile and can move within the sample through drift or diffusion. Hence, the diffusion length of charge carriers is an important factor reducing the spatial resolution of CL [77]. This is discussed further in section 2.7.2. STEM-CL applies STEM instead of SEM as the excitation source and provides superior spatial resolution due to more local excitation, but is also limited by charge carrier diffusion [78].

2.7.1 Working principles of CL

CL can rather easily be integrated in a SEM, by connecting the required detectors similar to an EDS detection system. It is also possible to implement CL in other electron-exciting environments [79]. A schematic of a CL-setup inside a SEM is shown in Figure 2.39. The measurement technique applied for photon detection is

simply an elliptical mirror inserted above the sample stage, followed by fiber optics leading to a spectrograph and finally, a camera [65]. The spectrograph has an adjustable diffraction grating, which determines the dispersion of the wavelengths onto the camera and hence the spectral resolution. There are some drawbacks with the geometry of this set-up. The insertion of the mirror makes the working distance (the distance from the bottom of the SEM column to the top of the sample) longer and hence the depth of focus shorter, which deteriorates the performance of the microscope. The mirror also restricts the tilting of the sample. The optimum acquisition parameters for CL are low electron energy and low beam current, to achieve a small interaction volume and a small probe size. However, these two conditions are contradictory. The detection time per pixel should also be short enough to minimise drift, but long enough to have high S/N [80]. Because of these restrictions it is important to apply parameters according to the properties of the specimen to be inspected. The resulting wavelength-resolved spectra are

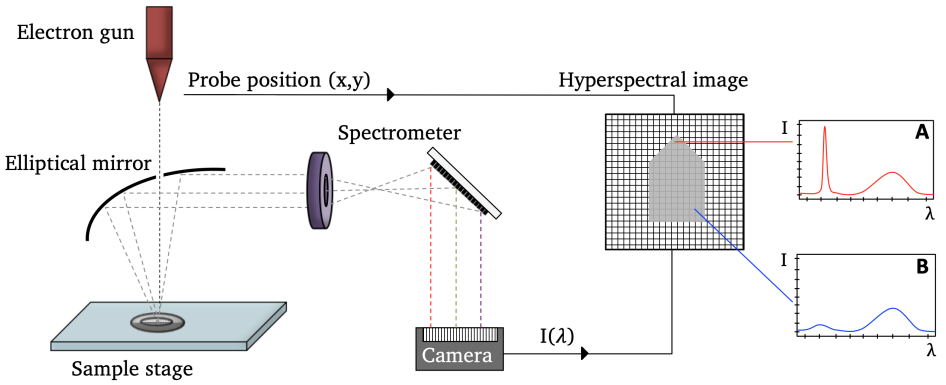

Figure 2.39: Schematic showing the principles of a CL detector inside a SEM. The elliptical mirror reflects the electromagnetic radiation emitted from the sample into a spectrometer. This results in intensity versus wavelength spectra for every (x,y) location. Spectra from two pixels (**A** and **B**) are illustrated. Lenses, apertures, electron detectors and scanning coils are omitted from the SEM column.

connected with the corresponding SEM image, such that spectral information for every (x,y) location on the specimen can be extracted [81].

During acquisition the electron beam excites electrons in the specimen from the valence band to the conduction band, as illustrated in Figure 2.40. The electron can take several paths, depending on the available energy transitions in the material. Direct recombination in the valence band is one possibility, or the electron can recombine with a hole in a trap level, caused by irregularities in the crystal structure. A third possibility is Auger recombination, as mentioned in section 2.1.5 [41]. These three recombination mechanisms were illustrated in Figure 2.10. If the material has been doped or implemented with, for example, quantum-confined structures, different extrinsic states exist in the region between the valence band and the conduction band. These states contribute to new energy

transition possibilities.

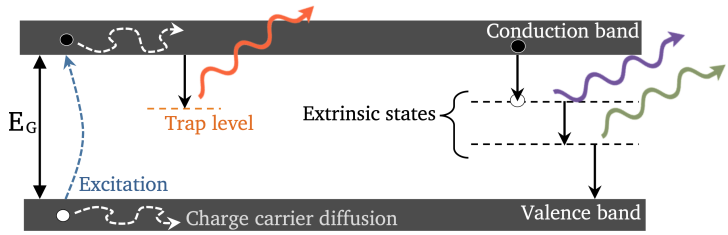

Figure 2.40: Illustration of the different energy transitions possible during CL detection. Due to charge carrier diffusion electrons exited in one area of the sample do not necessarily recombine in the same area. Adapted from [65, 31].

2.7.2 Signal delocalisation by diffusion

The CL signal emerges from a relative large volume, as seen in Figure 2.37(a). Charge carrier diffusion makes excited carriers recombine away from this excitation area, degrading the spatial resolution of CL even further. Transport by diffusion occurs when there is a concentration gradient of a species of mobile particles present in a solid, from regions of high concentration to regions of low concentration. The driving force behind this behaviour is random motion increasing the entropy, and hence minimising the free energy, of the system. Like any other transport mechanism inside a solid, diffusion suffers from random collisions. This process is best described by the mean free path, l (the distance travelled in between collisions), and the mean collision time, τ (the time between collisions). These two parameters describe the scattering inside the solid. The net flux of particles within a solid with concentration gradient $\left(\frac{\partial c}{\partial x}\right)$ is given by Fick's first law of diffusion [82]

$$\phi(x,t) = -D\frac{\partial c(x,t)}{\partial x}, \tag{2.55}$$

where D is the diffusion constant of the solid in units of m^2/s, depending on the scattering rate (l and τ). For a charge carrier inside a semiconductor, the diffusion length is defined as the distance travelled before the carrier recombines and is approximated by [79]

$$L_D = \sqrt{D\tau}. \tag{2.56}$$

The density profile of a charge carrier point source at $x = 0$ undergoing diffusion can be approximated as [24]

$$n(x) \propto \exp -\frac{x}{4D\tau}. \tag{2.57}$$

This is a simplified picture and recombination is not accounted for. The standard deviation of this distribution is approximately $\Delta x = \sqrt{D\tau} = L_D$. Hence, the spatial resolution of CL data is limited according to the diffusion constants of the different diffusion mechanisms of the charge carriers.

2.7.3 CL spectrum interpretation

The peak positions and intensities in a CL spectrum inform about the different bandgap energies available in the material and the amount of radiation coming from the different bandgaps. For $Al_xGa_{1-x}N$, the peak position depends on the Al/Ga ratio, according to Equation 2.1 and Equation 2.9. Intrinsic peaks stem from, for example, vacancies in the crystal structure or other irregularities. Extrinsic peaks, on the other hand, originate from impurities [83]. Another source for extrinsic peaks is confined carriers by engineered structures like MQWs. The full width at half maximum (FWHM) of each peak is affected by the quality of the crystal, bandgap fluctuations (e.g. from doping), electron-phonon coupling, strain, temperature etc. [84].

For CL there exists no law corresponding to Moseley's law for EDS (section 2.4.4) that dictates the wavelength emitted from an element as a function of atomic number. The wavelength is given by the bandgap, which is a property of the entire compound and not each individual element, as in EDS. Additionally, there are non-radiative processes not accounted for and absorption as in EDS, which makes it challenging to interpret CL spectra [79]. Because CL spectra often consist of several overlapping peaks, a common technique to determine the properties of each peak is Gaussian deconvolution in eV units [81, 85]. An example of a deconvoluted spectrum is shown in Figure 2.41.

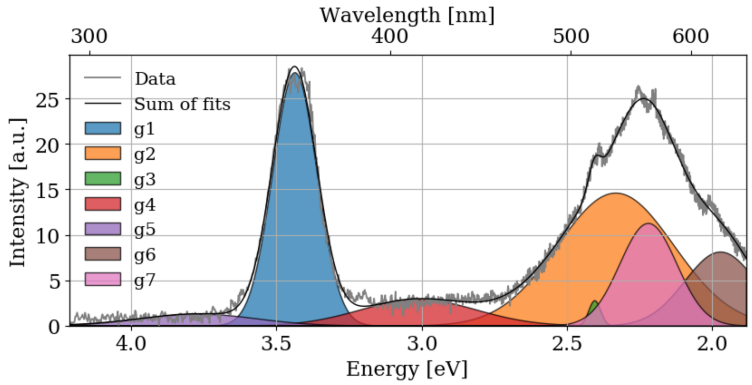

Figure 2.41: Example of a rough Gaussian decomposition performed on CL data from AlGaN NWs. Here, seven components have been included in the fit. Original data and the sum of the components can also be seen.

2.8 Principles and analysis of hyperspectral data

CL and EDS acquired by spatial scanning results in hyperspectral data. That is, both spatial and spectral information is acquired by collecting a spectrum for every single pixel. Energy-filtered images, i.e. elemental maps, can be constructed from hyperspectral data by choosing an energy range and only including the integrated intensity from that range for every pixel [81]. This way the part of a structure with a certain element responsible for characteristic X-rays (or the part of a light-emitting structure responsible for emission of a certain wavelength) can

be recognised in the image. An illustration of the concept of hyperspectral imaging is given in Figure 2.42 and the construction of energy-filtered images is illustrated for 2 x 2 pixels in Figure 2.43. If the S/N from the individual pixels is too low, it is possible to combine several pixels by binning the hyperspectral dataset. However, this hampers the spatial resolution. The problem with low S/N can be accounted for by statistical methods like Principal Component Analysis (PCA) [86]. In what follows, three different techniques for denoising and analysis of hyperspectral data will be presented.

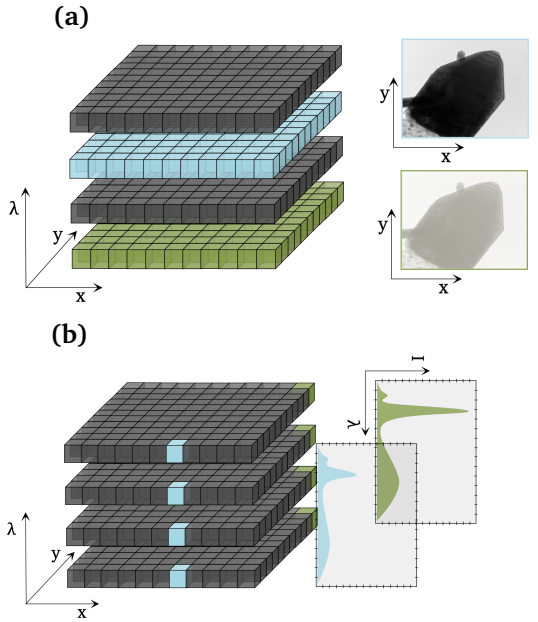

Figure 2.42: Illustration of hyperspectral CL data. (a) A horizontal slice represents the data reconstructed with one specific wavelength or a range of wavelengths. (b) A vertical slice represents the spectrum from a single pixel.

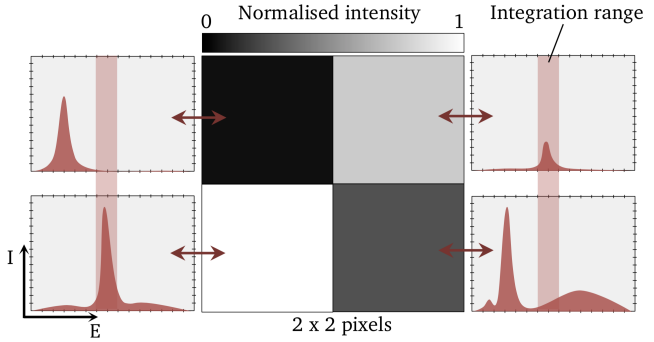

Figure 2.43: Illustration showing an image consisting of 2 x 2 pixels generated from the intensity integrated in a certain energy range for every pixel. This principle is used to construct EDS elemental maps and CL images.

Principle Component Analysis

PCA is a useful method for noise reduction in hyperspectral imaging, which is done by fitting a low-dimensional subspace to data in high-dimensional space. In order to determine the dimension of the data after noise reduction, singular value decomposition (SVD) is often applied. In PCA transformation variance in the data is exploited and the dimension of the data is reduced by removing redundant (i.e. noise) and correlated data. The components with higher variance, that is, the components with larger spread in the data, are chosen to represent the entire dataset, as illustrated in Figure 2.44. In the transformed data the principal components are put together in a weighted linear combination. The transformation is given by [87]

$$\mathbf{y} = \mathbf{A}^T\mathbf{x} \qquad \mathbf{y}, \mathbf{x} \in \mathbb{R}^l \qquad \mathbf{A} \in \mathbb{R}^{l \times l}, \tag{2.58}$$

where $\mathbf{y}$ is the transformed data containing the uncorrelated variables, $\mathbf{A}$ is the transformation matrix and l is the dimension. An example of PCA performed on both EDS and CL data is given in Figure 2.45 and Figure 2.46.

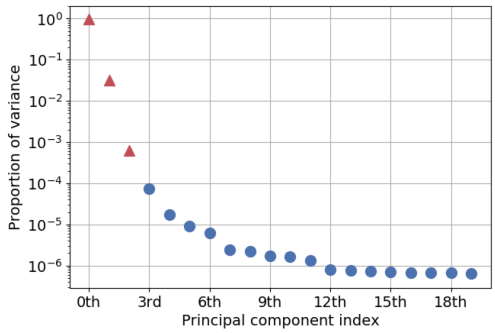

Figure 2.44: Example of a SVD scree plot used to approximate the dimension of the data in PCA and NMF. The red triangles indicate the high variance components included in the final data and the blue circles indicate the redundant components that are removed.

Non-negative matrix factorisation

NMF is an algorithm used for identifying different components in large data, described by the following optimisation problem

$$\min ||\mathbf{X} - \mathbf{MA}||_2^2 \qquad \mathbf{M}, \mathbf{A} \geq 0. \tag{2.59}$$

Here, $\mathbf{X}$ is the original data and $\mathbf{M}, \mathbf{A}$ represent the components and the corresponding weights. Compared to PCA, NMF ensures that the magnitude of the different components, for example the intensity in a CL spectrum, is positive and can represent physical entities. However, the algorithm can not know the dimension of $\mathbf{M}$ and $\mathbf{A}$. Therefore, similar to PCA, SVD is used for a rough approximation. If the data is decomposed into too many components, each component might not represent a physical feature [87].

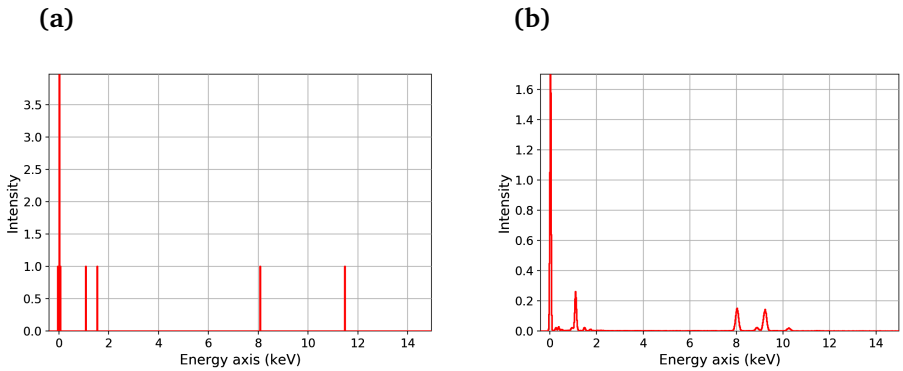

Figure 2.45: Illustration of (a) raw data from EDS and (b) the same data processed with PCA using the HyperSpy library in Python. It is important to underline that this figure illustrates only one of many spectra that are used for the PCA processing.

Mixed-Gaussian peak fitting

Mixed-Gaussian peak fitting is another method of extracting information from, for example, a CL spectrum. The CL signal from a single feature is assumed to take the shape of a Gaussian distribution in eV-space [85], due to statistical variations. By fitting a complex CL spectrum to a sum of Gaussians, it is possible to extract peak position, intensity and FWHM for the different features. However, this is not an accurate method as the separation into different components can be ambiguous. The findings should therefore be considered in conjunction with results from other methods. A deconvoluted CL spectrum was illustrated in Figure 2.41 [81]. The code used for Gaussian decomposition in this work is given in Appendix A.3.

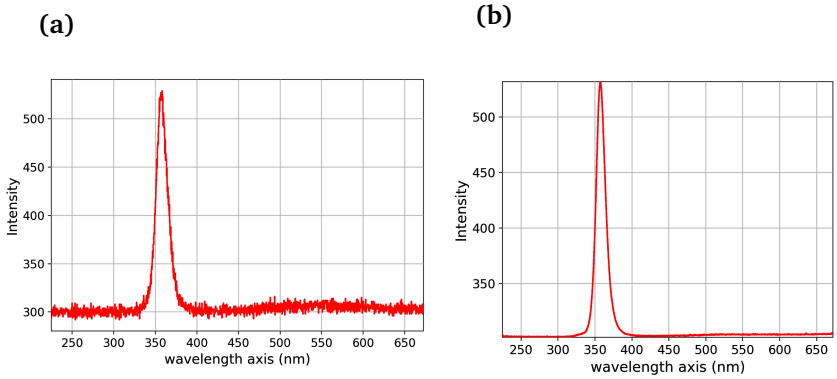

Figure 2.46: Illustration of (a) raw CL data and (b) the same data processed with PCA using the HyperSpy library in Python.

3 Experimental

3.1 Material

The studied NWs in this work are grown in a Propel GaN MOCVD and the targeted structure is illustrated in Figure 3.1. Initially a SiO_2 mask of 35 nm is grown on top of a SLG-covered sapphire substrate. The mask is patterned by EBL and the full pattern consists of sixteen (4 x 4) 500 x 500 μm^2 areas, all with hole patterns with different size and spacing illustrated in Figure 3.2. The 4 x 4 pattern is implemented in order to determine the optimal conditions for growth. Following is the MOCVD growth. The Al contents and growth lengths stated in what follows have not been confirmed and are based on the gas phase concentration, temperature and pressure during the intended growth and the duration of the different steps.

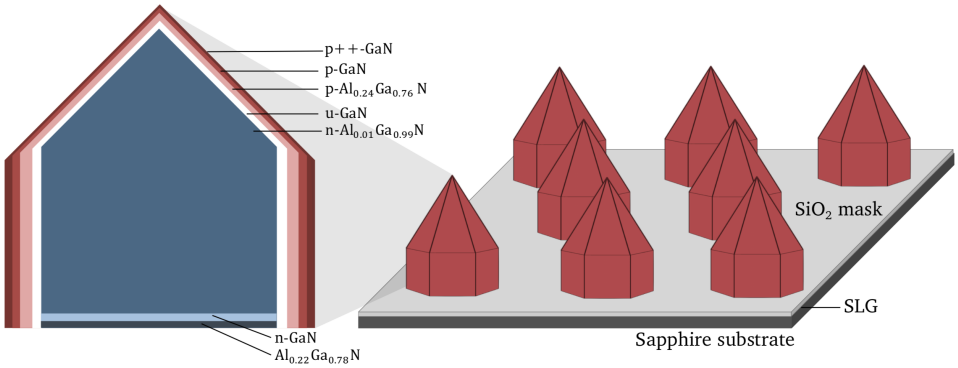

Figure 3.1: Cross section of targeted NW heterostructure and array of several NWs grown with mask on SLG-covered sapphire. The figure is not to scale in order to illustrate all features.

An AlGaN nucleation layer with 22% Al is initially grown on SLG on the c-plane of the sapphire substrate. Following is a layer of n-GaN and a 600 nm long n-doped AlGaN layer with 1% Al. A 50 nm undoped shell layer of GaN is subsequently grown, before a 20 nm long p-doped AlGaN shell layer with 24% Al is grown. Finally, two p-GaN shell layers (150 nm in total) of increasing doping level complete the LED as the contact layer opposite to the SLG layer.

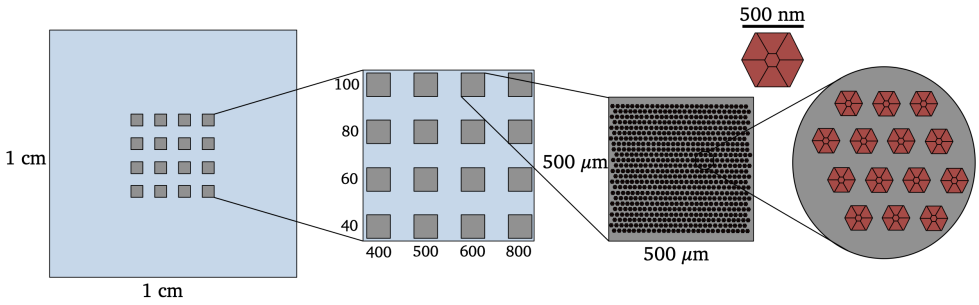

Figure 3.2: Schematic showing the 1 x 1 cm^2 sample supplied by CrayoNano. The horizontal and vertical numbers along the 4 x 4 square pattern give the spacing and dose, respectively, from the previous EBL step. The square with spacing 600 nm and dose 100 (denoted 100_600) was chosen and scribed for preparation onto TEM grid due to promising morphology. The red hexagonal structures ordered in a hexagonal pattern represent the NWs.

3.2 Sample preparation

The patterned 1 x 1 cm^2 sample provided by CrayoNano was initially scribed with a diamond scriber. One of the 4 x 4 squares on the patterned sample was chosen according to which one exhibited the most promising growth and minimal coalescence. The chosen area (denoted 100_600) is shown in Figure 3.2. A scriber wet with isopropanol was traced over the region of interest and washed off in a beaker of fresh isopropanol. This was repeated until the entire region was scraped. The capped beaker, in which the scriber was washed off in, was subsequently inserted in a ultrasonic bath for 5 minutes before a small amount was carefully transferred to two TEM finder grids with a pipette. The finder grids consist of Cu frames with enumerated references covered with a 20 nm thick carbon film from Electron Microscopy Sciences (EMS). The finalised grids were mounted in between pairs of Mo plates of diameter 15 mm, with concentric holes of diameter 2.5 mm, glued together with silver glue for easy handling during SEM/CL. An illustration of this can be seen in Figure 3.3. The grids are, subsequent to SEM and CL inspection, easily detached and ready for TEM inspection. Prior to TEM inspection plasma cleaning was performed if required. A shielded holder was used for a duration of 2×10 s in a Ar/O plasma.

3.3 Instrumentation

The AlGaN NWs in this work were studied with mainly three different electron microscopes. For SEM and CL studies a FEG Hitachi SU5000 equipped with Delmic SPARC CL detection system was applied. The latter has a spectral resolution of about 0.2 nm. An acceleration voltage of 5 kV was used together with a SE detector.

For TEM investigations a Jeol JEM 2100 LaB_6 and a Jeol JEM 2100F were exploited. A dual tilt beryllium holder was used in order to tilt the NWs onto

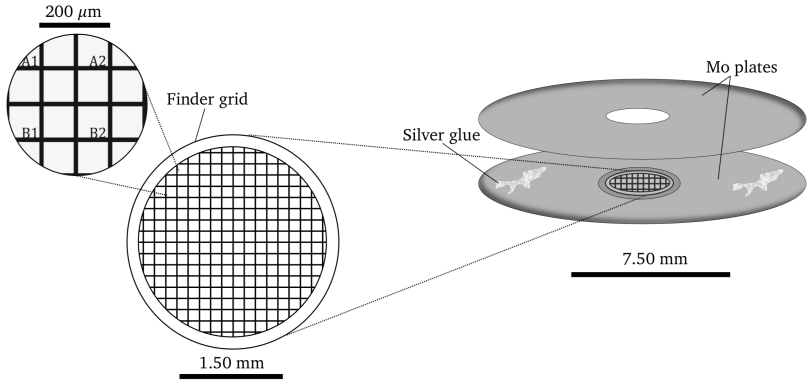

Figure 3.3: Homemade sample holder for SEM and CL inspection. The finder grid consists of a Cu frame covered with a carbon film and it has enumerated references (A1, A2, B1, B2 etc.). The grid is sealed in between two Mo plates with concentric holes using silver glue for easier handling.

specific zones. All characterisation by TEM was performed at 200 kV, recorded on a 2k Gatan Orius CCD (2100) and a Gatan 2k UltraScan CCD (2100F).

EDS measurements were executed in the Jeol JEM 2100F by an Oxford X-Max 80 SDD EDS. A spectral range of 0-20 keV was used in STEM mode for all EDS data.

3.4 Correlated data acquisition

The different techniques applied in this work are performed in a certain order. The reason for this is that the 200 kV electron beam incident on the NWs during TEM inspection degrades the CL signal [12, 59]. Initially the as-grown sample is inspected with SEM followed by scribing and sample preparation onto TEM grids. The sample is inspected with SEM also after grid preparation in order to examine the scribed area. The correlated data acquisition for a full series is then performed in the order indicated by the following sections for both grids. All measurements are performed at room temperature.

An initial SEM inspection is performed in order to localise the NWs on the two grids for more effective acquisition. The position of the different NWs on the grids is noted so that they easily can be retraced. SEM also provides a three-dimensional impression of the NWs where the morphology and the different facets of the NWs can be seen.

Subsequent to CL acquisition TEM images can be acquired. Kikuchi lines in the diffraction pattern of the individual NWs are initially used in order to reorient the NWs onto the desired zone. When the NWs finally are on the desired zone conventional TEM techniques are applied. If necessary, plasma cleaning is applied.

HAADF STEM is applied after conventional TEM with focus on distinguishing the different components of the radial heterostructure of the NWs.

The final technique applied in this correlated series is EDS as it results in

significant damage to the NWs and carbon contamination. Small regions of interest are chosen to minimise degradation of the NWs.

3.5 Data processing

Processing of images from SEM, TEM and STEM was performed in Digital Micrograph (version 3.30.2016.0). Intensity profiles were extracted from this software and exported to Jupyter Notebook written in Python (version 3.7.2).

EDS data was acquired in AZtec and exported as three files for spatial and spectral calibration. These files include a rpl-file, a txt-file (spatial calibration) and a msa-file (spectral calibration) which were subsequently converted into one hdf5-file (see Appendix B.1).

CL data was acquired in ODEMIS and exported as h5-files. ODEMIS viewer was used to inspect the h5-files. The spatial data was calibrated by exploiting SEM and TEM images of the same areas. For further processing the data was converted into hdf5-files [88] (see Appendix A.1).

For hyperspectral data acquired from EDS and CL the HyperSpy library in Python was applied after conversion to hdf5 format. In order to reduce noise in the data PCA was performed and NMF was applied for decomposition. Both utilities are found in the HyperSpy library together with basic operations such as binning, cropping etc. Plotting of all data was performed in Python through Jupyter Notebook.

4 Results

In this chapter the results from the five different characterisation techniques are presented. Firstly, general findings from before and after sample preparation are given. Finally, results from SEM, TEM, STEM, CL and EDS from six individual NWs and one cluster are presented for the correlated study.

4.1 General findings before and after sample preparation

SEM inspection of as-grown sample

The bird view SEM image in Figure 4.1(a) was acquired in order to investigate the morphology of growth area 100_600 (see Figure 3.2) before the preparation routine described in section 3.2 was conducted. Some NWs have coalesced and are parts

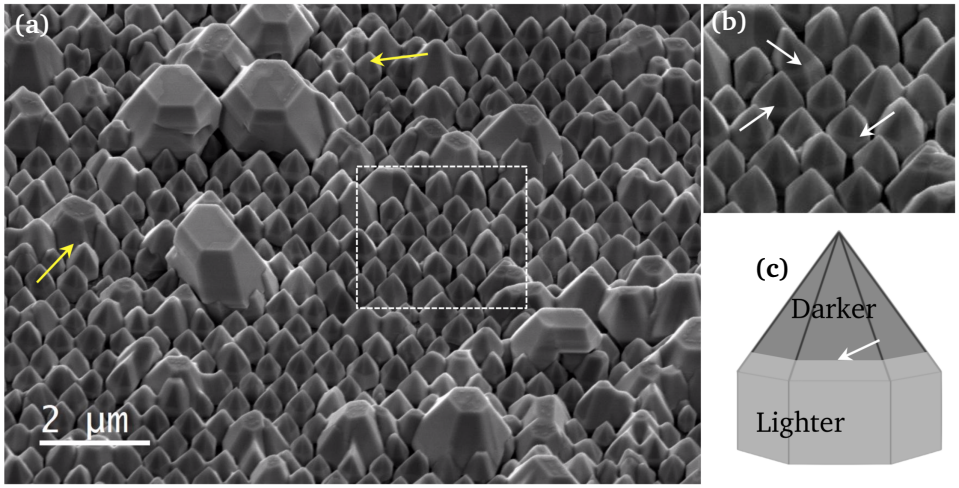

Figure 4.1: (a) Bird view secondary electron SEM image of the as-grown sample acquired by Julie Hessevik at CrayoNano. Yellow arrows indicate areas of coalescence. In (b) a more uniform growth area is shown, where a change of contrast has been indicated with white arrows. The same feature is illustrated in (c).

of larger agglomerates indicated by yellow arrows, while other NWs have grown separately. Light edge contrast is present at interfaces between facets. A change

of SE contrast can be seen in Figure 4.1(b), where the top of the NWs appears darker than the bottom. This is illustrated with a schematic in Figure 4.1(c). More specifically, the m-planes of the NWs appear brighter than the top of the semi-polar planes and the c-planes, independent of the shadowing caused by the spatial bias from the SE detector.

Selected-area growth

The majority of the NWs grow separately from their respective holes in the SiO_2 mask. This was seen in Figure 4.1(a). However, a significant percentage shows extensive radial growth, causing coalescence of several NWs. This can be seen for a cluster deposited onto a grid in Figure 4.2(a), where more than ten NWs have merged into a large hexagonal structure. A few separately grown NWs are also present. In (b) a similar assembly of NWs imaged from below can be seen.

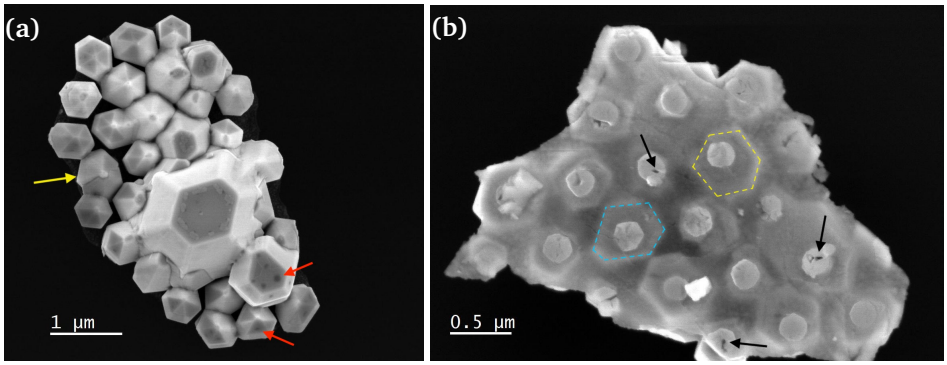

Figure 4.2: Two NW assemblies deposited onto the grid with the c-axis pointing (a) up and (b) down. In (a) a NW with a fracture along the c-axis is indicated with a yellow arrow. Dark spots on the c- and semi-polar facets are indicated with red arrows. In (b) voids on the initial growth site are indicated by black arrows. The distorted hexagonal shape of two NWs has also been indicated.

In many instances the SiO_2 mask remains attached to the NWs after sample preparation. Some NWs are, although growing separately from other NWs, indirectly attached to each other through the mask layer, as illustrated in Figure 4.3. The mask and a hole in the mask have been indicated in Figure 4.3(a) and the same SE contrast from Figure 4.1 is marked with white arrows. These NWs tend to deposit with random orientation. Larger clusters are more commonly seen deposited with the c-axis perpendicular to the grid, either pointing into the grid or out of the grid, as seen in Figure 4.2. The hole pattern is hexagonal and the spacing of the holes is found to be 594 ± 7 nm, based on Figure 4.2(a) and similar images. Variation in SE yield is also seen for these assemblies, where the SiO_2 mask appears darker than the initial growth site inside the holes.

In Figure 4.2(a) the tapered top shape of the NWs can be seen from the edge contrast of the facets. Most NWs appearing separated have pointed tips, whereas larger agglomerates appear with flat top shapes. One of the NWs in Figure 4.2(a),

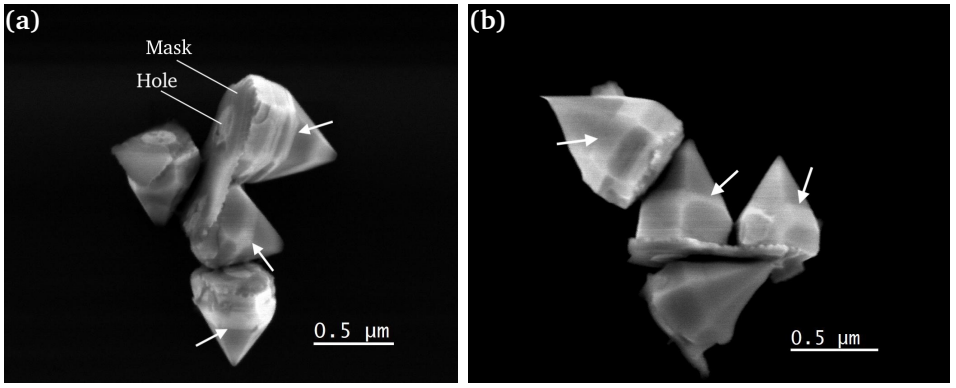

Figure 4.3: A change of the SE contrast is also detected for NWs prepared on grids. This trend is seen for NWs pointing in various directions in (a) and (b), indicated with white arrows. The mask and a hole in the mask have been indicated in (a). A scan artefact from charging can be seen for the top left NW in (b).

indicated with a yellow arrow, has a fracture across the NW cross section. Unlike the light edge contrast seen at the interfaces between facets, the fracture appears darker than the NW. Dark spots are seen at the c- and semi-polar facets in Figure 4.2(a), indicated with red arrows. In some of the holes in the mask in Figure 4.2(b) small voids can be seen, indicated with black arrows. The distorted hexagonal shape of the NWs and the position of the NWs compared to the holes can also be seen through the mask.

In Figure 4.4(a) a larger assembly of NWs with the c-axis pointing into the plane can be seen. In Figure 4.4(b) NWs still attached to the sapphire substrate, with the c-axis pointing out of the plane, is shown. When comparing the two, it can be seen that for Figure 4.4(a) the pattern of holes in the mask is close to perfect hexagonal from the EBL step. For the NWs in Figure 4.4(b), on the other hand, it is harder

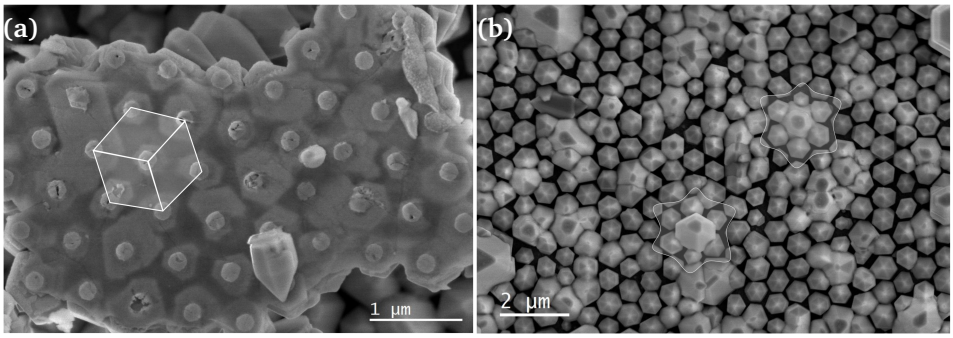

Figure 4.4: Top view SEM images from the substrate after grid preparation of (a) a flake of NWs flipped such that the hexagonal hole pattern is revealed. In (b) NWs still attached to the sapphire substrate can be seen from the top. Two areas where one NW has overgrown the six surrounding NWs are marked.

to recognise a hexagonal pattern, as the NWs are not centred about the holes but slightly shifted away from them. In addition, the coalescence distorts the pattern. The in-plane orientation of the NWs varies, that is, no preferred orientation about the c-axis is detected.

SEM inspection after sample preparation

SEM acquired from the sapphire substrate after conducting the preparation routine described in section 3.2 is shown in Figure 4.5 and Figure 4.6. Figure 4.5(a) shows the region where area 100_600 has been scraped off. It is evident that also some of area 80_600 has been scraped off. The zoomed-in area in Figure 4.5(b) shows a 20 μm thick scratch in area 80_600. The SEM image in Figure 4.6(a) was acquired from the lower left corner of area 100_600 in Figure 4.5(a), where some NWs are still attached to the sapphire substrate. Two different contrasts can be seen in the top left corner of Figure 4.6(a), where the NWs have been scraped off. The dashed line indicates the border of area 100_600. In the bottom right corner parasitic growth on top of the mask can be seen. In Figure 4.6(b) dark features of circular shape, separated by approximately 600 nm in a hexagonal pattern are indicated. This pattern appears sporadically over the entire substrate. Some cracks in the substrate are also observed.

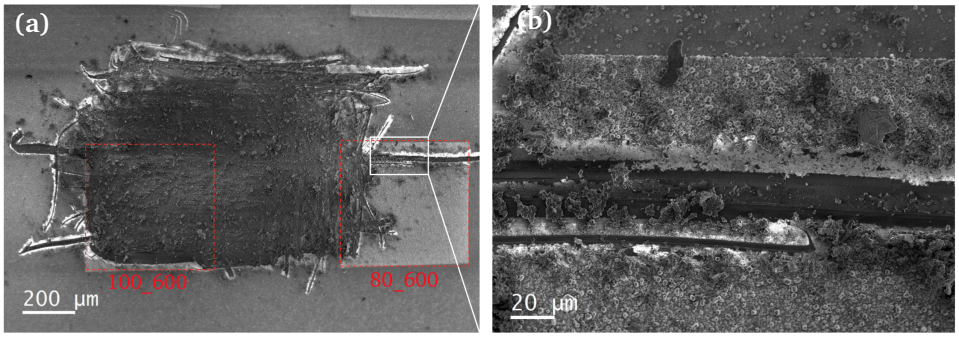

Figure 4.5: Top view SEM image of the sapphire substrate after preparing grids from area 100_600 (see image 3.2). (a) From the overview image it can be seen that also some of the NWs from area 80_600 have been scraped off. (b) The zoomed-in area shows a scratch with flakes of various sizes detached from the substrate.

Parasitic growth on mask

Apart from the intentional growth in the holes of the SiO_2 mask, irregular growth is also observed on top of the mask. This is illustrated with HAADF STEM, SAED pattern and EDS in Figure 4.7. The SAED pattern in Figure 4.7(b) shows that the crystallites grow with random orientation. By measuring the radius of the second and third diffraction ring, represented by dashed lines in the radially integrated intensity profile in Figure 4.7(c), the ratio between the two was found to be approximately 0.877. The diameter of the hexagonal crystallites varies from less

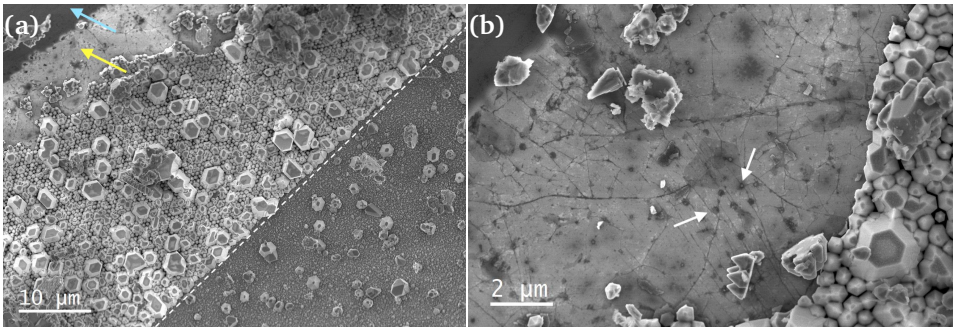

Figure 4.6: SEM images from substrate after preparation of grids by scribing. In (a) two different contrasts from the scribed area is indicated. The dashed line represents the edge of area 100_600 and some growth can be seen on the mask in the bottom right corner. In (b) dark features separated with approximately 600 nm with circular shape in a hexagonal pattern are indicated on the scribed area. Cracks in the substrate can also be seen.

than 100 nm to more than 500 nm, as seen from HAADF STEM in Figure 4.7(a). A layer with higher Al percentage and lower Ga percentage is detected with EDS in Figure 4.7(d).

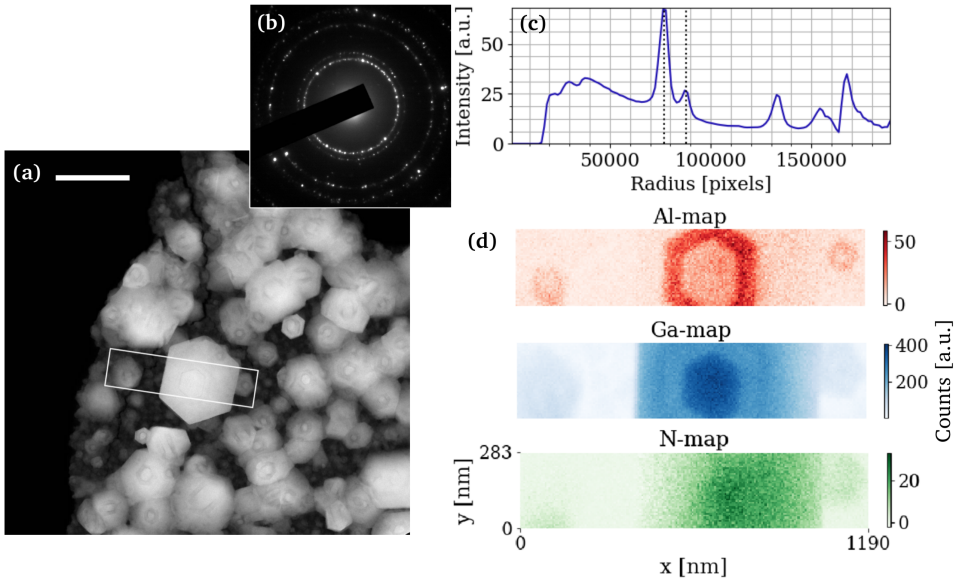

Figure 4.7: (a) HAADF STEM image from part of sample with parasitic growth on top of the mask. The scale bar is 500 nm. In (b) the SAED pattern for this cluster is given and in (c) the integrated intensity over the 2π radius is presented. In (d) EDS from the rectangular region in (a) is given.

4.2 Correlated study

For the rest of this chapter six individual NWs and one larger cluster will be considered for every applied technique. A representative selection of the results will be presented and the rest will be given in Appendix D and Appendix E.

4.2.1 SEM

NW orientation and morphology

SEM from the seven specimens is shown in Figure 4.8, together with the corresponding labels (NW1, NW2, etc.) that will be used throughout this work. All of the individual NWs, except for NW4, have their c-axis pointing vertically. The orientation of the NWs during SEM and CL acquisition is as-deposited from the preparation routine described in section 3.2. That is, the NWs are not systematically reoriented onto a specific zone due to limited tilt control in the experimental setup. NW2, NW5 and NW6 are slightly tilted into the paper plane, so that the hole from the mask is visible, illustrated with yellow arrows in Figure 4.8. NW4 is oriented with the c-axis pointing out of the paper plane. Edge contrast

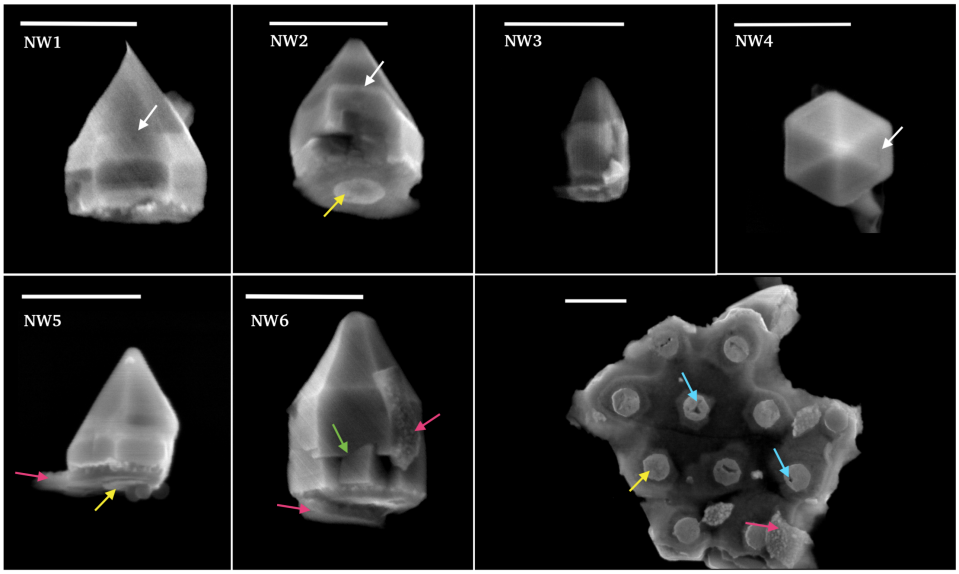

Figure 4.8: SEM images of the six individual NWs in this correlated study and a larger cluster. All NWs but NW4 are oriented with the c-axis pointing up. NW4 is oriented with the c-axis pointing out of the paper plane and the cluster with the c-axis pointing into the paper plane. All scale bars are 500 nm. Arrows represent SE contrast chance (white), holes in mask (yellow), SiO_2 mask (pink), voids (blue) and change of facets (green).

reveals the facets of the NWs and the SE contrast change discussed in section 4.1 is present for NW1, NW2 and NW4, indicated with white arrows. Some of the SiO_2

mask is still attached to NW5, NW6 and the cluster. This is shown with pink arrows in Figure 4.8. All NWs have pointed tips, and for NW6, a clear change of facet can be seen, indicated with a green arrow. The NWs display more defects towards the bottom in general, according to the shape and the contrast seen in this region. The larger cluster consists of eleven NWs attached to each other through the mask or through coalescence caused by radial growth. The cluster is seen from below, that is, the c-axis is pointing into the paper plane. Mainly the mask, but also the initial growth site in the holes is displayed. Through the mask the distorted hexagonal shape of the NWs is visible. In some of the holes, the NWs have voids indicated with blue arrows.

4.2.2 HAADF STEM and TEM

Radial heterostructure

HAADF STEM images of the seven constituents of the correlated study can be seen in Figure 4.9. All of the NWs are reoriented onto the [11$\bar{2}$0] zone, except for NW4

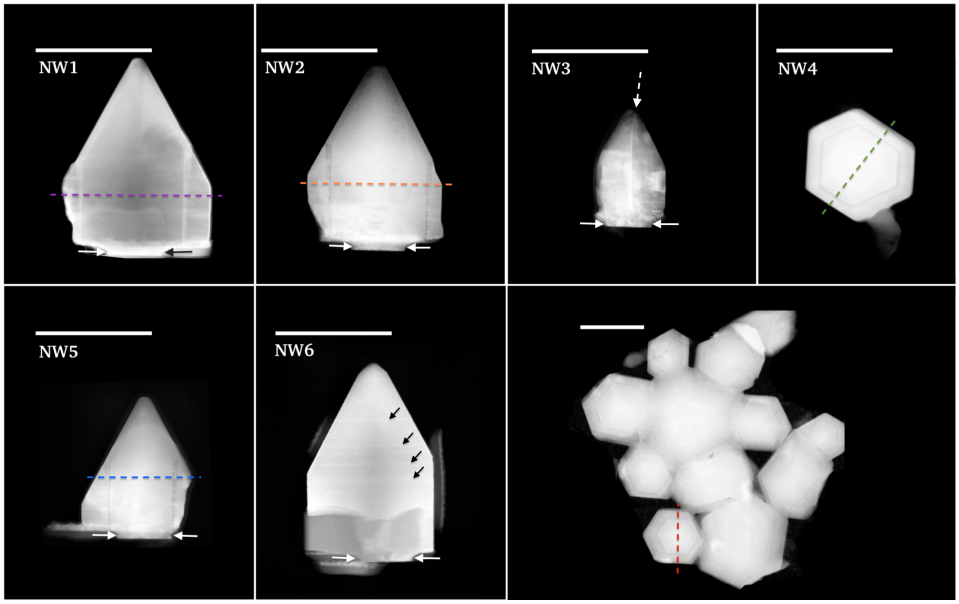

Figure 4.9: HAADF STEM images from all seven specimens. Most NWs are on zone [11$\bar{2}$0], except for NW4 and the cluster, which are on zone [0001]. The radial heterostructure can be seen for NW1, NW2, NW4, NW5 and the cluster and the indicated profiles from the dashed lines are plotted in Figure 4.10. Double arrows indicate the hole in the mask. Stacking faults for NW6 and a fracture in NW3 have been indicated with black arrows and a white arrow, respectively. All scale bars are 500 nm.

and the cluster, which are reoriented onto zone [0001]. Because the orientation is random during SEM acquisition, the NWs appear different in SEM compared to in HAADF STEM and TEM. The average diameter and length of the NWs is 499 ± 113

nm and 574 ± 115 nm, respectively. The dashed lines along the m-planes in Figure 4.9 represent the intensity profiles given in Figure 4.10(a). A radial heterostructure can be seen for NW1, NW2, NW4, NW5 and the cluster. The heterostructure is composed of a light core, a dark intermediate shell and a light exterior shell. In the profiles presented in Figure 4.10(a) the dark intermediate shell is represented by local minima. For NW4 the intrinsic GaN layer ($\sim$ 5 nm thick) is observed just outside the core in Figure 4.10(b) as a local maximum. In NW1 the relative contrast in the heterostructure is reversed. That is, the exterior shell and the core appear darker than the intermediate shell. The thickness of different layers is found to vary for different planes and also within planes. These results are summarised in Table 4.1. The n-AlGaN core and the p-GaN contact layer is found to exhibit the largest variation in thickness. The p-AlGaN layer shows the smallest variation. The angle between the m-planes and the semi-polar planes is found to be $152.5 \pm 0.9°$.

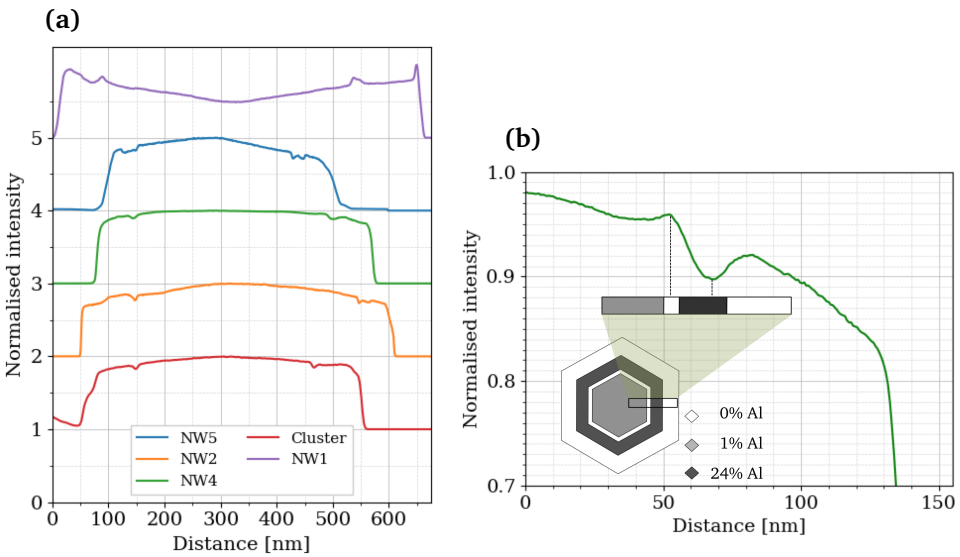

Figure 4.10: (a) HAADF STEM intensity profiles indicated for NW1, NW2, NW4, NW5 and the cluster in Figure 4.9. The dark intermediate shell is seen as local minima. For NW1 the relative intensity has been reversed and the same layer appears as local maxima. A zoomed-in area from NW4 is given in (b), where the contrast from the intrinsic GaN layer can be seen as a local maximum. The colours in the schematic illustrate the nominal Al percentages.

Crystal quality and irregularities

BF TEM images and the corresponding diffraction patterns from NW5 and NW2 on zone axis $[11\bar{2}0]$ can be seen in Figure 4.11. All NWs are found to have WZ crystal structure. Some of the NWs exhibit thick layers of carbon contamination after SEM and CL acquisition. This is seen as a light grey layer covering NW5 in Figure 4.11(a). Plasma cleaning was applied to the grids before TEM acquisition, but was found to be detrimental to the carbon film.

Table 4.1: Based on the radial heterostructure detected from HAADF STEM, the average thickness based on all inspected NWs is summarised for all layers in this table. The intrinsic layer was only detected for NW4 and only the core layer is detected for NW6.

Component	**Average thickness [nm]**
Core (n-$Al_{0.01}Ga_{0.99}N$)	221.7 ± 151.8
Intrinsic layer (u-GaN)	~ 5
p-doped layer (p-$Al_{0.24}Ga_{0.76}N$)	25.8 ± 3.40
Contact layers m-plane* (p-GaN)	65.6 ± 26.0
Contact layers r-plane (p-GaN)	6.59 ± 4.96

* The thickness of the contact layer is separated into the m- and the r-plane, due to a large difference between the two.

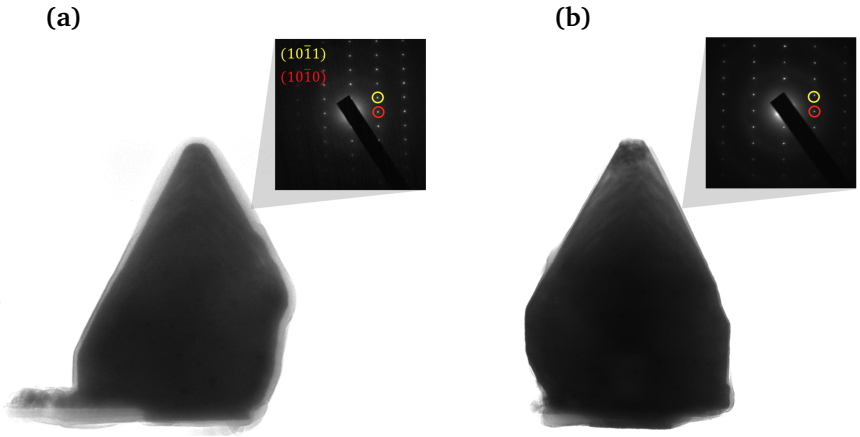

Figure 4.11: (a) BF TEM image of NW5 on zone axis $[11\bar{2}0]$, where the corresponding diffraction pattern is given. In (b) the same is shown for NW2. Carbon contamination can be seen for both. The diffraction spots from $(10\bar{1}1)$ and $(10\bar{1}0)$ are indicated.

Compared to SEM, inspection by HAADF STEM reveals additional irregularities in the NWs. Basal plane stacking faults (BSFs) as horizontal lines, for example, are indicated for NW6 in Figure 4.9. The initial NW growth inside the hole of the mask and the sharpness of the mask etch can be observed with HAADF STEM on zone $[11\bar{2}0]$. The holes in the mask are marked with double arrows in Figure 4.9. In general, the contrast in the lower ~ 250 nm of the NWs is more irregular. NW3 appears with irregular contrast across the entire NW.

The SiO_2 mask attached to some on the NWs, for example on the semi-polar planes of NW6 in Figure 4.9, appears dark with a bright layer of rough morphology deposited on top. The thickness of the mask is measured to be 34 ± 4.6 nm. Similar voids seen for the cluster in Figure 4.8 are discovered for some NWs with HAADF

STEM side view. This is shown in Figure 4.12(a), where the void has resulted in a fracture along the c-axis of the NW. The radial heterostructure for this NW is only visible on the right hand side, that is, the crystal structure on either side of the fracture has slightly different orientation. In the HAADF intensity profile in Figure 4.12(c) the valley close to the centre of the NW, at approximately 320 nm, represents a relative deep fracture. HAADF STEM of NW3 in Figure 4.9 reveals a fracture similar to the one seen from above in Figure 4.2(a). In the BF TEM image of NW3 in Figure 4.12(d) the different contrasts on either side of the fracture represent two different orientations. In general, NW3 is smaller than the rest of the NWs in the correlated study and exhibits more irregularities. In Figure 4.13(a)

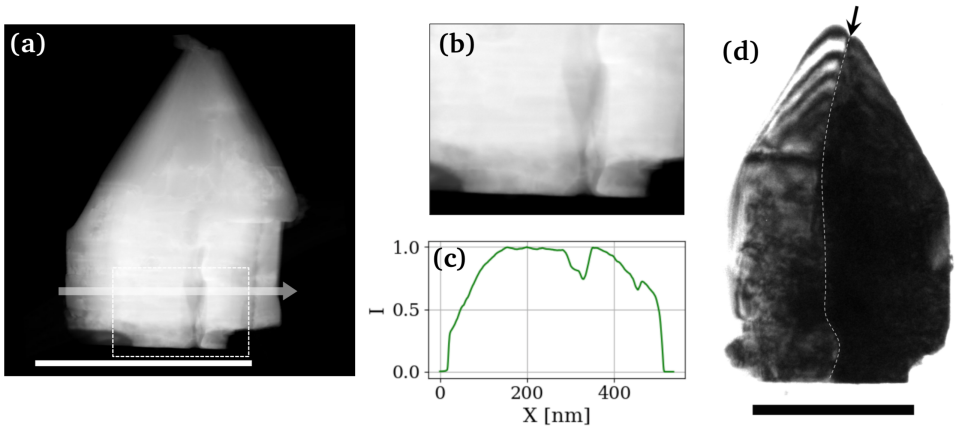

Figure 4.12: (a) NW where a fracture originates from a void in the initial growth site. A similar void was seen in the cluster in Figure 4.8. The scale bar is 500 nm. In (b) a zoomed-in area from the fracture is given and in (c) the HAADF intensity profile across the NW, indicated with an arrow in (a), is presented. In (d) a BF TEM image from NW3 is given where a fracture can be seen along the c-axis. The scale bar is 200 nm.

a NW cluster consisting of two NWs is shown. For one of the NWs a gap is present between the SiO_2 mask and the NW. This is shown in Figure 4.13(b). Growth has occurred on top of the mask in the gap. For the other NW there is no gap, but a dark feature can be seen at the initial growth site, shown in Figure 4.13(c).

4.2.3 EDS

Qualitative mapping of radial heterostructure

EDS elemental mapping of the different components of AlGaN for NW5 is given in Figure 4.14. The same radial heterostructure detected by HAADF STEM is recognised with EDS. The dark intermediate shell layer in Figure 4.9 is found to exhibit high Al content and corresponding low Ga content, compared to the surrounding layers. The same trend is shown in the line scan in Figure 4.15. The N content is more or less uniform across the NW and the intrinsic GaN layer is not resolved. There is a significant difference in the signal intensity for the three

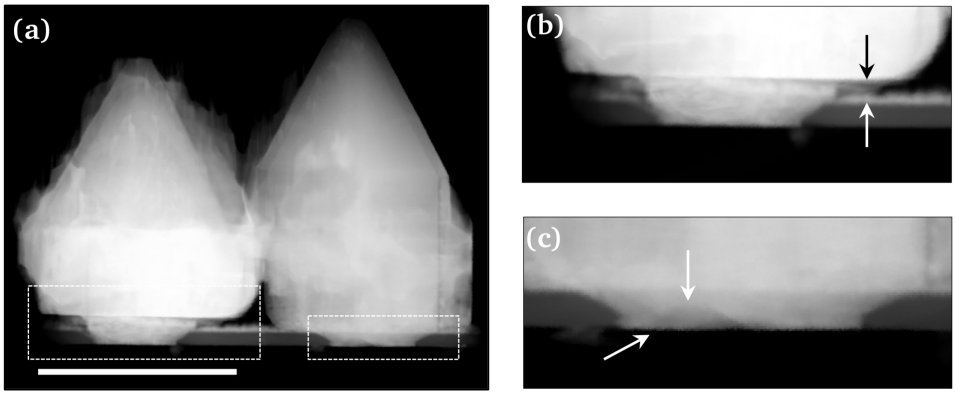

Figure 4.13: (a) Two NWs showing different growth characteristics. The scale bare is 500 nm. (b) One of the NWs has a gap between the mask and the NW due to growth on top of mask. (c) For the other NW there is no gap, but a dark contrast can be seen at the bottom.

elements, as indicated by the scales in Figure 4.14. EDS element maps for the remaining NWs show similar trends and are given in Appendix D.

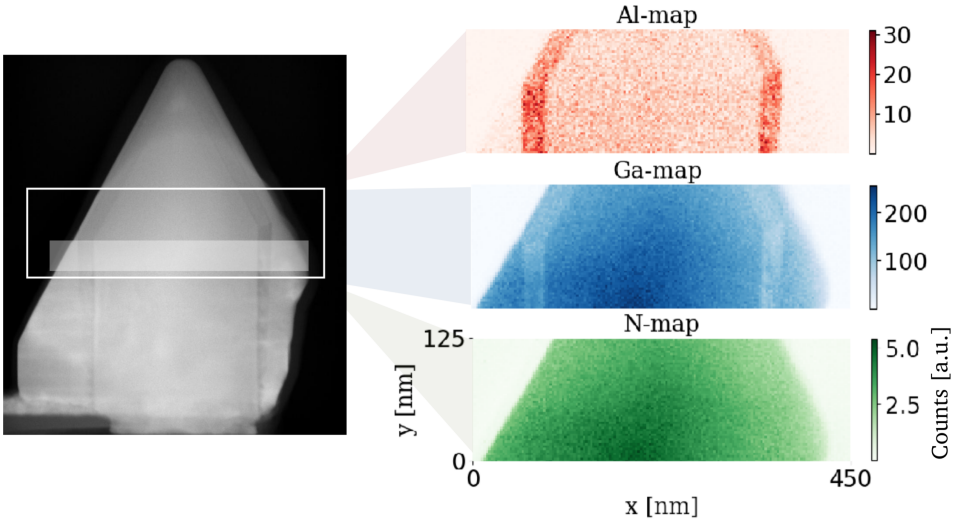

Figure 4.14: EDS elemental mapping of Al, Ga and N from the rectangular region of interest in the HAADF STEM image of NW5. An increase in Al and a corresponding decrease in Ga is seen for the dark shell layer in the HAADF STEM image. The broad line indicates the area for the line scan in Figure 4.15 and Figure 4.16.

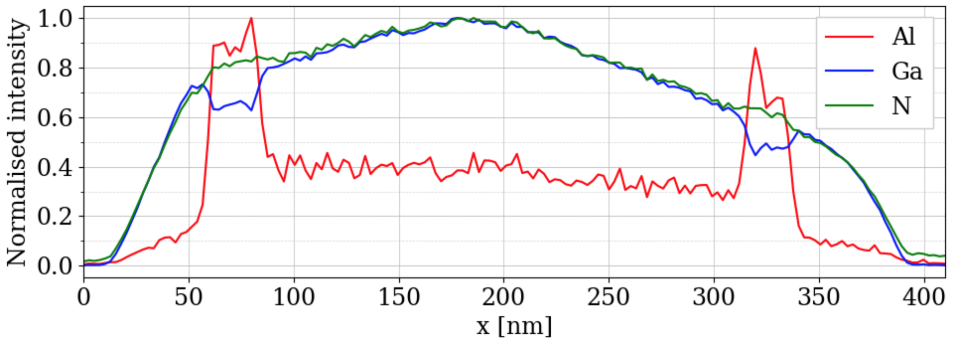

Figure 4.15: Normalised EDS line scan from the filled rectangular area in Figure 4.14. The increase in Al and the corresponding decrease in Ga can be seen around 75 nm and 325 nm.

Quantitative mapping of radial heterostructure

In Figure 4.16 a quantitative EDS line scan generated by the Cliff-Lorimer method is given for the same area as the qualitative line scan in Figure 4.15. The applied k-factors are extracted from the AZtec software and the code for the Cliff-Lorimer quantification is attached in Appendix B.2. The atomic percentage of N on average is found to be $< 30\%$ across the NW.

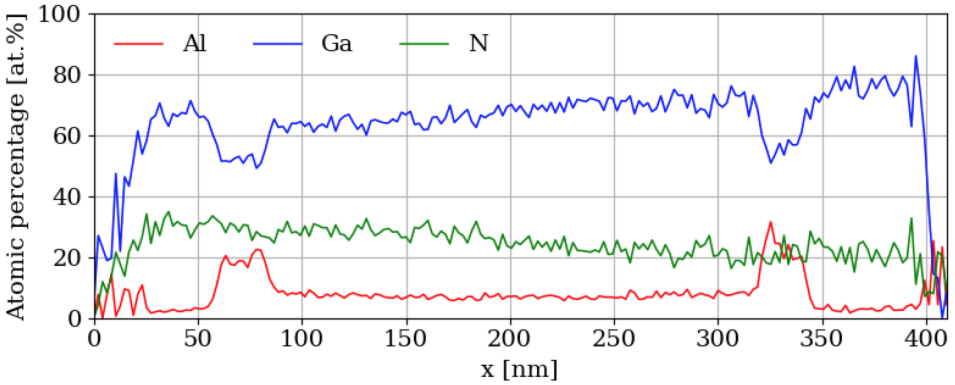

Figure 4.16: Quantitative line scan from the filled rectangular area in Figure 4.14. The Cliff-Lorimer method is applied with k-factors from the AZtec software to determine the atomic percentage of Al, Ga and N (see Appendix B.2).

4.2.4 CL

Mapping of NW luminescence

The integrated intensity distribution in the wavelength range 340-380 nm can be seen for all individual NWs in Figure 4.17. This interval is chosen as it covers the desired wavelength range for the UV LED. A histogram presenting the highest

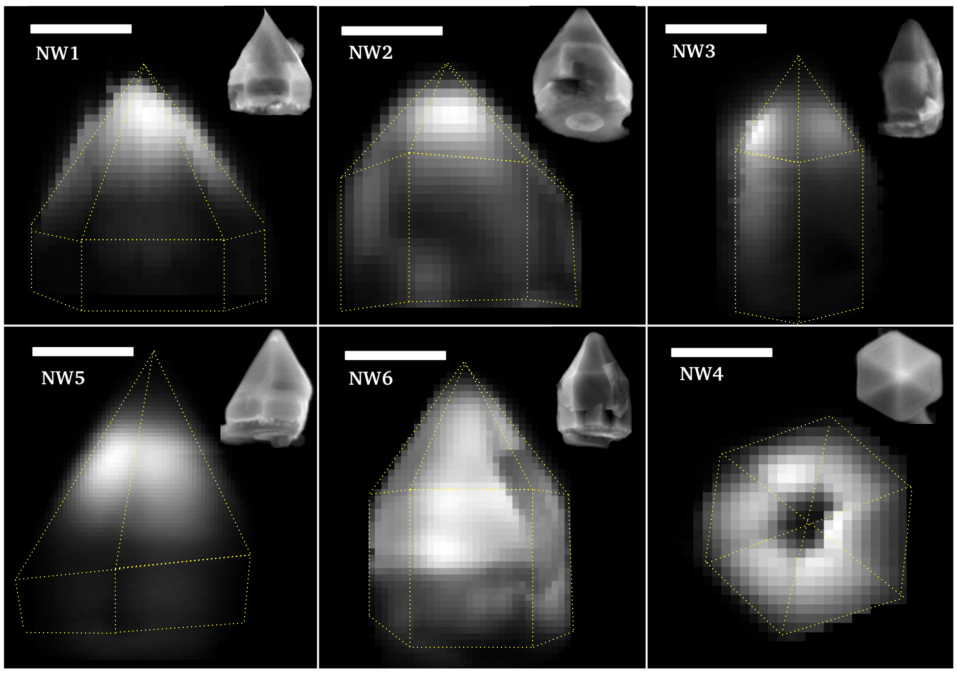

Figure 4.17: Hyperspectral CL images from all six individual NWs. The data is created by integrating the intensity range 340-380 nm (see Figure 2.43) before PCA denoising is performed. The scale bar is 200 nm and the corresponding SEM image is given for all NWs. The facets are indicated. Charge carrier diffusion must be taken into account when inspecting these images.

intensity and most frequently occurring peaks is given in Figure 4.18. The most frequent peak is centred about 361 nm. In general, the intensity in the desired wavelength range decreases from top to bottom of the NWs, which can be seen from the contrast in Figure 4.17. The intensity is also low at interfaces between different facets. NW4, for example, exhibits very low intensity at the tip of the NW where all six semi-polar facets interface. NW3 shows the lowest overall intensity. The orientation of the NWs during CL acquisition is the same as for SEM, and therefore the corresponding SEM image is attached for all specimens in Figure 4.17. The facets according to the SEM images have also been indicated with dashed lines.

A three-dimensional plot of the spectra from a column of pixels along the c-axis of NW5 can be seen in Figure 4.19(a). A decrease in intensity from the top to

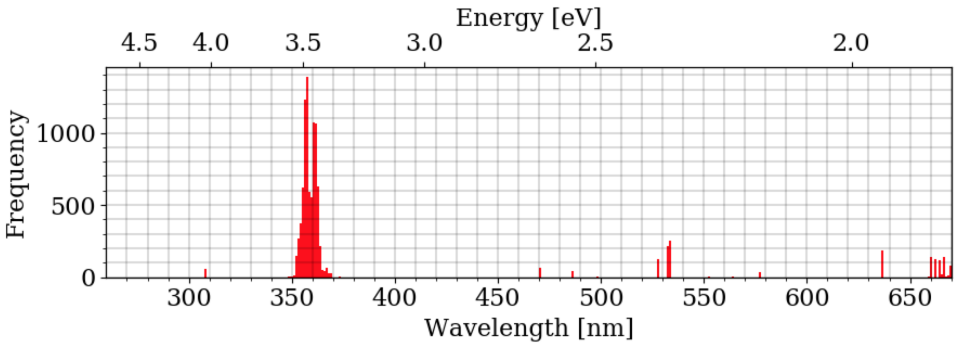

Figure 4.18: Histogram showing the most frequent and highest intensity occurring peaks among all NWs. The data is gathered by detecting the global maximum in the spectrum of every pixel for all NW data after PCA. The most frequent peak is at 361 nm. The CL detection system has a resolution of ~ 0.2 nm and the binning is here set to 1 nm.

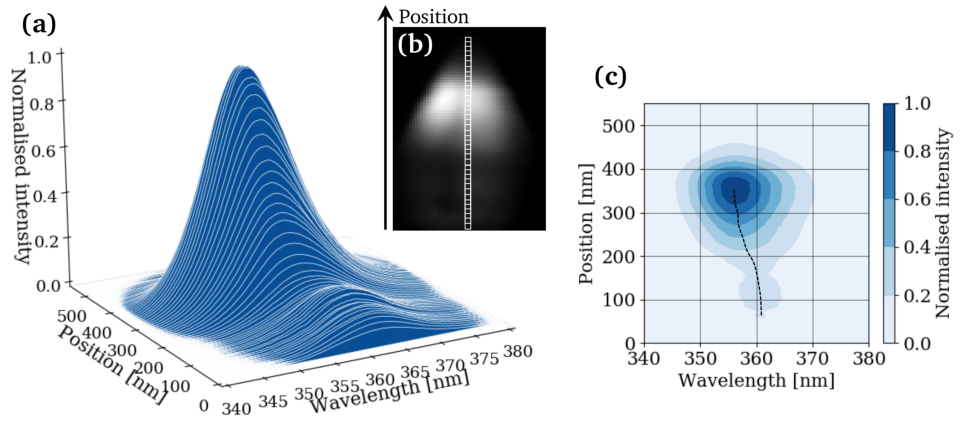

Figure 4.19: (a) For NW5 the intensity in the range 340-380 nm is decreasing significantly from the top of the NW to the bottom. In (b), the position of the pixels from where the spectra in (a) are extracted along the NW is indicated. (c) The peak position also shifts towards longer wavelengths for lower parts of the NW, indicated with a dashed line in the contour plot.

the bottom of the NW is observed. The peak centre position also shifts towards longer wavelengths by approximately 5 nm, which is illustrated by a dashed line in the contour plot in Figure 4.19(c). The column of pixels is illustrated in Figure 4.19(b). The same trend is observed for all individual NWs in the correlated study (see Appendix E).

CL was acquired from one of the holes in the mask for the larger cluster. The results are given in Figure 4.20, where in (a) the inset shows the integrated intensity for the wavelength range 260-672 nm from the bottom of a NW. In the resulting spectrum in Figure 4.20(b), peaks are observed at 274 nm and 550 nm with low intensity and at 363 nm with high intensity. FWHM for the peak at 550 nm

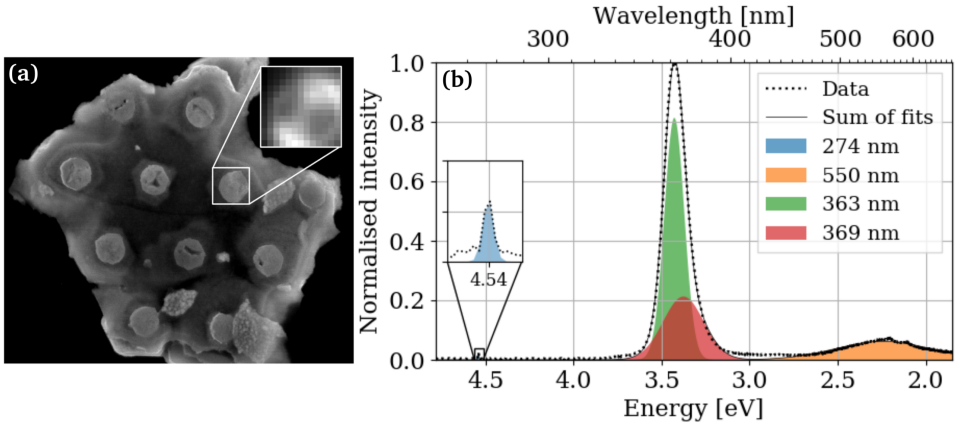

Figure 4.20: (a) SEM image of the cluster, where the integrated intensity in the range 260-672 nm for one of the NWs is shown in the inset. The average spectrum is given in (b), where four Gaussian components have been suggested.

is significantly larger than for the other peaks. The spectrum in Figure 4.20(b) is the average over all pixels in the inset in Figure 4.20(a). A Gaussian decomposition is performed in eV-space and an additional peak centred about 369 nm is found.

In Figure 4.21 the wavelength distribution at maximum intensity for NW5 and NW4 is presented. The longest wavelengths are found at the bottom and on the edges of both NWs. The shortest wavelengths are found on the semi-polar planes. The wavelength distribution for the rest of the NWs is given in Appendix E.

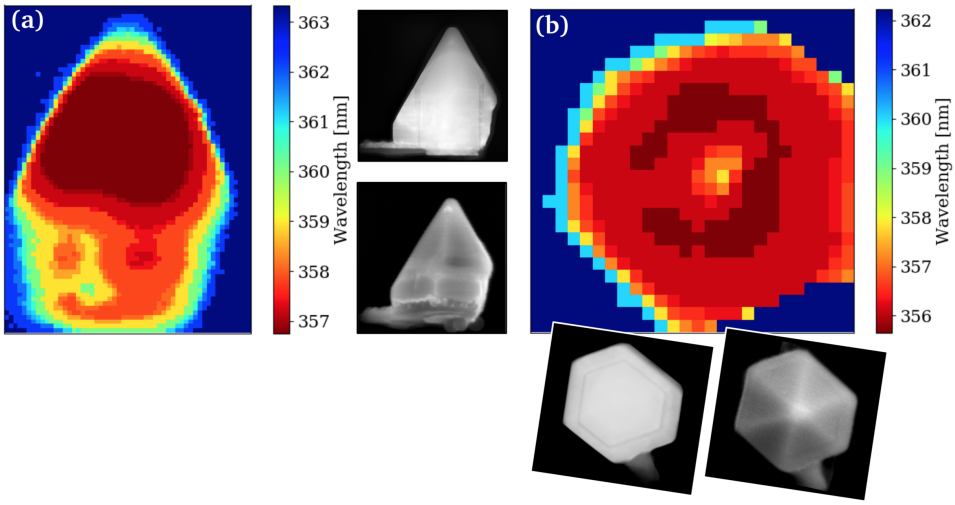

Figure 4.21: Maps showing the wavelength distribution at maximum intensity for (a) NW5 and (b) NW4 in the wavelength range 340-380 nm. The data is generated by detecting the wavelength at maximum intensity for every pixel after PCA denoising. The corresponding SEM and HAADF STEM images are attached.

NMF decomposition analysis

In order to explore emission in different bands, a NMF decomposition analysis is performed on the hyperspectral CL data. The results are presented in Figure 4.22 for NW4, NW1 and NW2. The number of components the data is decomposed into is determined by SVD in the form of a scree-plot. PCA denoising is applied before the decomposition, similar to the approach used in [86]. The applied method is described in detail in Appendix E. For all six individual NWs three similar NMF components were found, centred about 354 ± 5 nm, 357 ± 5 nm and 362 ± 5 nm, respectively. The three spectral components and the corresponding intensity loadings are given in Figure 4.22. The data for the three remaining NWs is presented in Appendix E. In general, component 1 and 2 overlap but component 1 is confined to a smaller area towards the tip of the NWs. Component 2 has the highest intensity for the majority of the NWs. The tip of NW4 in Figure 4.22(a)

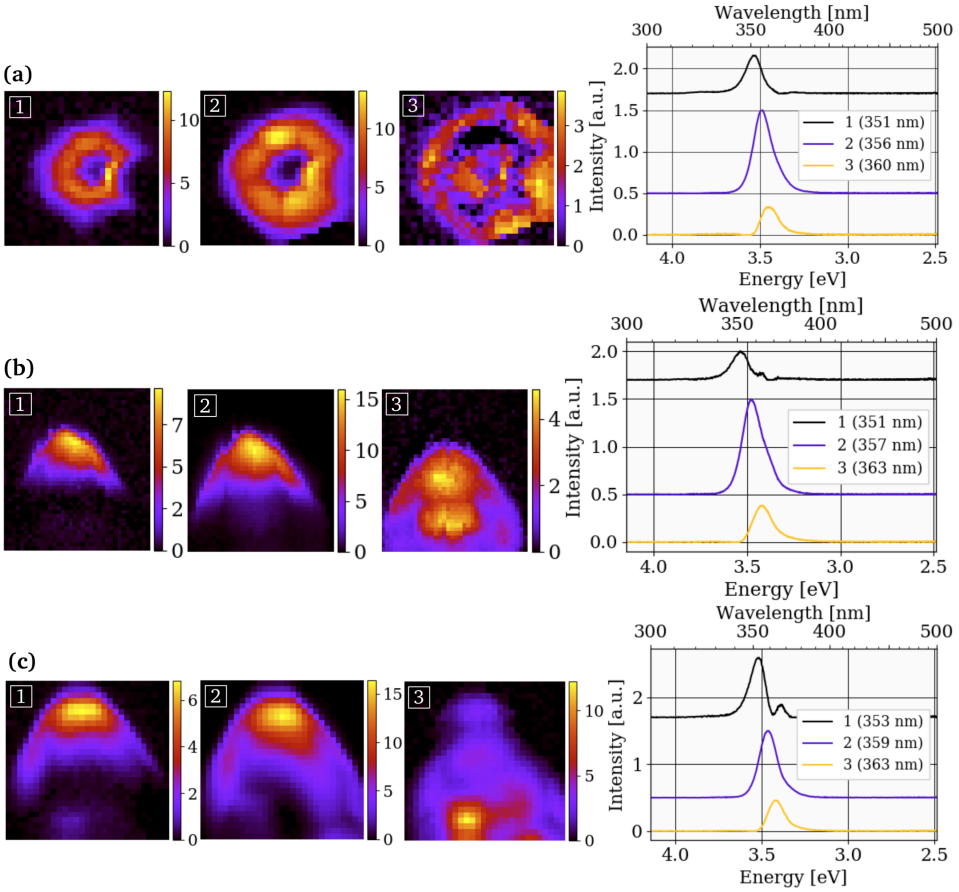

Figure 4.22: NMF decomposition in the wavelength range 330-500 nm of (a) NW4, (b) NW1 and (c) NW2 into three components; 1, 2 and 3. The spectral components (peak maximum given in parentheses) and their loadings are shown.

has low intensity for all components, except for component 3. For NW2 in Figure 4.22(c), component 3 shows high intensity emission for a confined region at the bottom of the NW.

In Figure 4.23(a), four NMF components from decomposition of NW1 is presented. The wavelength range for this decomposition is larger than for the decomposition performed on the same NW in Figure 4.22(b). In addition to component 1 and 2, which were observed for all three NWs in Figure 4.22, peaks centred about 307 nm and 527 nm with narrow FWHM are detected. This is illustrated with component 3 and component 4 in Figure 4.23(a). Both wavelengths are found in the histogram in Figure 4.18. In Figure 4.23(b) three NMF components from decomposition of the cluster are presented. Here, two of the NMF components from Figure 4.22 can be seen and an additional broad peak centred about 563 nm, illustrated in Figure 4.23(b) with component 3. The same NMF component also has a peak centred about 274 nm, as shown in the inset. This peak was found from the Gaussian decomposition of the cluster in Figure 4.20(b).

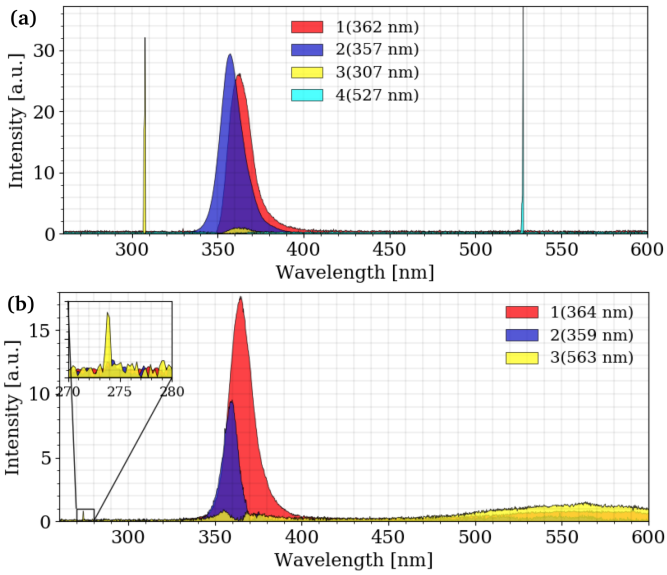

Figure 4.23: (a) Two additional peaks, centred about 307 nm and 527 nm with small FWHM, are extracted from NMF for NW1 in the wavelength range 350-600 nm. This is represented by component 3 and 4. (b) For the cluster, an additional broad peak centred about 563 nm is detected. This is represented by NMF component 3. Another peak is detected at 274 nm in the inset from the same component. A Gaussian decomposition was applied to the same data in eV-space in Figure 4.20.

A NMF decomposition in the wavelength range 430-672 nm was also conducted. A broad peak centred about approximately 540 nm is common for several NWs. In Figure 4.24, this component and the corresponding loading map is given for NW2, NW1 and NW4.

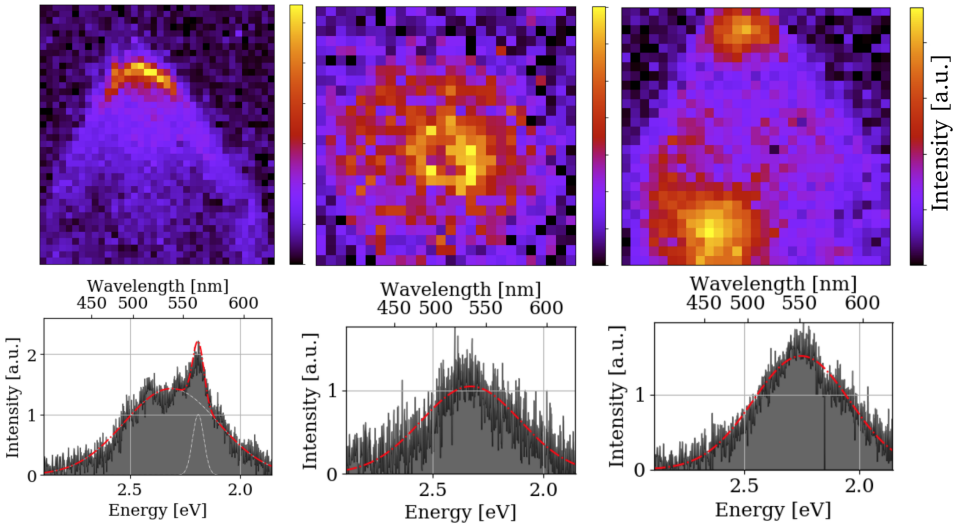

Figure 4.24: NMF loadings and spectral components with Gaussian fits in the wavelength range 430-670 nm for NW1, NW4 and NW2.

The intensity for all three NWs shows higher counts towards the tip of the NW. From Figure 4.20(b) a significant peak in this band is also detected from the bottom of the NWs.

5 Discussion

The aim of this study includes correlated characterisation of optical, structural and compositional properties of individual AlGaN NWs. The purpose of correlating these properties is to recognise the underlying structural and compositional details contributing to the efficiency constraint. NW defects and growth mechanisms are also discussed, based on analysis of the obtained results. Results from SEM, CL, STEM and EDS are together discussed in the following sections covering structural, compositional and optical characterisation. Finally, the correlated findings are discussed. Similar studies have been conducted in [59].

5.1 Structural characterisation

Single NWs were chosen for the detailed correlated study, as this is the targeted structure for selected-area growth with a patterned mask. One cluster is also included since it contributes to the study of the NW growth mechanism. The efficiency of the sample preparation routine described in section 3.2, that is the number of NWs deposited onto the grids, is low and therefore this study is statistically limited. However, six individual and representative NWs and one cluster could be studied in a correlated manner.

Growth uniformity

The selected AlGaN NWs for the detailed study are found to have an average diameter of 499 ± 113 nm and a length of 574 ± 115 nm. These values result in an aspect ratio of only 1.15 ± 0.427, due to the significant radial growth exhibited by the NWs. This is not a typical value for the aspect ratio of NWs [89]. However, in lack of a better name the author has chosen to stay with the name nanowires. Alternative names commonly used in literature are nanoclumns, nanorods, nanocones, pyramids, etc. [90, 91, 92]. The NWs appear with hexagonal cross sections and pointed tips, as seen in Figure 4.2. The exception is larger clusters, which appear with more irregular shapes and truncated tips. Similar geometries for position-controlled catalyst-free grown GaN NWs are reported in [93, 94]. However, the hexagonal cross section of the NWs in this study appears more or less distorted. The NWs consist of a stem and a sloped top region, which is made up from the m-planes and semi-polar planes, respectively. The average angle measured between the two is $152 \pm 0.9°$, which corresponds well to the angle

between the r-plane and the m-plane (see Figure 2.17) [95]. However, many studies report the semi-polar planes as $\{1\bar{1}01\}$ and not the r-plane ($\{1\bar{1}02\}$) for MOCVD grown GaN NWs [93, 94, 96]. These planes would correspond to an angle of approximately $133°$ between the semi-polar plane and the m-plane. That is, the pyramidal top shape of the NWs in the current study appears steeper. An illustration of the observed NW geometry variations is presented in Figure 5.1.

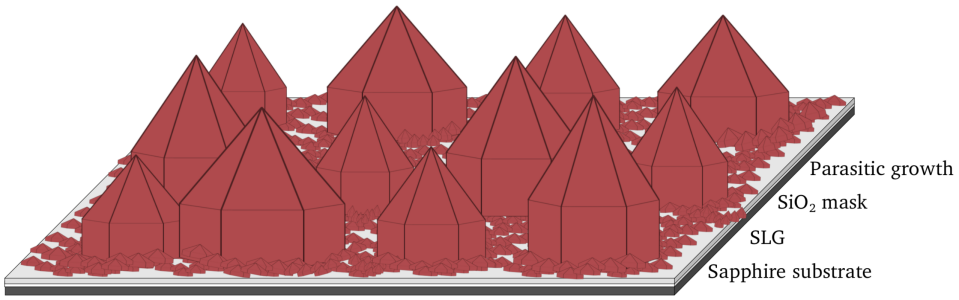

Figure 5.1: Illustration of the variation in NW uniformity. The parasitic growth on top of the SiO_2 mask is also shown. The displayed facets are the m- and r-planes. NW coalescence can be seen in the lower left corner.

The thickness of the different components of the radial heterostructure in Figure 4.9 was summarised in Table 4.1. The thickness of the p-GaN layer on the r-planes constitutes on average only about 10% of the thickness of the same layer on the m-planes. This is caused by a difference in growth rate for the two facets. The same trend was observed for a MQW NW structure in [97], which was explained by the surface energy and the stability of surface atoms on the r-planes. The reason why this difference is not seen for other layers in the present study is most likely because the MOCVD growth parameters differ significantly for the p-GaN layer. Another explanation is based on the surface mobility of Al and Ga atoms. Because the mobility of Al is inferior, growth of higher Al percentage layers is less prone to diffusion before settling at a crystal site. For GaN, on the other hand, diffusion might cause the atoms to consistently move to other preferred facets due to larger surface mobility.

The radial heterostructure was observable only when then NWs were rotated onto or close to the $[11\bar{2}0]$ zone, as seen in Figure 4.9. The reason for this is illustrated in Figure 5.2. For some areas at zone $[11\bar{2}0]$ the majority of the material the electron beam passes through consists of the the dark shell structure, which in the case of this study is a layer of high Al percentage. Al has atomic number 13 and results in a darker contrast in HAADF STEM compared to Ga with atomic number 31, due to less scattering events. On zone $[01\bar{1}0]$, on the other hand, the beam passes through many layers such that the resulting contrast averages out.

From the diffraction pattern of the NWs, shown for NW5 and NW2 in Figure 4.11, the crystal structure is found to be WZ, which is noncentrosymmetric and has polarisation along the c-axis. This is commonly observed for GaN NW growth [97, 93]. For the parasitic growth on the mask, the orientation of the different

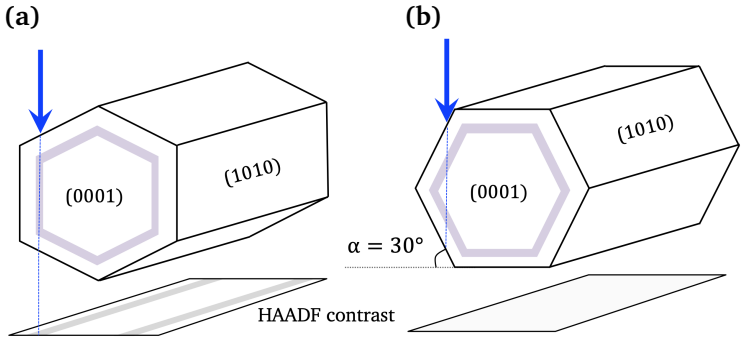

Figure 5.2: Illustration of the difference between (a) $[11\bar{2}0]$ and (b) $[01\bar{1}0]$ for the radial heterostructures in HAADF STEM. The dark shell structure represents a layer with lower atomic number, which can be seen from the resulting Z-contrast. Contrast variations due to thickness variations have been ignored

crystals was found to be random. The parasitic growth was illustrated in Figure 5.1. The ratio between the radius of the second and third diffraction ring in Figure 4.7(b) (from $(01\bar{1}0)$ and $(01\bar{1}1)$) was found to be approximately 0.877. From Equation 2.21, Equation 2.24 and the lattice constants in Table 2.1, it is found that for an AlGaN alloy this ratio should exist in the interval $\{0.845, 0.852\}$. Hence, the parasitic growth on top of the mask most likely also exhibits WZ crystal structure. The NWs suffer from carbon contamination from the initial SEM and CL acquisition, which can be seen in Figure 4.11(a). However, the plasma cleaning step proved to be detrimental to the electron transparent carbon film, despite using a shielded holder and short plasma duration. Because of the small number of available NWs deposited on the carbon film, carbon contamination had to be accepted.

Selected-area growth

The SiO_2 mask is found to be 34 ± 4.6 nm thick, which is not far from the targeted thickness of 35 nm. Most NWs are found to grow separately from their respective holes, however, a large fraction coalesces with neighbouring NWs due to variation in radial growth. This was seen in Figure 4.4(b), where one NW has grown on top of and disrupted the growth of the six surrounding NWs. This results in more grain boundaries and interfaces. The same effect was observed in [93, 94]. Figure 4.5 revealed that in addition to area 100_600, some of area 80_600 was also scraped off during the sample preparation routine. These two areas should exhibit the same hole spacing, but different hole diameter. The spacing of the holes in the mask and the hole diameter was measured to be 594 ± 7 nm and 206 ± 13 nm, respectively. The larger uncertainty in hole diameter compared to hole spacing might be caused by contamination from the 80_600 area during sample preparation. The hole spacing is in accordance with the targeted structure for area 100_600 and the holes are distributed with a close to perfect hexagonal pattern, as seen in Figure 4.4. In [94]

it was observed that for smaller hole diameter in the mask, larger NW aspect ratio could be obtained. If this is the case for the present study, it will have contributed to ideally two different aspect ratio NW types. However, only a small fraction of the 80_600 area was scraped, as seen in Figure 4.5(a), and the effect is therefore not likely to be detected.

The NW growth seen from the top (see for example Figure 4.4(b)) does not form a well-defined hexagonal pattern, as the NWs are not centred about the holes. This might be due to spatial bias of the seed particles to one side of the hole. The sharpness of the etch of the hole might also affect the rate of radial growth, and hence how centred the resulting NW is about the hole. This is because the mask constitutes resistance towards radial growth initially. The etch was seen for all NWs, except for NW4 and the cluster, in Figure 4.9. If the mask has a sharp etch, it can exert a larger counter force on the growing seed particles. Variation in the sharpness of the etch around a hole might cause more radial growth in a certain direction, making the resulting NW shifted away from the centre of the hole. This is illustrated in Figure 5.3(a).

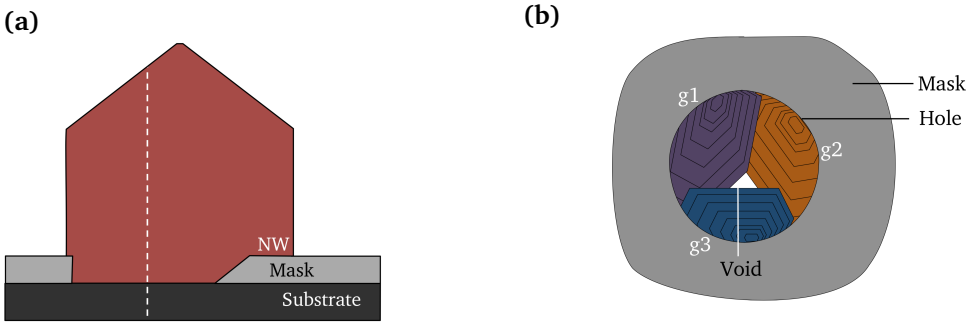

Figure 5.3: Illustration of (a) possible effects of the sharpness of the mask. The centre of the hole in the mask is indicated with a dashed line. In (b) the initial growth site of a NW in the hole of the mask, with three competing seed particles; $g1$, $g2$ and $g3$, is illustrated.

NW defects and irregularities

The orientation of the separate as-grown NWs about the c-axis is random, that is, no preferential orientation is found. Hence, no epitaxial relation to the single layer of graphene is expected [98]. Stacking faults are detected for most of the NWs imaged at zone axis $[11\bar{2}0]$, as seen for NW6 in Figure 4.9. This was also observed for GaN growth on graphene in [91] for lower parts of the NWs. This was explained by the lack of dangling bonds in graphene, leading to significant surface tension and low nucleation densities. Another frequent defect for the studied AlGaN NWs is abrupt changes in facet for the m-planes of the NWs, seen for NW6 in Figure 4.8. In this case, the change of facet is most likely the result of a 30 degree rotation about the c-axis. This could correspond to a change of

facets from $(01\bar{1}0)$ to $(\bar{1}100)$, and should be examined in cross section to figure out if it is related to lattice defects. One possible explanation is that the change of facet stems from two different seed particles with relative rotation to each other. Voids are observed at the initial growth site in Figure 4.2(b). The cause of this feature might be several seed particle competing inside the hole of the mask, as illustrated in Figure 5.3(b). Competing seed particles induce strain in the NWs, due to lattice mismatch between different seed particles. Fractures are detected along some NWs, for example in Figure 4.12. These are possibly the result of initial void defects propagating throughout the entire NW. The uneven contrast seen for the bottom part of the NWs in HAADF STEM is most likely caused by several overlapping grains with lattice mismatch caused by various orientations of the different grains. These effects most likely originate from the initial seed particles and cause additional strain and grain boundaries in the bottom region of the NWs.

Limitations imposed by the sample structure and preparation routine

Due to the pyramidal shape of the NWs a large variation in thickness is present, from approximately 500 nm at the bottom to 0 nm at the tip. This is illustrated with cross sections from four positions along the c-axis in Figure 5.4. Thickness

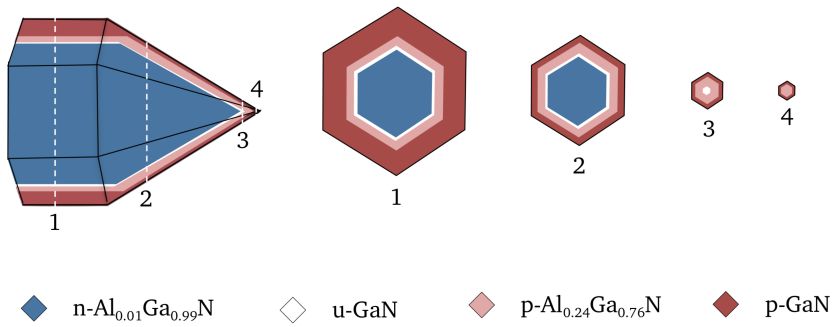

Figure 5.4: Illustration of an AlGaN NW with a radial heterostructure, where the cross section at four different locations along the c-axis has been presented. Depending on where on the c-axis the electron beam is incident on the NW, the thickness and the ratio of the thickness of the different layers varies.

variations affect the spatial signal yield for all applied techniques. HRTEM is, for example, only achieved at the thinner top region of the NWs. EDS yield is seen to increase with thickness and absorption of low energy X-rays deteriorates the signal, especially for thicker parts of the NWs. This makes elemental composition based on quantification of different signals hard, as it is ambiguous whether or not an alteration is a result of a change in the thickness or an actual change in the signal. The Cliff-Lorimer method is found to produce imprecise atomic percentages for the AlGaN NWs. Another problem is that one might not be able to detect a certain signal at all due to the small size of the feature, especially for low S/N. This might be the case for the u-GaN layer in the present study, which is only detected for one

of the NWs by HAADF STEM. Because the detected layer is only about ~ 5 nm thick, the resulting signal most likely disappears in the noise level.

As opposed to high aspect ratio NWs, who most often deposit with $[01\bar{1}0]$ perpendicular to the grid, the NWs in this study deposit onto the TEM grids with random orientation. This is partly because the attached mask material makes it energetically favourable for the NWs to deposit in a random fashion, depending on the geometry of the attachment. The shape of the NWs, their low aspect ratio and interaction with other NWs also affect the orientation after deposition. This is illustrated schematically in Figure 5.5 and makes the reorientation of the separate NWs onto specific zones in TEM more time-consuming. The NWs are inspected in

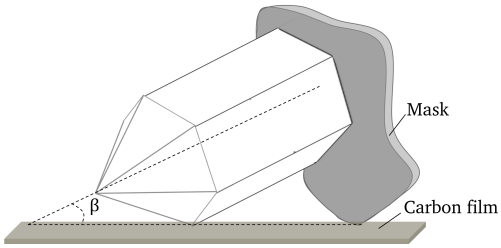

Figure 5.5: Illustration of a NW deposited onto grid with angle β to the carbon film, due to the geometry of the mask attachment.

SEM and CL with their original orientation after deposition onto the grid, that is, the NWs are not reoriented onto a specific zone during SEM and CL inspection. This is due to the limited space between the sample and the CL detection mirror inside the SEM chamber. The angle β in Figure 5.5 therefore affects the interaction volume of the electron beam in SEM and CL. For larger NW clusters it is more likely that deposition occurs with the c-axis perpendicular to the grid as seen in Figure 4.2, that is, $\beta = \pm 90$ degrees.

The sample preparation routine described in section 3.2 might induce alterations in the NWs, or it could be selective to certain sizes or shapes. In case of the latter, the results from the present study would not be representative for the NW growth on the substrate. However, by comparing the NW geometry from the correlated study with the results from the initial inspection of the as-grown sample, no such effect is confirmed.

5.2 Compositional characterisation

The known constituents of different composition in the studied NW structure are $Al_xGa_{1-x}N$ of varying x, SiO_2 from the mask, graphene from the contact layer and sapphire (Al_2O_3) from the substrate. The two latter components were identified in Figure 4.6, but are not detected after preparation of NWs onto grids. From CL, the x variable in $Al_xGa_{1-x}N$ is found to vary from 0 to approximately 40%. The experimental setup limits the CL detection system to a maximum energy of 4.781 eV, which corresponds to approximately 50% Al.

Variation in the thickness of the p-GaN layer

The variation in SE yield was seen both for as-grown NWs in Figure 4.1 and for NWs deposited on grids in Figure 4.3. For the latter, this feature is detected for NWs with various orientations. Hence, it is not simply an effect of the spatial bias from the detector. The variation in SE yield seen in SEM in Figure 4.1 and Figure 4.3 is a result of different elements having different work functions. Because Ga has a higher atomic number than Al, the latter is expected to exhibit lower SE yield. From HAADF STEM and EDS this trend is confirmed, as the p-GaN layer on the m-planes is found to be significantly thicker than the same layer on the r-planes. This is illustrated with interaction volumes in Figure 5.6. The interaction volume of a 5 kV electron beam has been simulated for an electron beam incident perpendicular to the surface and with an incident angle of 28 degrees in Appendix C. These two conditions are equivalent to an electron beam incident on the m-plane and on the r-plane of a NW on zone axis $[11\bar{2}0]$, respectively. The interaction depth is found to be approximately 200 nm for both cases. For the 28 degree tilt, however, the entire interaction volume is slightly tilted. Because the interaction volume created where the electron beam hits the m-plane includes a large fraction of the p-GaN layer, compared to the interaction volume created where the beam hits the r-plane, the r-planes appear darker. In conclusion, SE contrast in SEM is a function of many variables and should be interpreted with care.

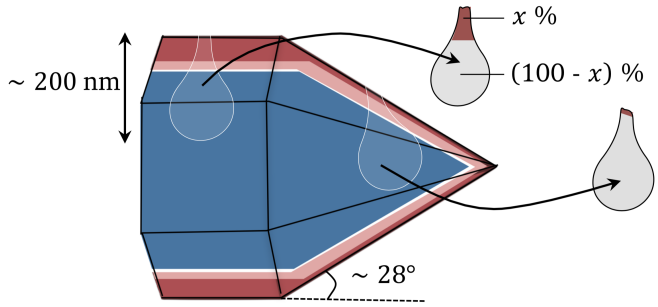

Figure 5.6: Illustration showing the variation in composition within the interaction volume for an electron beam incident on the m- and the r-plane. The percentage of p-GaN is denoted x and the difference in the incident angle of the electron beam for the two planes is ~ 28 degrees.

Quantitative and qualitative findings regarding the radial heterostructure

For $Al_xGa_{1-x}N$ the lattice constants change with x, however, only slightly as seen in Figure 2.3. Hence, it is hard to differentiate the crystal structure of different Al percentages with diffraction patterns and conventional TEM. Al and Ga do, however, have a significant difference in atomic number, and it is therefore possible to distinguish between $Al_xGa_{1-x}N$ with different x values using Z-contrast in HAADF STEM [62]. The dark shell layer in Figure 4.9 is a result of this Z-contrast, as it has higher Al percentage relative to the surrounding layers. This

is confirmed for NW5 by EDS in Figure 4.14. A low intensity peak from CL centred about 307 nm indicates an Al percentage of approximately 23% for this dark shell layer. From Figure 4.15 it can be seen that where the Al percentage increases, there is a corresponding decrease in Ga. This is in accordance with the formula for $Al_xGa_{1-x}N$. The EDS yield for the different NWs is found to vary across the acquired scans in a random manner. This can be explained by undesirable absorption inside the sample and the detector, which depends on the geometry and composition of the sample and the spatial bias from the detector. From Equation 2.51 it can be seen that the longer the distance the X-ray has to travel to the detector, the lower the resulting intensity. EDS yield also varies significantly among the different elements. Ga has the highest yield in all cases followed by Al, and N has the lowest yield. This is expected as elements of lower atomic number are known to exhibit lower fluorescence yield because the lower energy radiation has less penetrating power and is absorbed more easily.

As a first approximation, the composition from EDS is attempted quantified by the Cliff-Lorimer method. By using k-factors from the AZtec software for NW5, the percentage of N was found to be approximately 30. However, we know from the AlGaN formula that there should be 50% III elements and 50% V elements. The thickness of the scanned region is > 100 nm, which is larger than the recommended thickness for the method. From Figure 4.15 and Figure 4.16 it appears as if the thickness effect decays by applying the Cliff-Lorimer method, but the effect from absorption remains. Hence, more robust quantification methods like the Zeta-factor method [99] should be applied. Similar observations were seen and the same conclusion was drawn in [61] for GaN NWs. EDS maps were not able to resolve the u-GaN layer for any of the NWs. The spatial resolution in EDS is the size of the probe (~ 1 nm) plus broadening from the interaction volume, that is a few nm at best [58]. The HAADF intensity profile given in Figure 4.10 shows a local minimum for the p-AlGaN layer and a local maximum for the u-GaN layer at approximately 50 nm. The layer has a thickness of about 5 nm and would result in very low X-ray counts.

Compositional irregularities

The dark spots seen in Figure 4.2(b) are most likely from accumulation of Al adatoms at the NW surface. Al has a higher sticking coefficient compared to Ga, which makes the surface mobility of Al less. One possible explanation for this lies in the bond strength between Al and Ga with N. Due to different work functions for Al and Ga, accumulated AlN appears darker than the surrounding GaN/AlGaN.

In Figure 4.6(a), two different contrasts were detected in the scribed area on the substrate after the sample preparation routine was conducted. In Figure 4.6(b) dark circular features separated by approximately 600 nm in a hexagonal pattern were seen. The dark contrast in both of these cases most likely stems from the absence of graphene on top of the sapphire substrate, illustrated in Figure 5.7. That is, for the lighter area graphene is still covering the surface, making it conducting. Removal of graphene might have happend during the EBL step, that is, if the graphene was accidentally etched through. Or graphene might have had such a

strong bond to the NWs and remained attached during scribing. Graphene can be hard to recognise in TEM and was not detected for any of the NWs. It is possible that any remaining graphene was removed during the plasma cleaning step. For the UV LED device, the graphene layer constitutes an essential part and it is important to confirm if the graphene layer was etched through or if it was attached to the scraped-off NWs.

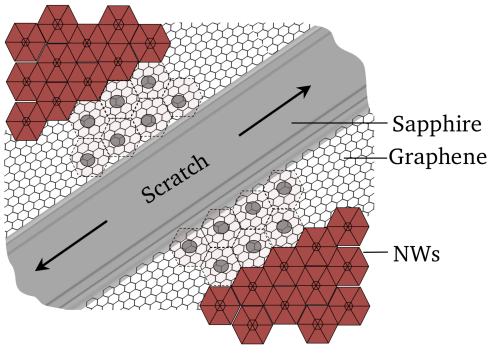

Figure 5.7: Illustration of a scratch on the surface of the as-grown sample after conducting the sample preparation routine. The scratch reveals the sapphire substrate. Some NWs remain attached, while others are scraped off. The circular regions represent areas where NWs have been scraped off and graphene is absent.

In the HAADF STEM intensity profile for NW1 in Figure 4.10(a) the relative variation across the NW is reversed, compared to the rest of the NWs. However, this does not necessarily implicate that the local maxima are caused by a higher average atomic number. In the EDS data from the same NW in Appendix D, an increase in Al and a corresponding decrease in Ga is seen for the lighter shell layer. During acquisition of HAADF STEM from NW1 the microscope settings were at maximum stage height. In order to achieve focus at the $[11\bar{2}0]$ zone a significant defocus was applied and a camera length of 200 mm. For these reasons, diffraction contrast might have dominated over Z-contrast during acquisition, reversing the relative contrast.

5.3 Optical characterisation

Signal delocalisation

The charge carrier diffusion length is an important parameter in CL analysis [77] and should be taken into consideration when evaluating the spatial distribution of luminescence, for example in Figure 4.17. Because of diffusion, the spatial resolution of CL is not only limited by the SEM interaction volume itself, but also by the diffusion of charge carriers before recombination. The detected intensity distribution is affected by this in the sense that emission from certain areas appears less confined than it really is. Diffusion also makes signals from adjacent regions overlap, which makes interpretation more complicated. This can

be seen in Figure 4.22, where the extracted NMF components overlap. Moreover, the diffusion constant varies for different materials and also with temperature. Counter-intuitively the diffusion length increases in regions of higher crystal quality, hence inferior spatial resolution might occur in such regions. Depending on the surrounding energy landscape, electrons excited in one area might also have a preferential flow direction, for example if a built-in electrical field is present. The latter is especially important for nitrides, due to the polarity of the III-V bond causing spontaneous and piezoelectric polarisations.

In addition to signal delocalisation by diffusion, the NWs in this study are not systematically oriented onto a specific zone prior to CL detection. Therefore, the incident angle of the electron beam is more or less random and this affects the volume emitting the optical signal. If the NW c-axis has a significant angle to the carbon film (see β in Figure 5.5), the NW core might be excited to a less extent compared with the exterior shell.

Intensity decrease along the NW c-axis

The most frequent occurring peak with highest intensity is centred about 361 nm, as seen from the histogram in Figure 4.18. This wavelength corresponds to approximately 1.5% Al. The component in the radial heterostructure occupying the largest volume is the n-AlGaN core which, according to nominal values, have about 1% Al. The intensity of all individual NWs in the wavelength range intended for the UV LED is found to decrease along the c-axis, from top to bottom of the NWs. This can be seen in Figure 4.17 and Figure 4.19. The intensity at edges is also low. The bottom part of the NWs is known to exhibit more defects and irregularities, compared to the top. This can be seen from the SEM images in Figure 4.8 and the HAADF STEM images in Figure 4.9. SEM shows changes of facets and other irregularities in the NW morphology. Conventional TEM and HAADF STEM show uneven contrast from grain boundaries and BSFs. This can cause non-radiative defect-related recombination or make recombination occur through other undesirable paths. The reason why the NWs show low intensity at interfaces between facets might be shorter recombination lifetime for non-radiative recombination events, as observed with PL lifetime measurements in [100]. Another factor that might cause an intensity alteration is the variation in length from the NW surface to the active u-GaN layer. This is the distance a charge carrier has to travel in order to recombine in the u-GaN layer, and this distance increases from top to bottom of the NW. In Figure 5.8 the bandgap according to nominal growth is illustrated. Electrons and holes seek smaller bandgap areas through transport mechanisms like diffusion. In the top region of the NWs the diffusion length in to the u-GaN layer is shorter. This explains why recombination in the u-GaN layer is favoured in the top region. Charge carrier occupation is dictated by the Pauli exclusion principle [17] and if the states in the narrow u-GaN layer are all filled up, the charge carriers must find other low bandgap areas to recombine in. The smallest bandgap in the NWs is the gap from p-GaN. Because of the heavy doping in the p-GaN layer, the recombination probability is increased, according to Equation 2.6. Hence, with a higher recombination probability in the

p-GaN layer and a longer diffusion length into the intrinsic layer (and a thicker p-GaN layer to recombine in), charge carriers are more likely to recombine in the p-GaN layer for the bottom part of the NWs. This results in a decrease in intensity at the intended wavelength.

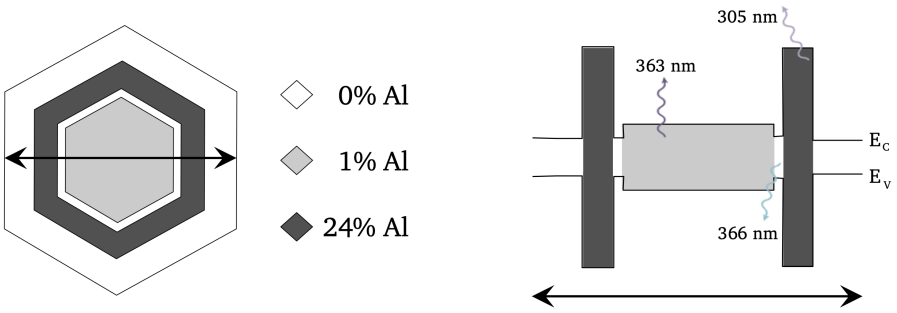

Figure 5.8: Schematic of the bandgap across a radial heterostructured NW. The nominal Al percentage and the expected wavelength, according to Equation 2.3 and Equation 2.9, is given. The final contact layer is heavily p-doped, which effectively reduces the bandgap.

Redshift of main emission band

Another frequent occurring trend for the studied NWs is a shift towards longer wavelengths for the bottom region of the NWs. In order for a redshift to occur in a CL spectrum, a component with a smaller bandgap must be introduced. The components in the NW structure emitting in the relevant wavelength range for the observed shift are:

- n-$Al_{0.01}Ga_{0.99}N$ ($\lambda \sim 363$ nm)
- n-GaN and u-GaN ($\lambda \sim 366$ nm)
- p-GaN/p++-GaN (366 nm$< \lambda < 371$ nm)

Hence, according to nominal growth the CL spectra should contain peaks at three different wavelengths. For the latter component, the wavelength is expected to increase with doping level with a maximum of ~ 5 nm. This is due to Mg-related acceptor levels from p-doping [84]. Because the difference in Al percentage is so small for some components, the peaks overlap (as seen from the NMF decomposition in Figure 4.22). From Figure 5.6 it can be seen that, depending on where along the c-axis the electron beam excites the NW, the number of radial components and the ratio between their volumes differ. Because the exterior p-GaN shell is thicker for the lower m-planes, the optical signal emerging from the NWs is expected to be more and more dominated by the exterior shell towards the bottom. This was illustrated in Figure 5.6, where x is the percentage of p-GaN inside the interaction volume. p-GaN is expected to emit the longest wavelength. Therefore, when the interaction volume is composed of a higher percentage of

p-GaN, the emission peak is expected to shift towards longer wavelength. The principle behind such a shift is illustrated in Figure 5.9. The mean of the sum, that is, the centre of the peak, shifts towards the mean of the component with higher intensity.

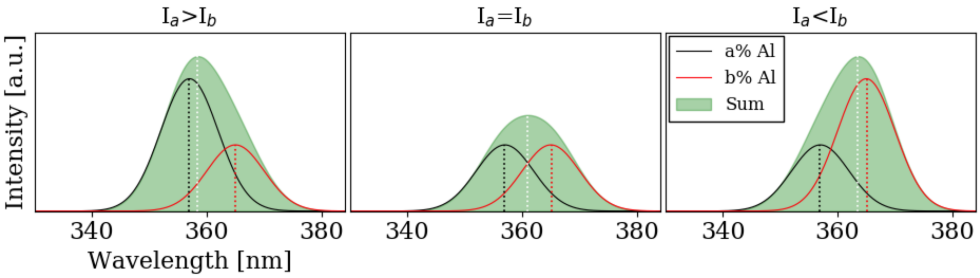

Figure 5.9: Illustration showing how the mean of the sum of two Gaussian peaks (white dashed line) shifts as the intensity ratio between them varies. The standard deviation is set to 5 nm for both peaks with centres 357 nm (a% Al) and 365 nm (b% Al). That is $a > b$.

NMF decomposition and spatial wavelength distribution

From the NMF analysis, three spectral components were found. The average peak positions were observed at 354 nm, 357 nm and 362 nm, with a spread of maximum ± 5 nm for all NWs. These correspond to Al percentages of 4.5%, 3.0% and 1.3%. The component with the shortest wavelength is primarily detected close to the NW tip and the longer wavelength components are less confined and spread towards the bottom of the NW. This is in correspondence with the redshift discussed above. NMF is, however, not designed to decompose the data into Gaussian fits representing certain Al percentages. The NMF analysis applied to the CL data is a sort of black box method, where the only boundary condition set is the number of components the data is divided into. The components are also forced to be non-negative. We know for a fact that the components must be non-negative in order to make physical sense. However, we do not know the dimension of the data. The spectral components generated by the algorithm are therefore not necessarily physical, and only represent patterns that are recognised in the data. Generation of non-physical components can easily occur if one extra component is included. Hence, results extracted from the NMF decomposition method should be interpreted with care.

The wavelength distribution images in Figure 4.21 show where the different wavelengths are detected inside the NWs. The shortest wavelength is for all NWs detected in the upper part, more specifically on the r-planes. The wavelength at edges and towards the bottom of the NWs is found to be longer for all inspected NWs. However, because of charge carrier diffusion, the detection area might not be the same area as where the electron beam excited the electron-hole pair. That is, one such pair could have been generated in the exterior shell layer but later recombined in the core, or the other way around. In literature, various numbers are

reported for the diffusion length in AlGaN, from < 10 nm to > 900 nm [77, 101]. The diffusion length is affected by many factors, for example the size and the crystal quality of the NWs. In general, diffusion lengths increase with crystal quality. It is important to recognise that the NWs are three dimensional in the sense that the shell layer is covering the entire NW, but with different thicknesses for different planes. This makes the examination of radial heterostructures more complicated than axial heterostructures.

Emission in the yellow band

The peak centred around 540 nm stems from YL. Emission in the yellow band is disputed, but a common belief seems to be that it is a result of various defects in the crystal structure of GaN [84]. Relatively high intensity YL is detected near the bottom of the NWs, as seen in Figure 4.20. This part of the NW most likely consists of several seed particles and hence grain boundaries. This was illustrated for competing seed particles in Figure 5.3(a). For all three NWs plotted in Figure 4.24, an increase in intensity within the yellow band is also seen for the tip of the NWs. From Figure 4.17 it can be seen that the targeted wavelength range shows low intensity in the same region. From TEM this region often contains BSFs, which might be responsible for the latter.

Cathodoluminescence versus electroluminescence

The results from the optical characterisation by CL are not expected to perfectly reproduce the characteristics of a working device, excited by EL. The transport of charge carriers, for example, is expected to behave differently. During CL acquisition, charge carriers in the core have to be excited by high-energetic electrons transported from the outside to the core. During EL, on the other hand, majority charge carriers are injected from either side of the junction [42]. Random diffusion is present for both excitation methods but during EL a directional electrical field dominates the transport mechanism. It is also unknown whether or not some of the defect-related luminescence detected in the NWs resulted from sample preparation or was specific to the CL detection setup.

5.4 Correlated findings

The order of inspection for the five different characterisation techniques was found to matter, as the 200 kV electron beam in TEM degrades the CL signal. This was also observed in [12, 59]. The impact of this on the current study is that CL acquisition had to be conducted blindly, as the radial heterostructure is not visible in SEM.

The decrease in intensity from top to bottom of the NWs detected by CL is found to origin from various defects and irregularities in the bottom of the NWs. The latter is detected by TEM, HAADF STEM and SEM and causes non-radiative recombinations, which make the NWs less effective. The defects found include BSFs, facet changes, grain boundaries, voids and fractures.

The redshift, detected by CL for the main emission peak centred about 361 nm, is caused by variations in the thickness of the exterior p-GaN layer along the c-axis of the NWs. The variation in thickness is detected by HAADF STEM, EDS and also SE contrast from SEM. The heavily p-doped GaN layer exhibits certain acceptor levels from impurity Mg atoms substituting Ga sites. These levels make the bandgap effectively smaller, hence, a redshift occurs when the intensity of this signal increases.

From the bottom of the cluster, a peak centred about 274 nm is detected by CL. From HAADF STEM this is suspected to origin from high Al percentage ($\sim 40\%$) seed particles. The bottom of the NWs also exhibits high intensity YL, which is possibly caused by competing seed particles, resulting in a high density of strain-related defects and grain boundaries.

Parasitic growth on top of the SiO_2 mask is found from SEM inspection. From the SAED pattern in Figure 4.7(b) this growth is found to have WZ crystal structure with various crystallographic orientations. The parasitic crystallites are, from HAADF STEM and EDS maps in Figure 4.7(a) and (d), found to exhibit a radial heterostructure with a shell layer of higher Al and lower Ga percentage, compared to the surrounding layers. The thickness of the radial heterostructure of this growth deviates from the intentionally grown heterostructure in the NWs.

6 Conclusion

In this work a correlated study comprised of SEM, HAADF STEM, TEM, EDS and CL was applied to individual position-controlled AlGaN NWs grown on graphene by MOCVD. The aim of this work was to relate structural and compositional features to optical characteristics, in order to identify the attributes responsible for the efficiency droop in III-nitride NWs. Six individual NWs and one cluster were included in this correlated study.

The targeted properties from position-controlled NW growth include separate and uniform NWs with high crystal quality. The selected-area growth was found to produce many separated NWs, but varying degree of radial growth also caused coalescence. The latter provides additional grain boundaries and interfaces, where charge carriers can recombine either non-radiatively or through other undesirable paths. The same effect was observed in the bottom part of the NWs, where competing seed particles induce grain boundaries and strain-related defects. In general, this contributes to the deterioration of the targeted defect-free standard of NWs. The NWs were found to have a diameter and length of 499 ± 113 nm and 574 ± 115 nm, respectively. The different layers of the heterostructure, however, exhibited far less uniform dimensions due to variation in growth rate for different planes. The thick p-GaN layer covering the m-planes of the NWs is anticipated to cause the redshift of the main emission peak, due to the induced acceptor levels from Mg doping. The thickness of the p-GaN layer also makes the diffusion path for charge carriers in to the intrinsic GaN layer longer. By applying NWs instead of planar AlGaN structures the goal is to increase the crystal quality. Threading dislocations were not observed, however, BSFs, abrupt changes of facets, fractures, voids and multiple grain boundaries were detected for the examined NWs. These defects are predominantly found at the bottom of the NWs and reduce emission efficiency in this area.

For the optical data, novel processing techniques based on unsupervised machine learning algorithms, to be more specific factorisation algorithms such as PCA and NMF, were applied. The purpose of this was to remove redundant data and to recognise repeating patterns. Diffusion is, however, found to smear out the spatial distribution of the luminescence, complicating the extraction of patterns from the data. Compositional data from EDS is quantified with the Cliff-Lorimer method. However, the estimated composition is believed to be imprecise due to absorption effects.

Before any conclusions are drawn from this study regarding the efficiency of the

NWs, it is important to consider the difference between characteristics extracted from CL and from EL. Some of the effects discussed above might be specific to CL or to the sample preparation method, and will therefore not impose a lowered efficiency on a working device. The different factors assumed responsible for the efficiency droop and the redshift are summarised in Figure 6.1. Because this study examined a limited number of NWs, the results might not be representative for a full device consisting of thousands of NWs.

In conclusion, the correlated study conducted in this work is applicable primarily for mapping of the structural, compositional and optical characteristics of individual NWs for optoelectronic devices. Due to charge carrier diffusion and hidden internal features in the NWs, it is impossible to correlate the structural and compositional properties to the optical ones with a simple SEM-CL setup. By conducting additional inspections with TEM, HAADF STEM and EDS, the optical features observed by CL can be identified.

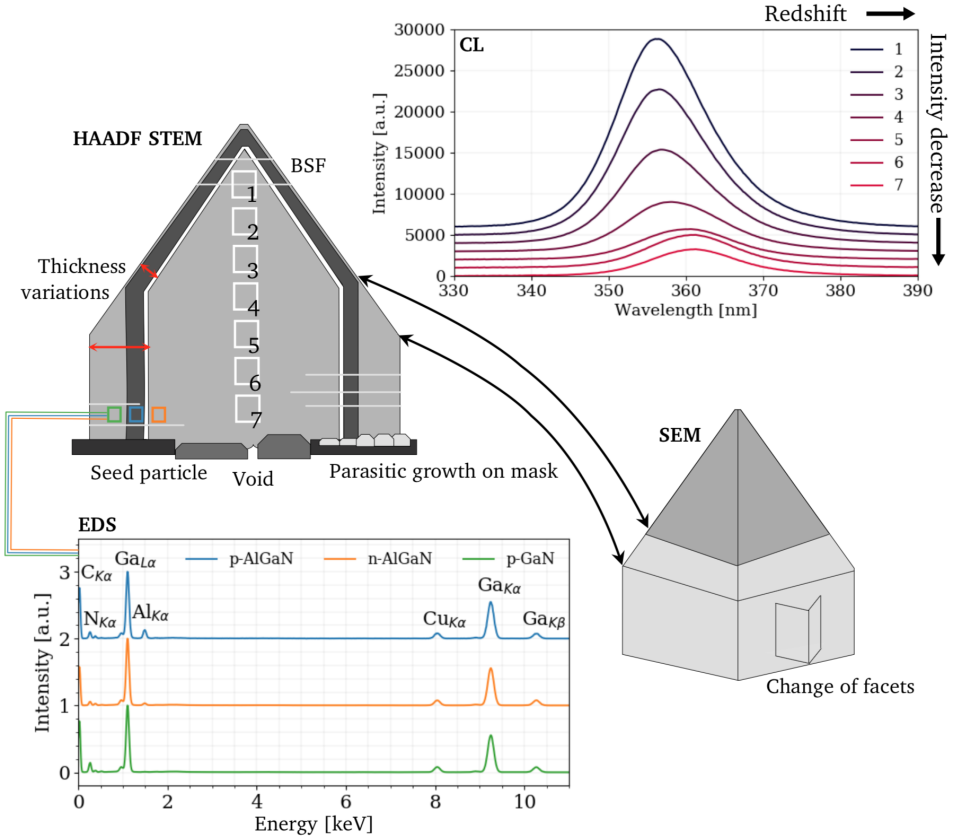

Figure 6.1: Schematic of the different features lowering efficiency and causing a redshift, illustrated with HAADF STEM and SEM contrast, EDS and CL. The features include seed particles, voids, change of facets, BSFs and variation in the thickness of the p-GaN layer. The SE contrast change is also shown. Data from NW5 is used in this illustration.

7 Future work

There are many possible improvements that can be implemented to better correlate the structural, compositional and optical properties of the studies NWs. The presence of intrinsic GaN was, for example, not confirmed by EDS and from HAADF STEM the intrinsic GaN layer was only detected for one NW. Hence, an extended analysis of the NW composition might prove useful. Limitations on the spatial resolution from the SEM-CL setup complicate the localisation of the signal components. In addition, CL is unable to confirm the amount of non-radiative recombination activity. Therefore, alternative optical measurement techniques should be tested and, if possible, incorporated into the correlative approach developed in this work. In what follows, suggestions for future work are presented.

7.1 Extended compositional analysis

Because the intrinsic GaN layer was only observed for one NW with HAADF STEM, an extended study of the NW composition should be applied. The Cliff-Lorimer method (described in section 2.4.4) resulted in imprecise numbers for the atomic percentage of the AlGaN components, possibly due to thickness and absorption effects. The extended study should therefore be independent of sample thickness and absorption. Exactly this can be provided by the Zeta-factor method [58]. In this method, absorption correction for low energy characteristic X-ray lines such as N_K and Al_K is included. The detection of N is especially challenging in the present study. For the Cliff-Lorimer method theoretically computed k-factors or experimentally determined k-factors from standards can be used. In the present study, theoretically computed ones are used, as the experimentally method is time-consuming [99]. For the Zeta-factor method, in-situ measurement of the probe current is required. This is one of the drawbacks with the method. When the specifics of the (S)TEM-EDS setup is determined, suitable standards from pure elements are applied to find the Zeta-factor. Hence, accurate Zeta-factors are more easily obtained and they result in more precise quantification, compared to the Cliff-Lorimer method [102].

As described in section 2.6 and demonstrated in the HAADF intensity profiles in Figure 4.10, composition from HAADF STEM images can be interpreted qualitatively due to Z-contrast. For thin samples (ideally < 50 nm) also quantification from HAADF STEM images is possible. Due to the size of the interaction volume emitting X-rays for EDS analysis, higher spatial resolution can

be achieved by HAADF STEM quantification. HAADF STEM is also very sensitive to Z number, and the acquisition time is low. However, this method requires a high quality specimen and time-consuming sample preparation. In addition, many parameters from the specimen and the instrument must be known, and it is therefore currently not a widely used technique for quantification [62].

7.2 STEM-CL

Similar to how a CL detection system can be integrated in a SEM (see section 2.7.1) the same can be done in a STEM. By taking advantage of the small probe size in the STEM, the spatial resolution of CL can be improved [78]. However, STEM-CL is still limited by charge carrier diffusion, which depends on material properties and operating conditions. Nevertheless, localisation of certain emission peaks might prove easier when a smaller interaction volume is excited. One of the challenges that was encountered in the NMF decomposition analysis was overlapping components, making interpretation ambiguous. By exciting a smaller volume in the NWs, this issue can be reduced, and allocation of specific emission peaks to specific features in the NWs might prove attainable. The spatial resolution can be further enhanced by slicing thin segments from the NWs with a focused ion beam (FIB). From the present and previous studies [12, 59] it is found that the 200 kV electron beam degrades the CL signal. It should therefore be verified whether or not FIB preparation alters the CL spectra. Ultramicrotomy is an alternative to FIB, which can prevent surface damage to the specimen [62], but constitutes a time-consuming preparation technique. Moreover, thinning the structure will reduce the CL signal, which already is a problem for NWs. Therefore, the S/N will be a critical factor and the denoising methods used in the present study for SEM-CL might prove useful. An advantage of STEM-CL is that it can be incorporated into the correlated approach developed in the present work.

7.3 Electron beam-induced current

Electron beam-induced current (EBIC) is a technique that can be applied in SEM or STEM to examine current flow in a device. By inducing a current in a device with an electron beam, electron-hole pairs are generated. If a built-in electrical field is present, for example across a pn-junction, the two carriers separate and current flows. This is detected by applying an external voltage over the device through ohmic contacts. Hence, a high signal is detected for areas where many separations occur, and for recombination centres and defects like BSFs, low to zero signal is detected. EBIC also provides information on the depletion region of a pn-junction and current leakage in a device. In conjunction with CL, charge carrier diffusion lengths should be attempted extracted to approximate the recombination volume and hence the spatial resolution. Similar spectra extracted from CL are generated in EBIC, but the intensity is replaced by current in EBIC [58]. Like CL, this method is limited by the interaction volume of the electron beam, but unlike CL, EBIC can measure non-radiative recombination activity, which will provide complementary information to the structural study presented in this work.

Bibliography

[1] Zissis, G. & Kitsinelis, S. State of art on the science and technology of electrical light sources: From the past to the future. *Journal of Physics D: Applied Physics* **42**, 173001 (2009).

[2] Kneissl, M., Seong, T.-Y., Han, J. & Amano, H. The emergence and prospects of deep-ultraviolet light-emitting diode technologies. *Nature Photonics* **13**, 233–244 (2019).

[3] Nanishi, Y. The birth of the blue LED. *Nature Photonics* **8**, 884–886 (2014).

[4] Kneissl, M., Rass, J., Schade, L. & Schwarz, U. T. *III-Nitride Based Light Emitting Diodes and Applications* (Springer, Cham, 2013).

[5] de la Mata, M., Magén, C., Caroff, P. & Arbiol, J. Atomic Scale Strain Relaxation in Axial Semiconductor III–V Nanowire Heterostructures. *Nano Letters* **14**, 6614–6620 (2014).

[6] The rise and rise of graphene. *Nature Nanotechnology* **5**, 755 (2010).

[7] Saini, A. Europe's Graphene Flagship produces intended results. *MRS Bulletin* **42**, 91–92 (2017).

[8] Zurutuza, A. & Marinelli, C. Challenges and opportunities in graphene commercialization. *Nature Nanotechnology* **9**, 730–734 (2014).

[9] Mazid Munshi, A. & Weman, H. Advances in semiconductor nanowire growth on graphene. *Physica Status Solidi - Rapid Research Letters* **7**, 713–726 (2013).

[10] Bjerknes, C. Teknologiselskap henter 50 millioner og ny ledelse ,. *Dagens næringsliv* Published 14.06.17 [Accessed 04.06.19]. URL `https://www.dn.no/teknologi/ntnu/drager/crayonano/teknologiselskap-henter-50-millioner-og-ny-ledelse/2-1-99417`.

[11] Meland, S. I. Utviklet nanomateriale som kan erstatte kvikksølv. *Gemini* Published 27.05.19 [Accessed 04.06.19]. URL `https://gemini.no/2019/05/utviklet-nanomateriale-som-kan-erstatte-kvikksolv/`.

[12] Hansen, I. Correlated SEM/CL/TEM of MOCVD Grown GaN/AlGaN Nanowires on Graphene (Project work). *Norwegian University of Science and Technology, Department of Physics (TFY4520)* (2018).

[13] Vázquez, M. *Magnetic Nano- and Microwires: Design, Synthesis, Properties and Applications* (Elsevier, 2015).

[14] Yan, R., Gargas, D. & Yang, P. Nanowire photonics. *Nature Photonics* **3**, 569–576 (2009).

[15] Dayeh, S. A., Morral, A. F. I. & Jagadish, C. (eds.) *Semiconductor Nanowires I - Growth and Theory*, vol. 93 (Elsevier, 2015).

[16] Dayeh, S. A., Morral, A. F. I. & Jagadish, C. (eds.) *Semiconductor Nanowires II: Properties and Applications*, vol. 94 (Elsevier, 2016).

[17] Kittel, C. *Introduction to Solid State Physics* (John Wiley & Sons, Inc., 2004).

[18] Colinge, J.-P. & Greer, J. C. *Nanowire Transistors: Physics of Devices and Materials in One Dimension Jean-Pierre Colinge and James C. Greer*, vol. 42 (Cambridge University Press, 2017).

[19] Mohammad, N. S. Understanding quantum confinement in nanowires: Basics, applications and possible laws. *Journal of Physics Condensed Matter* **26**, 423202 (2014).

[20] Quay, R. *Gallium Nitride Electronics* (Springer-Verlag Berlin Heidelberg, 2008).

[21] Kyrtsos, A., Matsubara, M. & Bellotti, E. First-principles study of the impact of the atomic configuration on the electronic properties of AlxGa1-x N alloys. *Physical Review B* **99**, 035201 (2019).

[22] Raza, H. (ed.) *Graphene Nanoelectronics Metrology, Synthesis, Properties and Applications* (Springer, 2012).

[23] Bhattacharya D.K., T. P. *Engineering Physics* (Oxford University Press, 2015).

[24] Kasap, S. & Capper, P. (eds.) *Springer Handbook of Electronic and Photonic Materials* (Springer, Cham, 2017).

[25] Zheng, Q. & Kim, J.-K. *Graphene for Transparent Conductors* (Springer, 2015).

[26] Suk, J. W. *et al.* Transfer of CVD-grown monolayer graphene onto arbitrary substrates. *ACS Nano* **5**, 6916–6924 (2011).

[27] Deng, S. & Berry, V. Wrinkled, rippled and crumpled graphene: An overview of formation mechanism, electronic properties, and applications. *Materials Today* **19**, 197–212 (2016).

[28] Hedberg, J. Graphene-sheet-wavey (2015). URL `http://www.jameshedberg.com/img/samples/graphene-sheet-wavey.jpg`.

[29] Schäpers, T. *Semiconductor Spintronics* (De Gruyter, 2016).

[30] Hannink, R. & Hill, A. *Nanostructure Control of Materials* (Woodhead Publishing, 2006).

[31] Hao, Y., Zhang, J. F. & Zhang, J. C. *Nitride wide bandgap semiconductor material and electronic devices* (Cambridge University Press, 2016).

[32] Campbell, S. A. *Fabrication Engineering at the Micro- and Nanoscale, 3rd Edition* (Oxford University Press, 2008).

[33] Yang, F. H. *Modern metal-organic chemical vapor deposition (MOCVD) reactors and growing nitride-based materials* (Woodhead Publishing, 2013).

[34] Liudi Mulyo, A. *et al.* Vertical GaN nanocolumns grown on graphene intermediated with a thin AlN buffer layer. *Nanotechnology* **30**, 015604 (2019).

[35] Musolino, M. *et al.* Compatibility of the selective area growth of GaN nanowires on AlN-buffered Si substrates with the operation of light emitting diodes. *Nanotechnology* **26**, 085605 (2015).

[36] Carnevale, S. D., Yang, J., Phillips, P. J., Mills, M. J. & Myers, R. C. Three-Dimensional GaN/AlN Nanowire Heterostructures by Separating Nucleation and Growth Processes. *Nano Letters* **11**, 866–871 (2011).

[37] Songmuang, R., Landré, O. & Daudin, B. From nucleation to growth of catalyst-free GaN nanowires on thin AlN buffer layer. *Applied Physics Letters* **91**, 251902 (2007).

[38] Xiao, H. *Introduction to Semiconductor Manufacturing Technology, 2nd Edition* (SPIE, 2013).

[39] Zhao, D. G. *et al.* Effect of Al incorporation on the AlGaN growth by metalorganic chemical vapor deposition. *Applied Surface Science* **253**, 2452–2455 (2006).

[40] Hofmann, P. *Solid state physics - an Introduction* (Wiley-VCH, 2008).

[41] Liu, J.-M. *Photonic Devices* (Cambridge University Press, 2005).

[42] Muller, R. S., Kamins, T. I. & Chan, M. *Device Electronics for Integrated Circuits, 3rd Edition* (Wiley-VCH, 2003).

[43] Singh, J. *Smart electronic materials: Fundamentals and applications* (University Press, Cambridge, 2005).

[44] Smallman, R. E. & Ngan, A. H. W. *Physical Metallurgy and Advanced Materials, 7th Edition* (Elsevier, 2007).

[45] Rabouw, F. T. & de Mello Donega, C. *Excited-State Dynamics in Colloidal Semiconductor Nanocrystals*, vol. 374 (Springer International Publishing, 2016).

[46] Bao, W., Su, Z., Zheng, C., Ning, J. & Xu, S. Carrier localization effects in InGaN/GaN multiple-quantum-wells LED nanowires: Luminescence quantum efficiency improvement and "Negative" thermal activation energy. *Scientific Reportst* **6**, 34545 (2016).

[47] Gaponenko, S. V. *Introduction to Nanophotonics* (Cambridge University Press, 2010).

[48] Huang, Jian-Jang, Kuo, H.-C. & Shen, S.-C. *Nitride Semiconductor Light-Emitting Diodes (LEDs): Materials, Technologies and Applications* (Elsevier, 2014).

[49] Lakhtakia, A. *The handbook of nanotechnology. Nanometer structures: theory, modeling, and simulation*, vol. 7 (SPIE, 2004).

[50] Park, J. H., Kim, D. Y., Schubert, E. F., Cho, J. & Kim, J. K. Fundamental Limitations of Wide-Bandgap Semiconductors for Light-Emitting Diodes. *ACS Energy Letters* **3**, 655–662 (2018).

[51] Avitabile, P. *Modal Testing: A Practitioner's Guide* (John Wiley & Sons, 2017).

[52] Wang, G.-C. & Lu, T. *RHEED Transmission Mode and Pole Figures* (Springer, New York, NY, 2014).

[53] Campbell, F. C. *Elements of Metallurgy and Engineering Alloys* (ASM International, 2008).

[54] Holt, D. B. & Yacobi, B. G. *Extended defects in semiconductors: Electronic properties, device effects and structures*, vol. 9780521819 (Cambridge University Press, 2007).

[55] Li, K. H. *Nanostructuring for Nitride Light-Emitting Diodes and Optical Cavities* (Springer, 2016).

[56] Tizei, L. H. *et al.* A polarity-driven nanometric luminescence asymmetry in AlN/GaN heterostructures. *Applied Physics Letters* **105**, 143106 (2014).

[57] Zuo, J. M. & Spence, J. C. *Advanced transmission electron microscopy: Imaging and diffraction in nanoscience* (Springer New York, 2016).

[58] Williams, D. B. & Carter, C. B. *Transmission electron microscopy: A textbook for materials science* (Springer, Boston, MA, 2009).

[59] Todorovic, J. Correlated transmission electron microscopy and micro-photoluminescence studies of GaAs-based heterostructured semiconductor nanowires (PhD thesis). *Norwegian University of Science and Technologys* 107 (2012).

[60] Broglie, L. d. Waves and Quanta. *Nature* **112**, 540 (1923).

[61] Nylund, I.-E. Electron Microscopy Characterization of III-Nitride Nanowires grown on Graphene (MSc thesis). *Norwegian University of Science and Technology* (2018).

[62] Kauko, H. Quantitative Scanning Transmission Electron Microscopy Studies on heterostructured GaAs nanowires (PhD thesis) (2013).

[63] Egerton, R. F. *Physical principles of electron microscopy: An introduction to TEM, SEM, and AEM, 2nd Edition* (Springer, 2016).

[64] Yurtsever, A. & Zewail, A. H. Kikuchi ultrafast nanodiffraction in four-dimensional electron microscopy. *Proceedings of the National Academy of Sciences* **108**, 3152–3156 (2011).

[65] Goldstein Joseph I. *et al. Scanning Electron Microscopy and X-ray Microanalysis* (Springer, 2003).

[66] Rösch, F. *Nuclear- and Radiochemistry, Volume 1 - Introduction* (De Gruyter, 2014).

[67] Dahman, Y. *Nanotechnology and Functional Materials for Engineers*, vol. 43 (Elsevier, 2018).

[68] Sabbatini, L. *Polymer Surface Characterization* (De Gruyter, 2014).

[69] Pennycook, S. J. & Nellist, P. D. *Scanning Transmission Electron Microscopy: Imaging and Analysis* (Springer Science & Business Media, 2011).

[70] Stroppa, D. G., Zagonel, L. F., Montoro, L. A., Leite, E. R. & Ramirez, A. J. High-resolution scanning transmission electron microscopy (HRSTEM) techniques: High-resolution imaging and spectroscopy side by side. *ChemPhysChem* **13**, 437–443 (2012).

[71] He, D. S., Li, Z. Y. & Yuan, J. Kinematic HAADF-STEM image simulation of small nanoparticles. *Micron* **74**, 47–53 (2015).

[72] Brydson, R. *Aberration-Corrected Analytical Transmission Electron Microscopy* (John Wiley & Sons, Inc, 2011).

[73] Chen, H. L. *et al.* Determination of n-Type Doping Level in Single GaAs Nanowires by Cathodoluminescence. *Nano Letters* **17**, 6667–6675 (2017).

[74] Glatthaar, M. *et al.* Spatially resolved determination of the dark saturation current of silicon solar cells from electroluminescence images. *Journal of Applied Physics* **105**, 113110 (2009).

[75] Delamarre, A., Lombez, L. & Guillemoles, J. F. Characterization of solar cells using electroluminescence and photoluminescence hyperspectral images. In *Physics, Simulation, and Photonic Engineering of Photovoltaic Devices*, vol. 8256, 825614 (2012).

[76] Meuret, S. *et al.* Complementary cathodoluminescence lifetime imaging configurations in a scanning electron microscope. *Ultramicroscopy* **197**, 28–38 (2019).

[77] Gustafsson, A., Bolinsson, J., Sköld, N. & Samuelson, L. Determination of diffusion lengths in nanowires using cathodoluminescence. *Applied Physics Letters* **97**, 072114 (2010).

[78] Kociak, M. & Zagonel, L. Cathodoluminescence in the Scanning Transmission Electron Microscope. *Ultramicroscopy* **176**, 112–131 (2017).

[79] Jimenez, J. & Tomm, J. W. *Spectroscopic Analysis of Optoelectronic Semiconductors*, vol. 202 (Springer, Cham, 2016).

[80] Edwards, P. R. *et al.* High-Resolution Cathodoluminescence Hyperspectral Imaging of Nitride Nanostructures. In *Microscopy and Microanalysis*, vol. 18, 1212–1219 (2012).

[81] MacRae, C. M., Wilson, N. C. & Torpy, A. Hyperspectral cathodoluminescence. *Mineralogy and Petrology* **107**, 429–440 (2013).

[82] El-Saba, M. *Transport of Information-Carriers in Semiconductors and Nanodevices* (IGI Global, 2017).

[83] Gucsik, A. *Cathodoluminescence and its application in the planetary sciences* (Springer, 2009).

[84] Reshchikov, M. A. & Morko, H. Luminescence properties of defects in GaN. *Journal of Applied Physics* **97**, 061301 (2005).

[85] Mooney, J. & Kambhampati, P. Get the basics right: Jacobian conversion of wavelength and energy scales for quantitative analysis of emission spectra. *Journal of Physical Chemistry Letters* **4**, 3316–3318 (2013).

[86] Hayee, F. *et al.* Correlated optical and electron microscopy reveal the role of multiple defect species and local strain on quantum emission. *arXiv: 1901.05952 [cond-mat. mtrl-sci]* (2019).

[87] Spiegelberg, J. Signal Processing Tools for Electron Microscopy (PhD thesis). *Uppsala University, Department of Physics and Astronomy, Materials Theory* 60 (2018).

[88] Schwarzburg, K. *hyperspyCL* (GitHub repository, https://github.com/ks00x/ hyperspyCL, 2018). URL `https://github.com/ks00x/hyperspyCL`.

[89] Hyun, J. K., Zhang, S. & Lauhon, L. J. Nanowire Heterostructures. *Annual reviews* **43**, 451–479 (2013).

[90] Høiaas, I. M. *et al.* GaN/AlGaN Nanocolumn Ultraviolet Light-Emitting Diode Using Double-Layer Graphene as Substrate and Transparent Electrode. *Nano Letters* **19**, 1649–1658 (2019).

[91] Heilmann, M. *et al.* Vertically Oriented Growth of GaN Nanorods on Si Using Graphene as an Atomically Thin Buffer Layer. *Nano Letters* **16**, 3524–3532 (2016).

[92] Kim, D. C., Høiaas, I. M. E., Heimdal, C. P. J., Fimland, B. O. M. & Weman, H. *Nanowires or nanopyramids grown on graphitic substrate* (PCT patent WO2017009395A1, 2016).

[93] Lin, Y. T., Yeh, T. W., Nakajima, Y. & Dapkus, P. D. Catalyst-free GaN nanorods synthesized by selective area growth. *Advanced Functional Materials* **24**, 3162–3171 (2014).

[94] Coulon, P. M. *et al.* Selective area growth of Ga-polar GaN nanowire arrays by continuous-flow MOVPE: A systematic study on the effect of growth conditions on the array properties. *Physica Status Solidi (B) Basic Research* **252**, 1096–1103 (2015).

[95] Hersee, S. D., Sun, X. & Wang, X. The controlled growth of GaN nanowires. *Nano Letters* **6**, 1808–1811 (2006).

[96] Jung, B. O. *et al.* Morphology development of GaN nanowires using a pulsed-mode MOCVD growth technique. *CrystEngComm* **16**, 2273–2282 (2014).

[97] Ra, Y. H., Navamathavan, R., Kang, S. & Lee, C. R. Different characteristics of InGaN/GaN multiple quantum well heterostructures grown on m- and r-planes of a single n-GaN nanowire using metalorganic chemical vapor deposition. *Journal of Materials Chemistry C* **2**, 2692–2701 (2014).

[98] Munshi, A. M. *et al.* Vertically aligned GaAs nanowires on graphite and few-layer graphene: Generic model and epitaxial growth. *Nano Letters* **12**, 4570–4576 (2012).

[99] Watanabe, M. & Williams, D. B. The quantitative analysis of thin specimens: A review of progress from the Cliff-Lorimer to the new ζ-factor methods. *Journal of Microscopy* **221**, 89–109 (2006).

[100] Hwang, S. *et al.* Optical and Facet-Dependent Carrier Recombination Properties of Hendecafacet InGaN/GaN Microsized Light Emitters. *Crystal Growth and Design* **17**, 3649–3655 (2017).

[101] Barjon, J., Brault, J., Daudin, B., Jalabert, D. & Sieber, B. Cathodoluminescence study of carrier diffusion in AlGaN. *Journal of Applied Physics* **94**, 2755–2757 (2003).

[102] Garmannslund, A. Refinement of the ζ-factor Method for Quantitative Energy-Dispersive X-ray Spectroscopy in Scanning Transmission Electron Microscopy (MSc thesis) 103 (2016). URL `https://brage.bibsys.no/xmlui/handle/11250/2402186`.

[103] Aylward, G. & Findlay, T. *SI Chemical Data, 6th Edition* (Wiley-VCH, 2008).

Appendices

A Source code for CL analysis

A.1 Conversion and calibration of CL h5 files

The following code is adapted from [88] and converts files in .h5 format to the signal class in the HyperSpy library in Python. The data is stored in .hdf5 format.

```
get_ipython().run_line_magic('matplotlib', 'tk')
import h5py as h5
import hyperspy.api as hs
import numpy as np
import numpy as np
import matplotlib.pyplot as plt

#Code adapted from https://github.com/ks00x/hyperspyCL
#Functions that convert .h5 file to signal object in the HyperSpy library
def odemis_to_hyperspy(filename, CL_widthx, specbin=1):
    f=h5.File(filename,'r')
    shome = 'Acquisition2//ImageData/'
    x = f[shome + 'Image']
    cdesc =f['Acquisition2/PhysicalData/ChannelDescription'].value[0].
    decode('utf-8')

    # Plot SEM overview of detection area
    image = f['Preview/Image'].value
    import matplotlib.pyplot as plt
    plt.title('SEM overview image')
    plt.imshow(image)

    cltype = None
    if 'Spectrum' in cdesc :
        cltype = 'spectrum'
    elif 'CL intensity' in cdesc:
        cltype = 'panchrom'
    print('<' + filename + '> original shape :' ,x.shape, cltype)

    # strip unused dimensions and transpose/ reverse index order
    if cltype == 'panchrom' :
        xx=x[0,0,0,:,:].transpose((1,0))
    else :
        xx=x[:,0,0,:,:].transpose((2,1,0))

    if cltype == 'spectrum' :
        #interpolate data to linearize the wavelength scale
        w  = f[shome + 'DimensionScaleC'].value *1e9
        wx = np.linspace(w.min(),w.max(),w.size)
        for i in np.arange(xx.shape[0]) :
            for k in np.arange(xx.shape[1]) :
                xx[i,k,:] = np.interp(wx,w,xx[i,k,:])

        wslope = wx[1]-wx[0]
        woffset = wx.min()
        s = hs.signals.Signal1D(xx)

```

```
    elif cltype == 'panchrom' :
        s = hs.signals.Signal2D(xx)
    else :
        print('unknown type')
    print('hyperspy shape :' ,s.data.shape)

    #Spatial calibration
    pixels_x = f['Acquisition1/ImageData/Image'].shape[4]
    s.metadata.General.title = 'Odemis: ' + cdesc
    s.metadata.General.original_filename = filename
    s.metadata.General.notes = cltype
    s.axes_manager[0].name = 'pos x'
    s.axes_manager[0].scale = CL_widthx/pixels_x
    s.axes_manager[0].offset = f[shome + 'XOffset'].value * 1e6
    s.axes_manager[0].units = 'nm'
    s.axes_manager[1].name = 'pos y'
    s.axes_manager[1].scale = CL_widthx/pixels_x
    s.axes_manager[1].offset = f[shome + 'YOffset'].value * 1e6
    s.axes_manager[1].units = 'nm'

    #Spectral calibration
    if cltype == 'spectrum' :
        s.axes_manager[2].name = 'wavelength'
        s.axes_manager[2].units = 'nm'
        s.axes_manager[2].offset = woffset
        s.axes_manager[2].scale = wslope
        s.metadata.signal_type = 'CL'

    f.close()
    if (specbin > 1) and (cltype == 'spectrum'):
        return( s.rebin(scale=[1,1,specbin]) )
    else :
        return( s )

def odemisSEM_to_hyperspy(filename, CL_widthx) :
    f=h5.File(filename,'r')
    shome = 'Acquisition1//ImageData/'
    x = f[shome + 'Image']
    cdesc =f['Acquisition1/PhysicalData/ChannelDescription'].value[0].
    decode('utf-8')

    print('<' + filename + '> original shape :' ,x.shape)
    # strip unused dimensions and transpose/ reverse index order
    xx=x[0,0,0,:,:].transpose((1,0))
    s = hs.signals.Signal2D(xx)
    print('hyperspy shape :' ,s.data.shape)

    #Spatial calibration
    pixels_x = f['Acquisition1/ImageData/Image'].shape[4]
    s.metadata.General.title = 'Odemis: ' + cdesc
    s.metadata.General.original_filename = filename
    s.axes_manager[0].name = 'pos x'
    s.axes_manager[0].scale = CL_widthx/pixels_x
    s.axes_manager[0].offset = f[shome + 'XOffset'].value * 1e6
    s.axes_manager[0].units = 'nm'
    s.axes_manager[1].name = 'pos y'
    s.axes_manager[1].scale = CL_widthx/pixels_x
```

```
    s.axes_manager[1].offset = f[shome + 'YOffset'].value * 1e6
    s.axes_manager[1].units = 'nm'

    f.close()
    return( s )

#Function that saves .h5 file as .hdf5 file and displays data. The signal in .hdf5 format is returned.
#CL_widthx is the x-width of the detection area for spatial calibration.
def get_signal(h5file,title, CL_widthx, specbin=1):
    s = odemis_to_hyperspy(h5file, CL_widthx, specbin=1)
    s_SEM=odemisSEM_to_hyperspy(h5file, CL_widthx)
    s.save(title, extension='hdf5')
    s = hs.load(title+'.hdf5')
    s.plot()
    s_SEM.plot()
    return s
```

A.2 PCA denoising and NMF decomposition

The following code performs PCA denoising on CL data, followed by NMF decomposition. The PCA denoising step is conducted in a similar manner for EDS data.

```
get_ipython().run_line_magic('matplotlib', 'tk')
import hyperspy.api as hs
import numpy as np
import matplotlib.pyplot as plt

s = hs.load('cluster_A_2.hdf5')    #load and crop data as desired
ll,ul = 260., 600.
s.crop_signal1D(ll,ul)
s.change_dtype('float64')
s.decomposition(normalize_poissonian_noise=True)   # PCA denoising step
s.plot_explained_variance_ratio()
num_components = 5                # Determine number of components from SVD scree plot
s = s.get_decomposition_model(num_components)

s.decomposition(normalize_poissonian_noise=True,algorithm='nmf',  # NMF decomposition
                output_dimension=num_components)

s.plot_decomposition_results()    # plots components and corresponding loadings
a = s.get_decomposition_factors()
wl = np.linspace(ll,ul,len(a.data[0]))

fig,ax=plt.subplots(figsize=(5,4))          # Plot all NMF components
plt.fill_between(wl,a.data[0],label=f'1({int(wl[np.argmax(a.data[2])])} nm)',alpha=0.8)
plt.fill_between(wl,a.data[1],label=f'2({int(wl[np.argmax(a.data[1])])} nm)',alpha=0.8)
plt.fill_between(wl,a.data[2],label=f'3({int(wl[np.argmax(a.data[3])])} nm)',alpha=0.8)
```

```
plt.fill_between(wl,a.data[3],label=f'4({int(wl[np.argmax(a.data[4])])} nm)',alpha=0.8)
plt.fill_between(wl,a.data[4],label=f'5({int(wl[np.argmax(a.data[0])])} nm)',alpha=0.8)
plt.legend(fontsize=14,loc='upper center',fancybox=False,framealpha=0.)
plt.xlim(min(wl),max(wl))
plt.ylim(0,a.data.max())
plt.grid(which='both',color='k',linewidth=0.1,alpha=0.8)
plt.xlabel('Wavelength [nm]')
plt.ylabel('Intensity [a.u.]')
```

A.3 Gaussian decomposition

The following code is written by the author and performs Gaussian decomposition with the *scipy.optimize.curve_fit* package in python.

```
get_ipython().run_line_magic('matplotlib', 'tk')
import numpy as np
import matplotlib.pyplot as plt
from scipy.optimize import curve_fit
import hyperspy.api as hs

def gaussian(x, A, mu, sigma):
    return A*np.exp(-(x-mu)**2/(2*sigma**2))


def gaussian2(x, A,  mu, sigma, A2, mu2, sigma2):
    return gaussian(x, A, mu, sigma) + gaussian(x, A2, mu2, sigma2)


def gaussian3(x, A, mu, sigma, A2, mu2, sigma2, A3, mu3, sigma3):
    return gaussian(x, A, mu, sigma) + gaussian2(x, A2, mu2, sigma2, A3, mu3, sigma3)


ll = 260.       # set wavelength range
ul = 670.

s = hs.load("NW0_A_2.hdf5") # loading, cropping and denoising of data
s.change_dtype('float64')
s.crop_signal1D(ll,ul)
s.decomposition(normalize_poissonian_noise=True)
s = s.get_decomposition_model(3)

I = s.sum().data/s.sum().data.max()    # Normalising and removal of offset
I = I-I.min()

# coefficients for conversion from wavelength (nm) to energy (ev)
hc = (6.63*np.float_power(10,-34)) * (3*np.power(10,8))
ff=(hc/(np.float_power(10,-9)*1.6*np.float_power(10,-19)))

wl = np.linspace(ll,ul,s.axes_manager[2].size)
E = []
for i in range(0,len(wl)):
    E.append(ff/wl[i])
# fitting of amplitude, mean, standard deviation of three gaussians
```

```
popt, pcov = curve_fit(gaussian3, E, I,          # boundary conditions
                       bounds=([0, (1/ul)*ff , 0., 0, (1/ul)*ff, 0.,0.,(1/ul)*ff,0.],
                               [1., (1/ll)*ff, 1, 1., (1/ll)*ff,1 , 1.,(1/ll)*ff, 1]))
#plot original data, gaussian components and sum of fits
fig,ax = plt.subplots()
plt.plot(E,I, label='Data')
plt.fill_between(E, gaussian(E, popt[0], popt[1], popt[2]), alpha=0.6, label = 'Gaussian 1')
plt.fill_between(E, gaussian(E, popt[3], popt[4], popt[5]), alpha=0.6, label = 'Gaussian 2')
plt.fill_between(E, gaussian(E, popt[6], popt[7], popt[8]), alpha=0.6, label = 'Gaussian 3')
plt.plot(E, gaussian3(E, *popt), linewidth=2,linestyle=':', color= 'r', label = 'Sum of fits')
plt.legend()
plt.xlabel('Energy [eV]')
plt.ylabel('Normalised intensity')
```

B Source code for EDS analysis

B.1 Conversion and calibration of EDS raw map data

The following code is adapted from [61] and converts and calibrates raw EDS map data from AZtec. The .OIP format from AZtec is converted into the format .hdf5 and the spatial and spectral calibration files are extracted from map data together with the raw data.

```
import hyperspy.api as hs
import pandas as pd
import re

#Function that imports raw EDS data and calibration files and exports in
#into the signal class in the HyperSpy library as a .hdf5 file.
def imp(rpl, txt, msa, title):
    #Load rpl file, txt file and msa file.
    s = (hs.load(rpl, signal_type="EDS_TEM")).as_signal1D(0)
    spatial_calibration_rawdata = pd.read_csv(txt, sep=' \t', header=None)
    single_spectra = hs.load(msa, signal_type="EDS_TEM")

    #Spectral calibration
    s.get_calibration_from(single_spectra)
    s.axes_manager[2].name='Energy'

    #Spatial calibration
    column = ['2', '3', '4', '5']
    spatial_calibration = []

    for i in column:
        a = [str(s) for s in re.findall(r'\d*[,]?\d?', string=(
     spatial_calibration_rawdata.at[int(i), 0]))]
        z = ''
        for j in range(len(a)):
            z = z + str(a[j])
            z2 = z.replace(',', '.')

        spatial_calibration.append(float(z2))
    names = ['x', 'y']
    units = '$nm$'
    scales = [spatial_calibration[2]/s.axes_manager[0].size,
     spatial_calibration[3]/s.axes_manager[1].size]

    for i in range(2):
        ax = s.axes_manager[i]
        ax.name = names[i]
        ax.units = units
        ax.scale = scales[i]

    #Export as .hdf5 file.
    s.save(title, extension='hdf5')
```

B.2 Cliff-Lorimer method for EDS quantification

The following code is adapted from [61] and quantifies data across a line extracted from a raw EDS map.

```
get_ipython().run_line_magic('matplotlib', 'tk')
import hyperspy.api as hs
import numpy as np
import matplotlib.image as mpimg
import matplotlib.pyplot as plt

def rot(s):                 # function that rotates data cube
        s.data = (np.rot90(s.data))
        temp2 = s.axes_manager[0].size
        s.axes_manager[0].size = s.axes_manager[1].size
        s.axes_manager[1].size = temp2
        return s

hdf5 = 'NW0_A.hdf5'         # load, rotate and rebin data
s = hs.load(hdf5)
s=rot(rot(rot(s)))
s=s.rebin(scale=[4,4,1])

elements = ['Al', 'Ga', 'N']
s.set_elements(elements)
lines = ['Al_Ka', 'Ga_Ka', 'N_Ka']
s.set_lines(lines)
s.add_lines()
k_factors = [1.444, 1.045,3.475] # k-factors for Al, Ga and N from Aztec
    software

AlKa = s.get_lines_intensity()[0]
GaKa = s.get_lines_intensity()[1]
NKa = s.get_lines_intensity()[2]
Intensities = [AlKa, GaKa, NKa]
model_p = s.quantification(Intensities, method='CL',factors=k_factors,
                           composition_units='atomic')

a, b, c = model_p[0].data, model_p[1].data, model_p[2].data #at% for Al,
    Ga and N

# set the desired pixel range for the line
x0, x1 = 1, 196
y0, y1 =42, 65

length_nm=410

al_p,ga_p,n_p = [None]*(x1-x0),[None]*(x1-x0),[None]*(x1-x0)
alpt,gapt,npt = 0 ,0 ,0

for i in range(x0,x1):      # Sum pixels over the thickness of desired
    line
    for j in range(y0,y1):
        alpt= alpt+a[j,i]
        gapt= gapt+b[j,i]
        npt= npt+c[j,i]
    al_p[i-x0]=(alpt)
    ga_p[i-x0]=(gapt)
```

```
    n_p[i-x0]=(npt)
    alpt,gapt,npt = 0,0,0

for i in range(0,x1-x0):       # Normalise based on number of pixels added
    al_p[i]=al_p[i]/(y1-y0)
    ga_p[i]=ga_p[i]/(y1-y0)
    n_p[i]=n_p[i]/(y1-y0)

x=np.linspace(0,length_nm,(x1-x0))
fig,ax=plt.subplots()
plt.plot(x,al_p,label='Al',linewidth=1.1,color='r')
plt.plot(x,ga_p,label='Ga',linewidth=1.1,color='b')
plt.plot(x,n_p,label='N',linewidth=1.1,color='g')
plt.legend(fancybox=False,framealpha=0,ncol=3)
plt.xlabel('x [nm]')
plt.ylabel('Atomic percentage [at.%]')
plt.xlim(0,length_nm)
plt.ylim(0,100.)
plt.grid(which='major')
```

C SEM interaction volume

The penetration depth for an electron beam incident on a sample with atomic number Z can be estimated by the Kanaya-Okayama formula [65]

$$R_{O-K} = 27.6\left(\frac{A}{Z^{0.89}\rho}\right)E_0^{1.67}, \tag{C.1}$$

where A is the atomic weight (g/mol), ρ is the density (g/cm^3) and E_0 is the incident beam energy (keV). The penetration depth for pure GaN and AlN, according to Equation C.1, is estimated to approximately 350 nm and 550 nm, respectively. Here, average values for the III and V component have been used [103].

The interaction volume for a simplified AlGaN heterostructure has been simulated in Figure C.1 with software CASINO 3.3. Two different incident angles for the electron beam are used. The structure consists of a 500 nm thick $Al_{0.01}Ga_{0.99}N$ layer at the bottom followed by a 5 nm thick GaN layer, a 30 nm thick $Al_{0.24}Ga_{0.76}N$ layer and a 20 nm thick GaN layer. Doping was not accounted for in the simulations and average values for the III-V composition are used. The blue trajectories represent the incident beam and BSEs, while green trajectories represent SEs. The depth of the interaction volume is approximately 200 nm for the perpendicular case, and the escape depth for SEs is significantly smaller than for BSEs. For the 28 degree tilt the penetration depth is approximately the same, but the deepest electrons are shifted compared to the surface. This is because the entire interaction volume in Figure C.1(b) is tilted.

The values extracted from Equation C.1 is meant for pure elements and does not account for the layered heterostructure. The simulation, on the other hand, does account for the latter and is based on Monte Carlo experiments. Nevertheless, these numbers are only used as a first approximation to get a rough idea of the extent of the interaction volume.

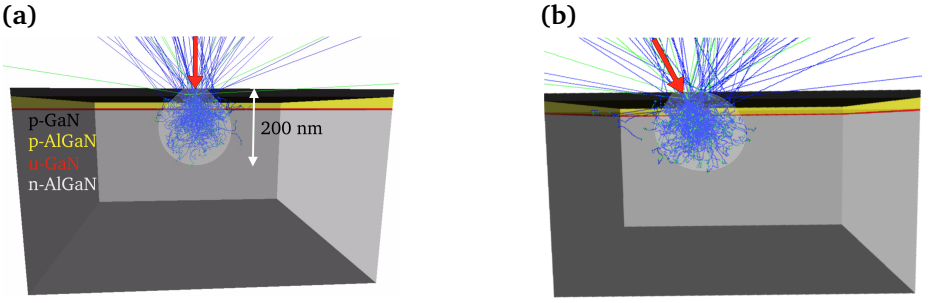

Figure C.1: SEM interaction volume simulated with CASINO v3.3 for an electron beam (a) perpendicular to the surface and (b) tilted 28 degrees. The blue trajectories represent the incident electrons and the backscattered beam, whereas green represent the SEs. The accelerating voltage is 5 kV and the thickness of layers representing n-AlGaN, u-GaN, p-AlGaN and p-GaN is 500 nm, 5 nm, 30 nm and 20 nm, respectively.

D Supplementary EDS data

In this section EDS maps for NW3, NW1, NW4, NW6, NW2 and the cluster is given in Figure D.1, Figure D.2, Figure D.3, Figure D.4 and Figure D.5. The same radial heterostructure is detected for all NWs, except for NW6.

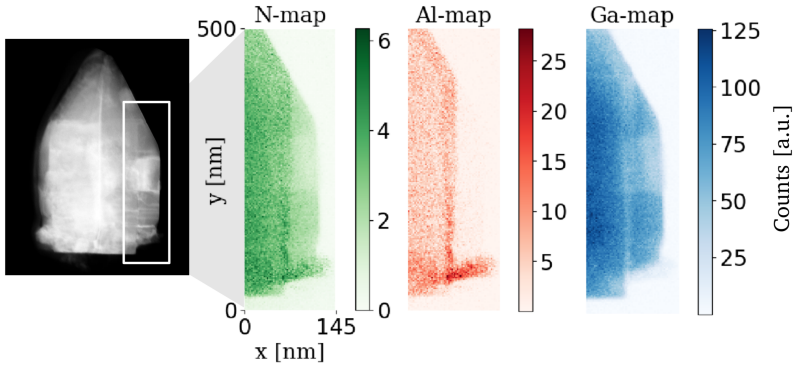

Figure D.1: EDS maps for NW3. The radial heterostructure is barely visible from HAADF STEM, however, with EDS the structure is confirmed.

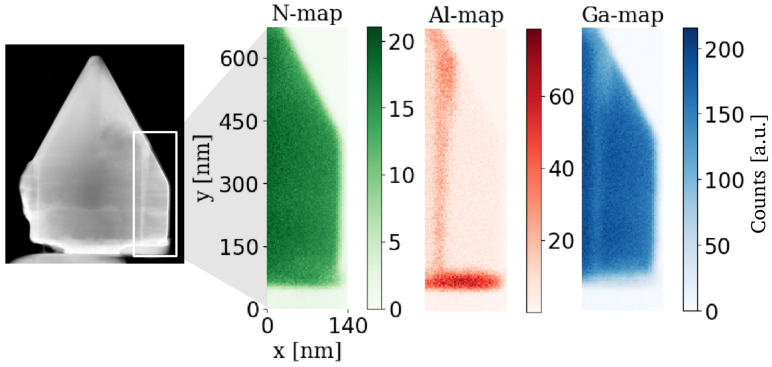

Figure D.2: EDS maps for NW1. The significant difference in the thickness of the p-GaN layer for the m-plane and the semi-polar plane can be seen.

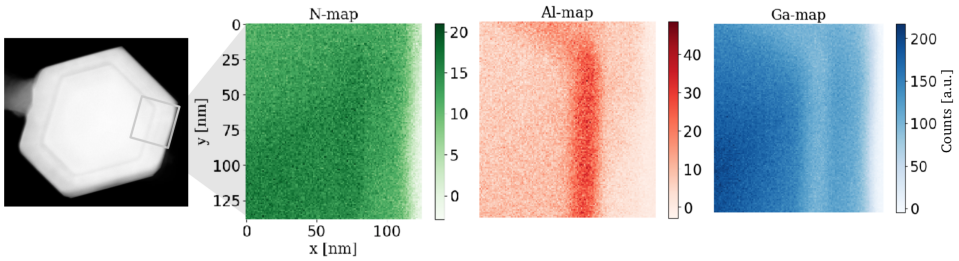

Figure D.3: EDS maps for NW4. The u-GaN layer seen from the HAADF STEM intensity profile in Figure 4.10(b) is not resolved with EDS.

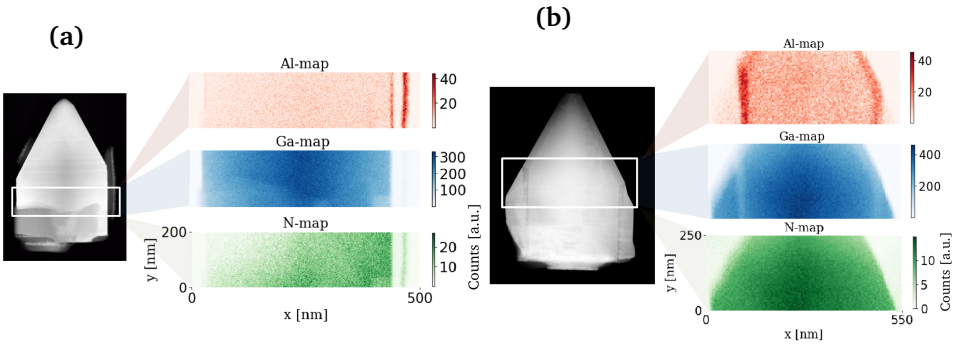

Figure D.4: EDS maps for (a) NW6 and (b) NW2. NW6 does not exhibit the same radial heterostructure as the rest of the NWs. Only a thin layer of higher Al percentage is detected as the exterior shell. The vertical line on the right hand side stems from the growth on top of the mask attached to the m-plane.

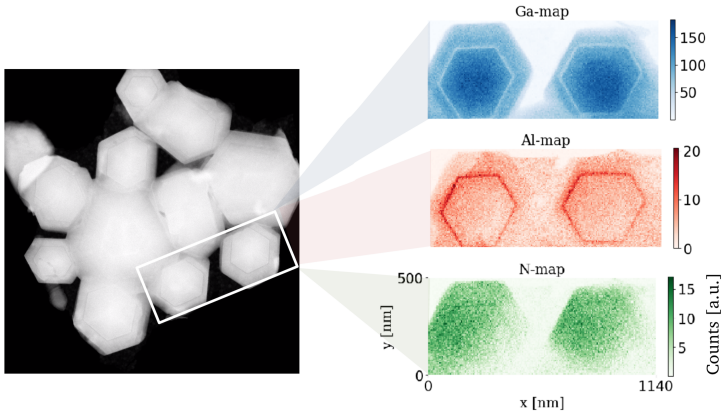

Figure D.5: EDS maps from two NWs in the cluster seen from the bottom through the mask. The high Al percentage layer is visible and an absorption effect can be seen in the lower right corner.

E Supplementary CL data

Intensity decrease and redshift along the NW c-axis
The same trend as seen in Figure 4.19 was detected for the remaining four NWs with the c-axis pointing vertically. Data from the NW1, NW2, NW3 and NW6 is given in Figure E.1, Figure E.2, Figure E.3 and Figure E.4, respectively.

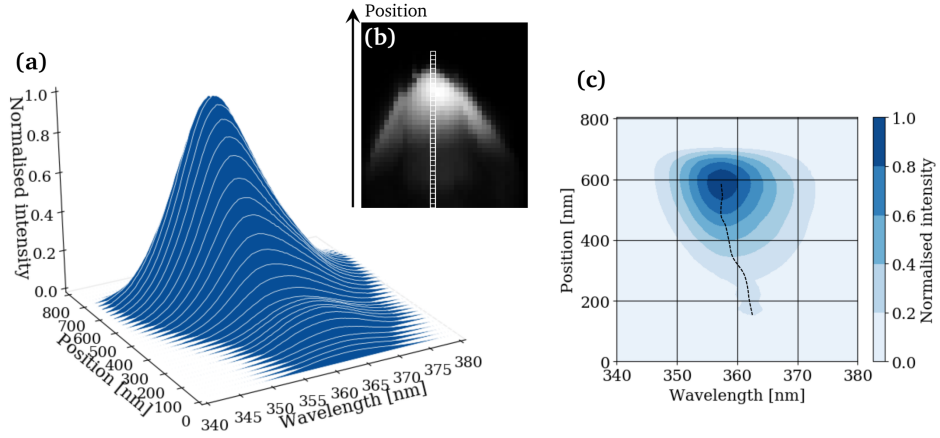

Figure E.1: NW1 exhibits the same trend as seen for NW5 in Figure 4.19. From the top of the NW to the bottom the intensity decreases and the peak shifts towards longer wavelengths.

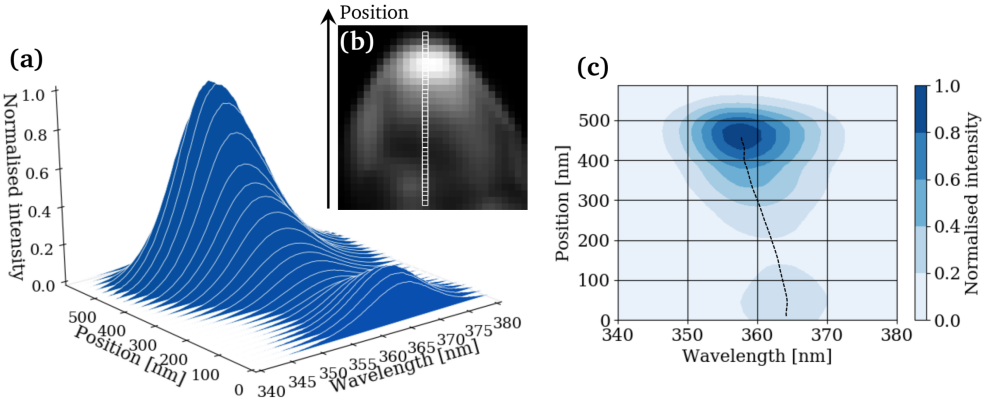

Figure E.2: Intensity and peak position plot for NW2 where an additional small increase is seen at the bottom.

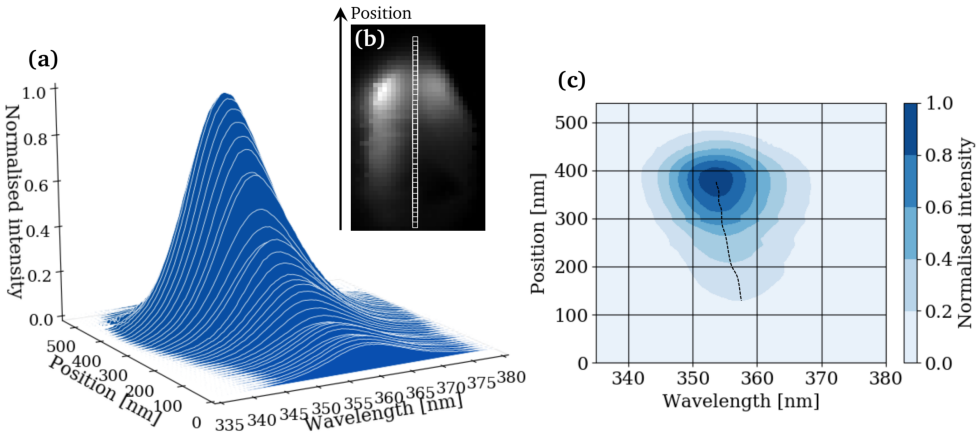

Figure E.3: Intensity and peak position plot for NW3.

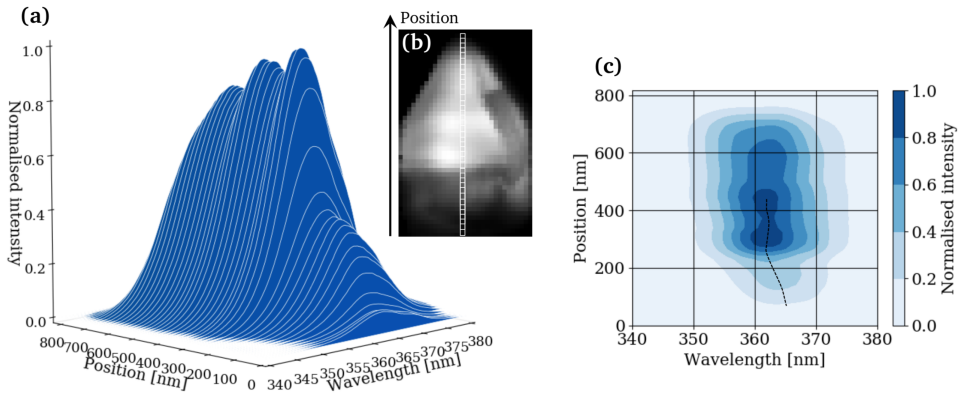

Figure E.4: Intensity and peak position plot for NW6 showing intensity oscillations that deviate from the rest of the NWs. However, a significant decrease in intensity and a redshift is seen at the bottom of the NW.

NMF decomposition method

In this section a worked example of a NMF decomposition is given for NW6. The data is initially denoised with PCA. In Figure E.5(a) the SVD scree plot is given, where the ten first components have been chosen for the denoising step. Extra components are included in the decomposition in order to illustrate weaknesses of the method. For the NMF decomposition, ten components are chosen again and the resulting CL image is given in Figure E.5(b). The wavelength range is 330-420 nm. In Figure E.6 all ten components are plotted together with their respective intensity loadings. Most components represent luminescence from certain regions of the NW (e.g. component 0, 2, 3, etc.), while other components appear as random noise (e.g. 1, 8 and 9). Component number two from the top left corner in Figure E.6 is most likely recognised as the carbon film. In general, it is found that the

dimension of the data for PCA and NMF is the same, and therefore SVD is used also for NMF. The boundary conditions applied are the strictly positive constraint on the components and the number of components. One of the weaknesses of NMF is the latter, as the dimension of the data is unknown, however, NMF decomposition provides a way of efficiently examining large data.

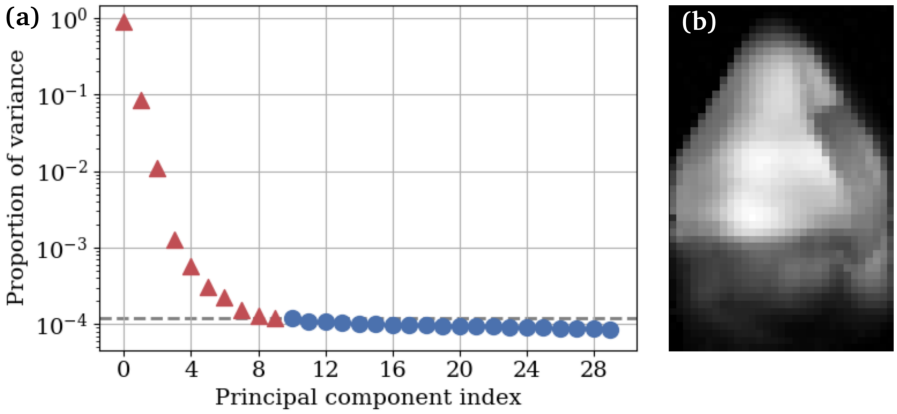

Figure E.5: (a) SVD scree plot of NW6 before PCA denoising. The ten first components are extracted. (b) CL image after PCA and NMF with ten components.

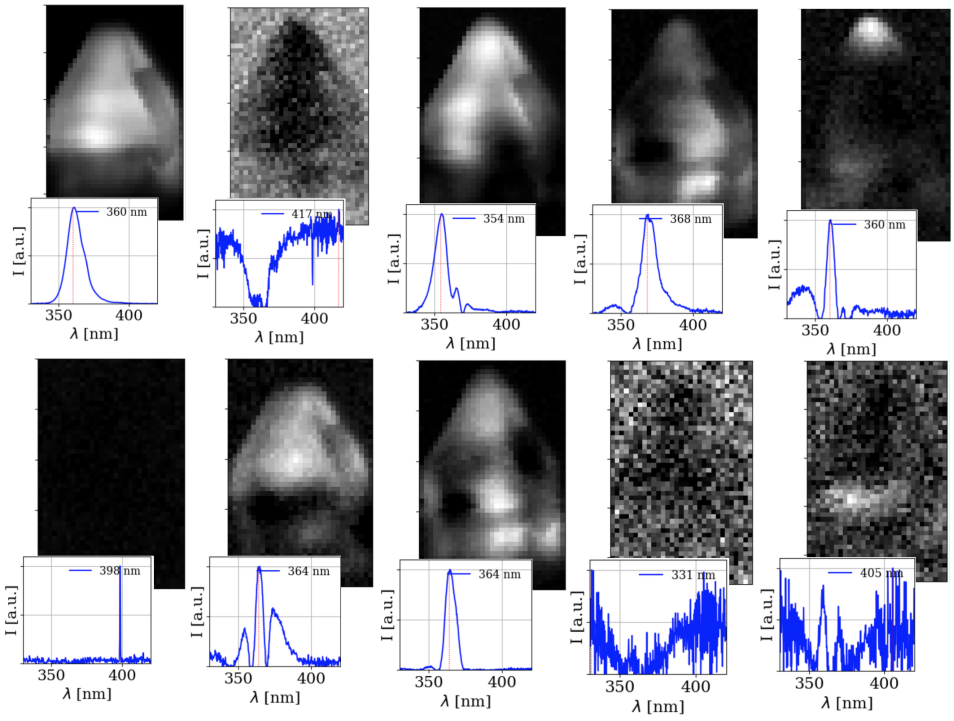

Figure E.6: The ten NMF loadings and corresponding NMF factors for NW6 with index 0, 1, 2 etc. from the top left corner. The peak wavelength for every factor is given.

NMF decomposition analysis
The NMF decomposition for NW3, NW5 and NW6 is given in Figure E.7.

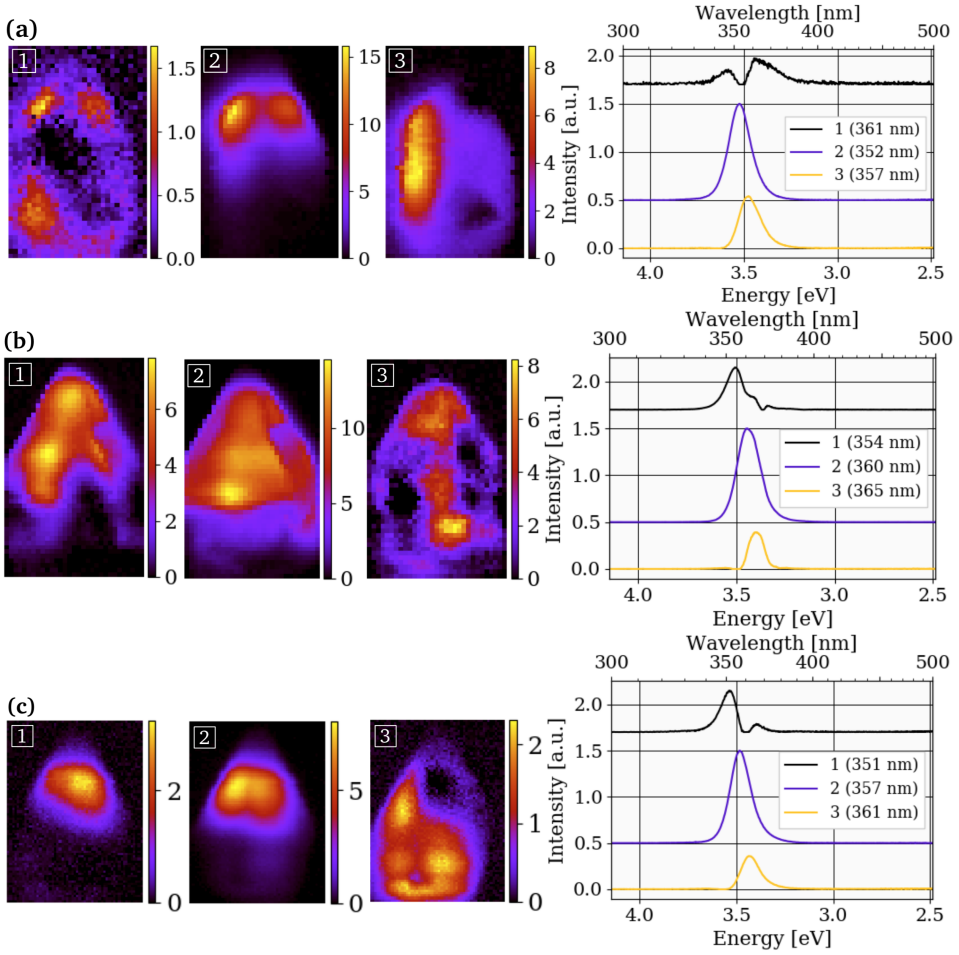

Figure E.7: NMF decomposition of (a) NW3, (b) NW6 and (c) NW5 into three components. The spectral components and their loadings are given. For every component the peak maxima is given.

Wavelength distribution
The distribution of wavelengths in the range 330-380 nm for NW1, NW6, NW2 and NW3 is given in Figure E.8.

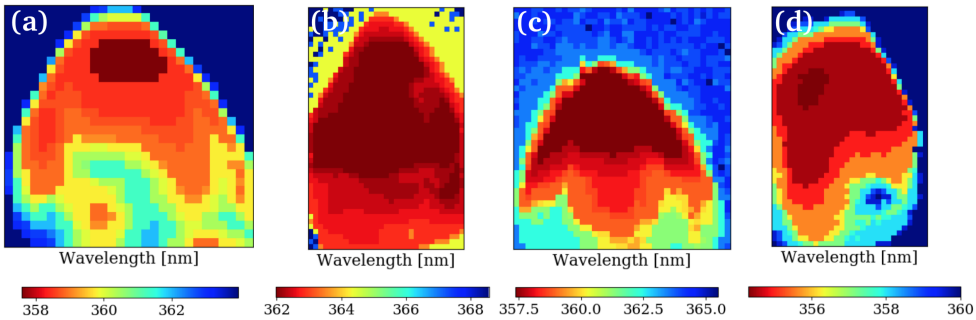

Figure E.8: Wavelength distribution for (a) NW1, (b) NW6, (c) NW2 and (d) NW3. The shortest wavelength is detected at the semi-polar planes for all NWs. Towards the bottom and the edges of the NWs the wavelength increases.

Ingvild Hansen

Correlated Structural and Optical Characterisation of Individual AlGaN Nanowires on Graphene

NTNU
Norwegian University of
Science and Technology

CrayoNano